

AD-A222 049

REPORT DOCUMENTATION PAGE			Form Approved OMB No. 0704-0188
<small>Public reporting burden for this collection of information is estimated to average 1 hour per response, including the time for reviewing instructions, searching existing data sources, gathering and maintaining the data needed, and completing and reviewing the collection of information. Send comments regarding this burden estimate or any other aspect of this collection of information, including suggestions for reducing this burden, to Washington Headquarters Services, Directorate for Information Operations and Reports, 1215 Jefferson Davis Highway, Suite 1204, Arlington, VA 22202-4302, and to the Office of Management and Budget, Paperwork Reduction Project (0704-0188), Washington, DC 20503.</small>			
1. AGENCY USE ONLY (Leave blank)	2. REPORT DATE February 28, 1990	3. REPORT TYPE AND DATES COVERED Final; Jan. 1, 1989-December 31, 1989	
4. TITLE AND SUBTITLE MICROSCOPIC MODELING OF TRIBOLOGICAL PHENOMENA		5. FUNDING NUMBERS 6001E 667716	
AUTHOR(S) Uzi Landman, Regents' Professor (PI) M. W. Ribarsky, Dr. (Co-PI)			
PERFORMING ORGANIZATION NAME(S) AND ADDRESS(ES) Georgia Tech Research Corporation Centennial Research Bldg., Room 24 Atlanta, GA 30332-0420		6. PERFORMING ORGANIZATION REPORT NUMBER AFOSR-TR-90-0578	
SPONSORING/MONITORING AGENCY NAME(S) AND ADDRESS(ES) AFOSR/NC Building 410, Bolling AFB DC 20332-6448		10. SPONSORING/MONITORING AGENCY REPORT NUMBER AFOSR-89-0230	
11. SUPPLEMENTARY NOTES DTIC ELECTE MAY 29 1990 S D & D			
12a. DISTRIBUTION/AVAILABILITY STATEMENT APPROVED FOR PUBLIC RELEASE; DISTRIBUTION IS UNLIMITED.		12b. DISTRIBUTION CODE	
13. ABSTRACT (Maximum 200 words) Computer-based large-scale molecular dynamics simulations are developed, implemented and used to investigate the energetics and dynamical mechanisms in materials under stress and interfacial processes occurring between material tips and substrate surfaces. Studies of the consequences of intermetallic interactions between a nickel tip and a gold surface reveal microscopic information about processes of adhesion, contact formation, nanoindentation, connective neck formation, plastic deformation and fracture. The theoretical predictions correlate well with Atomic-force microscopy experiments. Novel tribological phenomena coupled to enhanced surface superionic conductivity in (CaF_2) are investigated. (calcium fluoride) 56			
14. SUBJECT TERMS Tribological Processes, Nanomechanics, Molecular Dynamics Simulations of Tip-Substrate Interactions, Atomic Force Microscopy, Mechanics, Surface Chemistry, Materials		15. NUMBER OF PAGES	
		16. PRICE CODE	
17. SECURITY CLASSIFICATION OF REPORT UNCLASSIFIED	18. SECURITY CLASSIFICATION OF THIS PAGE UNCLASSIFIED	19. SECURITY CLASSIFICATION OF ABSTRACT UNCLASSIFIED	20. LIMITATION OF ABSTRACT

Microscopic Modeling of Tribological Phenomena

Final Technical Report prepared for the
Air Force Office of Scientific Research

Grant No. AFOSR-89-0230

by

Uzi Landman (PI)
and M. W. Ribarsky (Co-PI)

School of Physics
Georgia Institute of Technology
Atlanta, Georgia 30332

Accession For	
NTIS CRA&I	<input checked="" type="checkbox"/>
DTIC TAB	<input type="checkbox"/>
Unannounced	<input type="checkbox"/>
Justification	
By	
Distribution /	
Availability Codes	
Dist	Avail and/or Special
A-1	



Approved for public release;
distribution unlimited.

CONTENTS

	page
1. Introduction.	1-2
2. Summary of Research Achievements.	3-6
3. Conferences and Symposia Presentation	7
4. Reprints and Preprints.	

1. INTRODUCTION

Understanding the atomistic mechanisms, energetics and dynamics underlying the interactions and physical processes which occur when two materials are brought together (or separated) is fundamentally important to basic and applied problems such as adhesion, contact formation, surface deformations, materials elastic and plastic response characteristics, materials hardness, microindentation, friction, wear and fracture. These considerations have motivated for over a century extensive theoretical and experimental research endeavors of the above phenomena and their technological consequences. Most theoretical approaches to these problems, with a few exceptions, have been anchored in continuum elasticity and contact mechanics. Similarly, until quite recently experimental observations and measurements of surface forces and the consequent materials response to such interactions have been macroscopic in nature.

The recent emergence and proliferation of proximal probes, in particular tip-based microscopies, sensitive to nano- and subnano- meter scale structures provides compelling opportunities for studies of these structures which are key to the science base of many venerable technological problems. In addition these probes, coupled with advances in theoretical understanding of the energetics and interaction mechanisms in materials and the development of computer-based materials modeling and simulation techniques, open new avenues for exploration of new scientific concepts and novel materials properties and processes on the subnanometer scale.

Our research program is aimed at developing the methodology and theoretical models and implementing computational techniques to allow investigations of the aforementioned materials phenomena on the atomistic level. To obtain insights into the energetics and dynamics of such complex systems and phenomena we developed molecular dynamics programs, specifically

designed for studies of the properties of materials under stress and for investigations of the physical consequences of tip-to-substrate interactions.

The work reported herein represents new avenues for studies in the area of nanomechanics and nanodynamics as well as for investigations using the new tip-based spectroscopies. As we describe below (under "Summary of Research Achievements"), in addition to the theoretical studies, we have initiated collaboration with experimental groups and thus have developed a direct confrontation between theory and experiments.

2. SUMMARY OF RESEARCH ACHIEVEMENTS

The research program supported under the above AFOSR grant is a continuation of a research effort which was initially supported by DARPA, in the context of an initiative directed toward investigations of tribological phenomena. Our studies focus on basic understanding on the atomic level of tribological phenomena and of the properties and response of materials under stressed conditions. In order to gain such knowledge, on the microscopic scale, we have developed, implemented and analyzed computer-based large-scale molecular dynamics simulation methods, which allow probing of the aforementioned phenomena with refined spatial and temporal resolution.

In addition to the theoretical studies, we have initiated and formed active collaborations with experimental research groups (in particular at NRL and Hughes) which result in a comprehensive understanding of fundamental processes which are key to further studies and to future technological applications.

The research achievements of our investigations may be summarized as follows:

- (i) Development and implementation of the methodology and numerical simulation techniques for studies of stress, strain and finite deformations in materials. See: M. W. Ribarsky and Uzi Landman, Phys. Rev. B38, 9522 (1988).
- (ii) Development of the methodology and simulation methods for studies of the structural and dynamical consequences of the interaction between material tips and solid surfaces. These studies are of fundamental importance for understanding the atomic-scale mechanisms underlying tribological, adhesion, wear and other interfacial phenomena, as well as for the development, design and interpretation of experiments using the emerging tip-based microscopies (STM, and in particular, Atomic-Force Microscopy (AFM)).

In our initial studies (see Uzi Landman, W. D. Luedtke and M. W.

Ribarsky, J. Vac. Sci. Technol. A7, 2829 (1989); reprint attached) we have investigated tip-substrate interactions for covalently bonded materials (silicon), demonstrating the local nature of the deformation mechanisms, the atomic origins of the stick-slip phenomenon, and the formation of connective necks upon separation of the tip from the substrate. In these studies, simulations of atomically sharp tips, blunted ordered and disordered tips, in both the constant-height and constant-force scanning modes, have been performed.

Our recent studies (see Uzi Landman, W. D. Luedtke, N. A. Burnham and R. J. Colton, Science, April 27 (1990); preprint attached) focus on the atomistic mechanisms and dynamics of adhesion, nanoindentation and fracture in metallic systems. To simulate faithfully the properties and response in metals one must employ interaction potentials which are many-body in nature, including the electronic contribution to the cohesiveness of these materials. In our studies we have used the embedded atom theory (EAM) potentials where the cohesive interactions are represented by embedding functions, supplemented by parametrized pair-interactions which describe intercore repulsion. The particular system which we have investigated is a large nickel tip (Ni, exposing a (001) facet) interacting with a gold (Au (001)) substrate, chosen because of the difference between the elastic and mechanical properties (such as elastic moduli and hardness) of these materials.

In order to avoid finite size effects, we have used in our molecular dynamics studies a very large number of atoms which resulted in one of the most challenging simulations ever performed (see editorial in Science, 27 October (1989), p. 445).

The results of our studies (see full details in the attached Science preprint) reveal the atomistic mechanisms which underly the formation, upon tip-to-substrate approach, of an intermetallic adhesive junction, monolayer

fracture upon tip-to-substrate separation, plastic deformation of the metal surface region upon slight indentation, and the formation and elongation processes of atomically thin connective necks upon separation following contact.

The theoretical predictions from our studies have been verified by atomic-force microscopy experiments where the predicted hysteresis in the force versus tip-to-sample distance relationship was measured. In addition to guiding the interpretation of experimental data the theoretical results provide significant insights into the microscopic processes of deformation, adhesive friction, fracture and wear phenomena, as well as opening new avenues for critical assessment and reformulation of traditional continuum-based theories of materials deformation and response in the elastic, plastic and inelastic regimes.

(iii) Another facet of our research program focuses on the properties of ionic solids under stress and on interfacial phenomena in ionic materials.

In particular, the system which we have investigated is crystalline CaF_2 , which for the bulk material exhibits the onset of superionic conductivity at $\sim 1420\text{K}$ (while the melting point is at $\sim 1700\text{K}$). Due to this property we expect that the mechanical properties of this material will show pronounced variation with temperature (as is indeed observed experimentally). Our simulations of the response of bulk crystalline CaF_2 to applied strain, for a wide range of temperatures, show a strong dependence of the resolved shear yield stress on temperature.

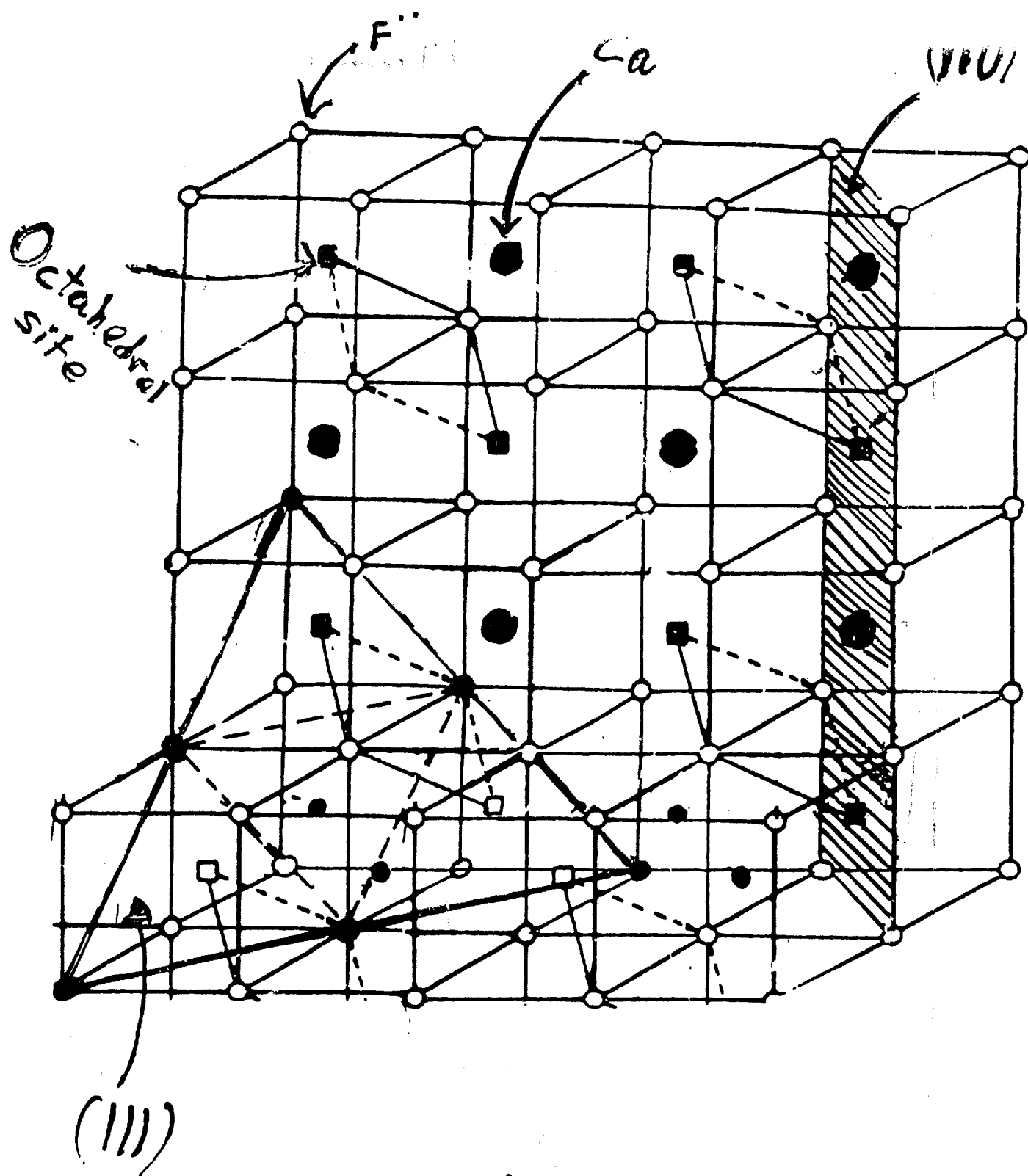
Since our main interest is in interfacial systems we have conducted extensive investigations of the surfaces of this material, exposing the (110) or the (111) crystalline faces. Our investigations show, for the first time, the onset of surface superionic conductivity at temperatures much below that of the bulk. Furthermore, the onset temperature for surface superionic

conductivity ($T_{\text{sic}}^{\text{s}}$) depends strongly on the exposed crystalline face. Thus while for the (111) surface of CaF_2 only a slight enhancement, over bulk values, of mobility of the F^- anions is observed at temperatures below the onset of bulk superionic conductivity ($T_{\text{sic}}^{\text{b}} \sim 1400\text{K}$), the (110) surface becomes a superionic conductor at a temperature as low as 1000K (i.e., 400K below the bulk); see Figure at the end of this section.

In addition to the above findings we observed no premelting of the surfaces ((111) and (110)) at temperatures below the bulk melting temperature. Thus the Ca^{+2} sublattice maintains its crystalline nature up to the melting transition of the crystal.

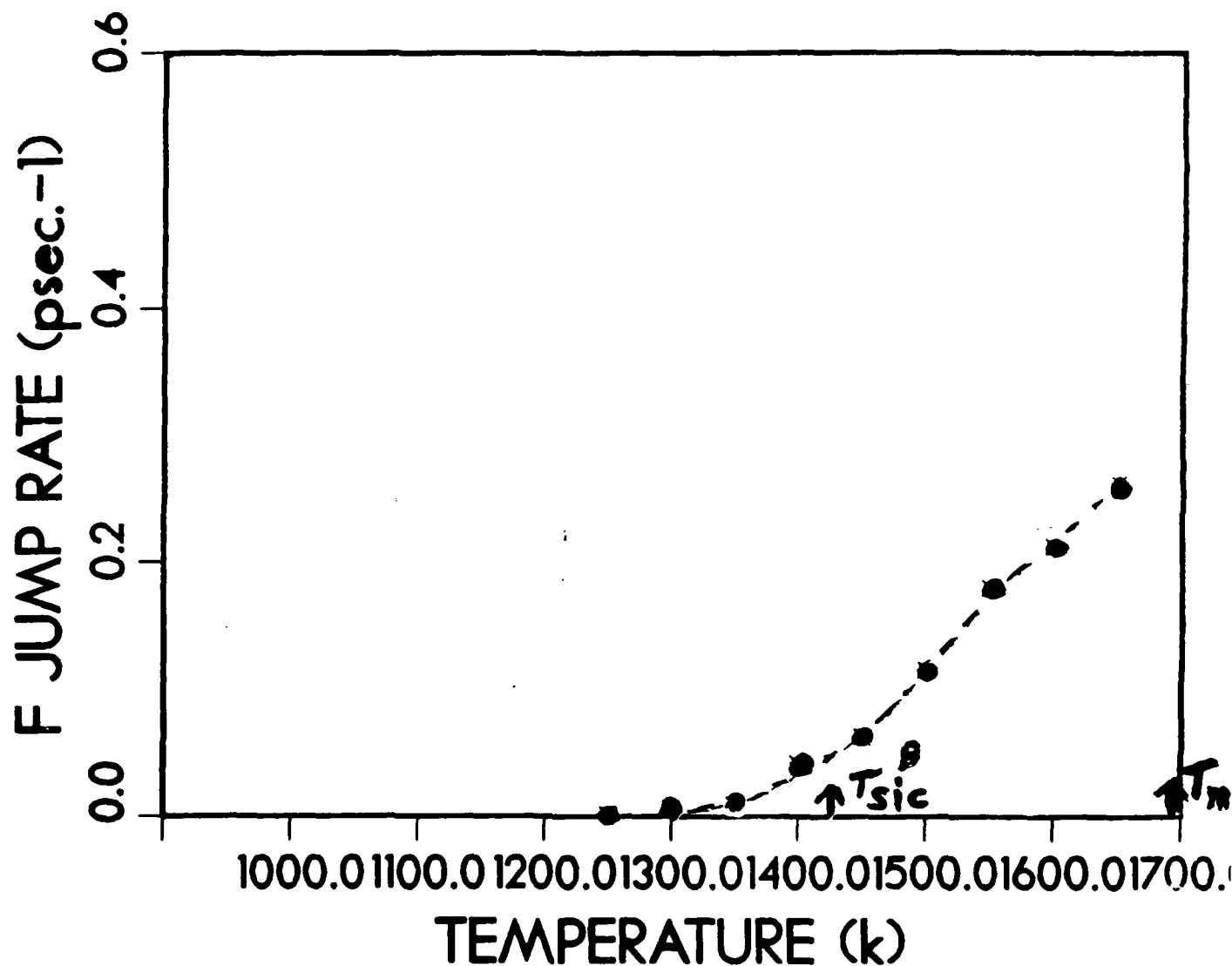
It is of interest to note in this context that the region of space above the topmost layer of the surface does not serve as a diffusion channel. Instead, the presence of the surface serves to lower the activation energy barrier for generation of anion vacancies which in turn promotes jump-diffusion processes in the top layer of the substrate and in deeper layers at higher temperatures. Finally the magnitude of superionic conductivity (as measured for example by the F^- jump rate) at the surface of the material (below and above the bulk onset, $T_{\text{sic}}^{\text{b}} \sim 1400\text{K}$) is noticeably larger than in the bulk.

These results indicate that this system offers a potentially most interesting material, in which tribological characteristics are coupled to a unique physical process (i.e., superionic conductivity). Indeed our current studies of the yielding processes of the material at elevated temperatures, and simulations of calcium difluoride tips interacting and scanning over a CaF_2 crystalline surface show a very pronounced dependence on the substrate temperature as well as on the rate of the scans. In a way one may postulate at this point, that the interface is capable of "self-lubricating" due to the enhanced mobility of F^- at the interface. Further investigations on this system are in progress and will be reported when completed.



CRYSTAL STRUCTURE OF CaF_2
THE (111) and (110) planes ARE INDICATED

BULK CaF₂

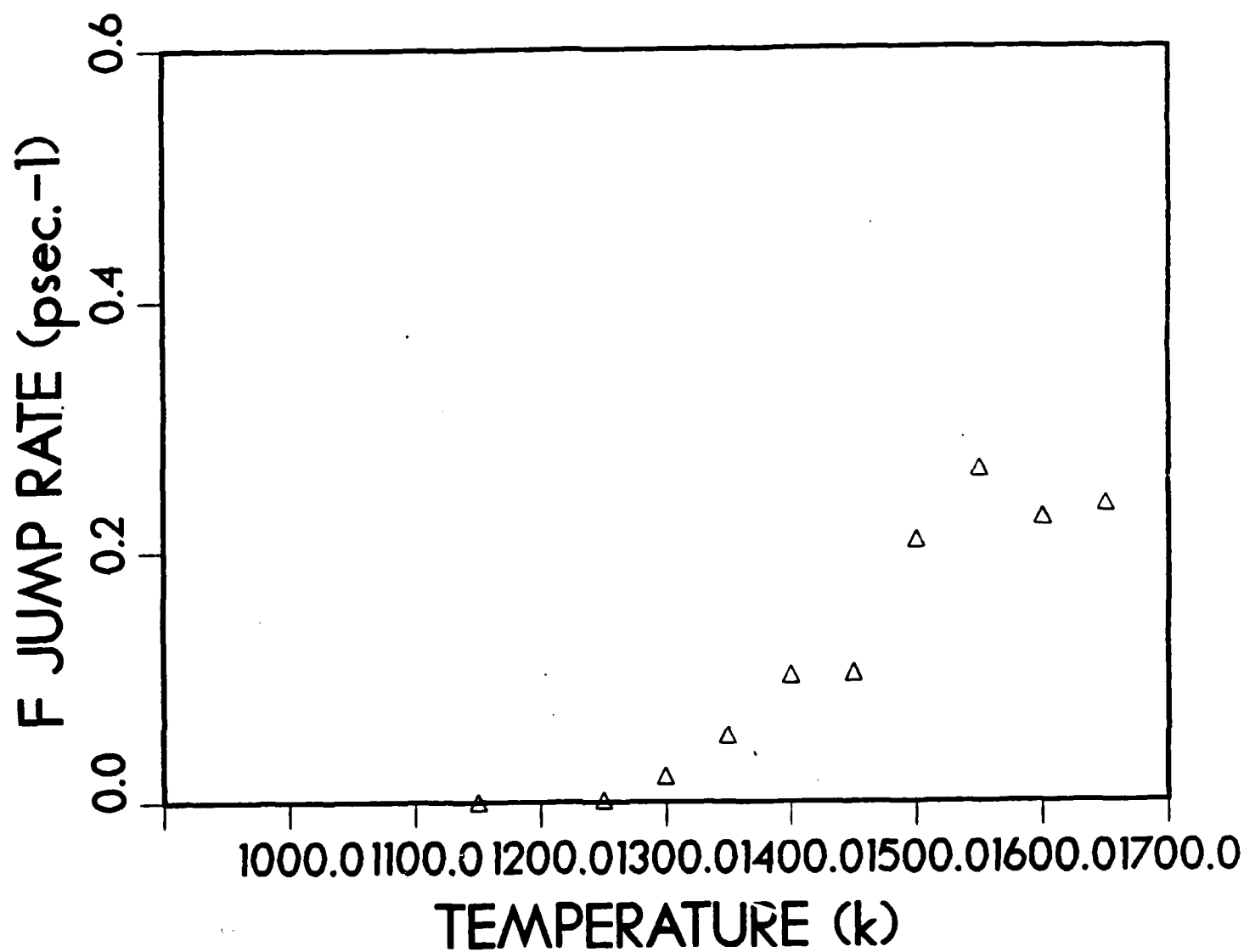


• Molecular dynamics simulation results
 --- experimental data (from conductivity measurements)

T^B_{sic} - denotes the temperature for the onset of bulk superionic conductivity
 T_m - denotes the melting temperature

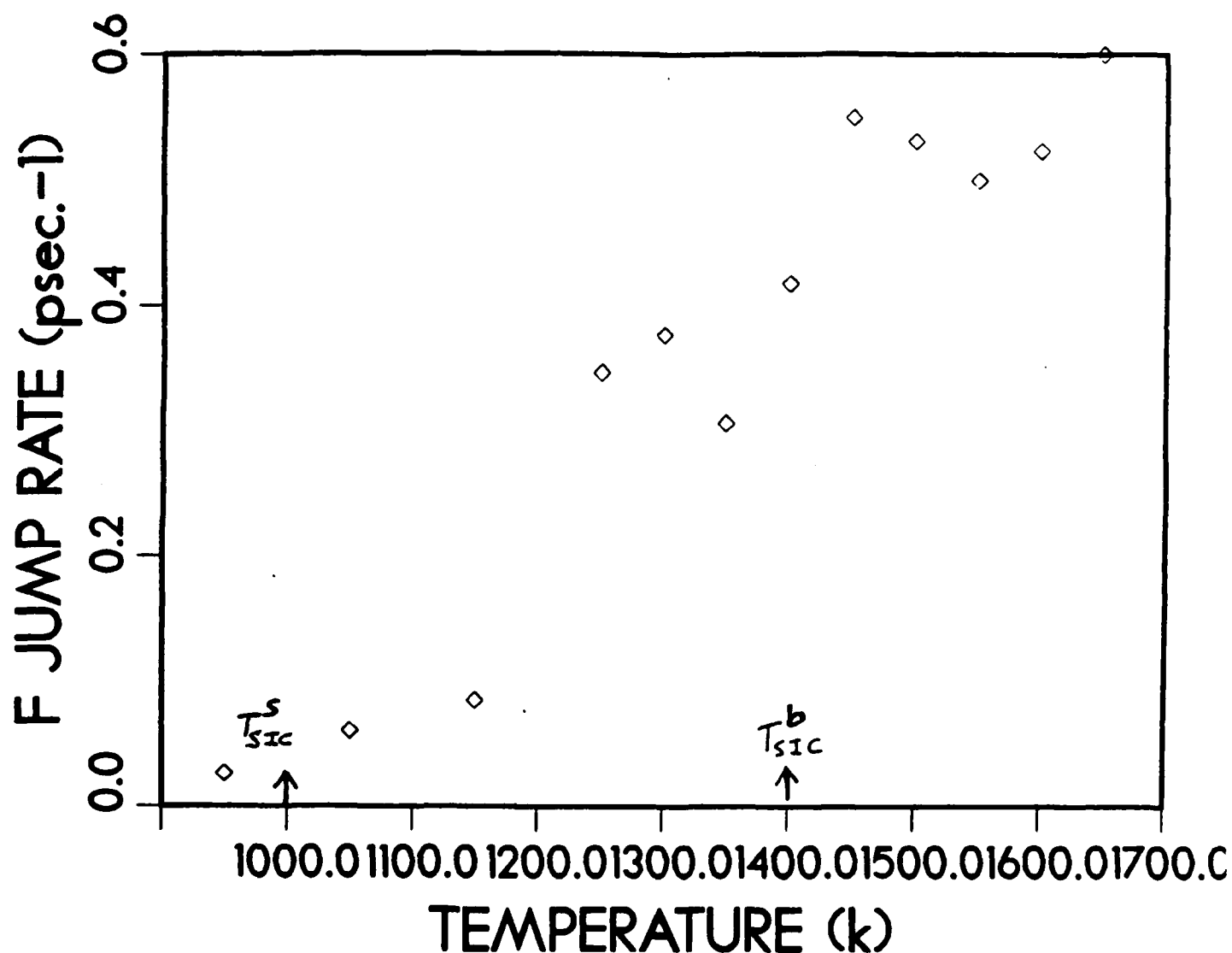
— Fig. 2a —

Surface 1st layer (111)



- Fig. 2b -

Surface 1st layer (110)

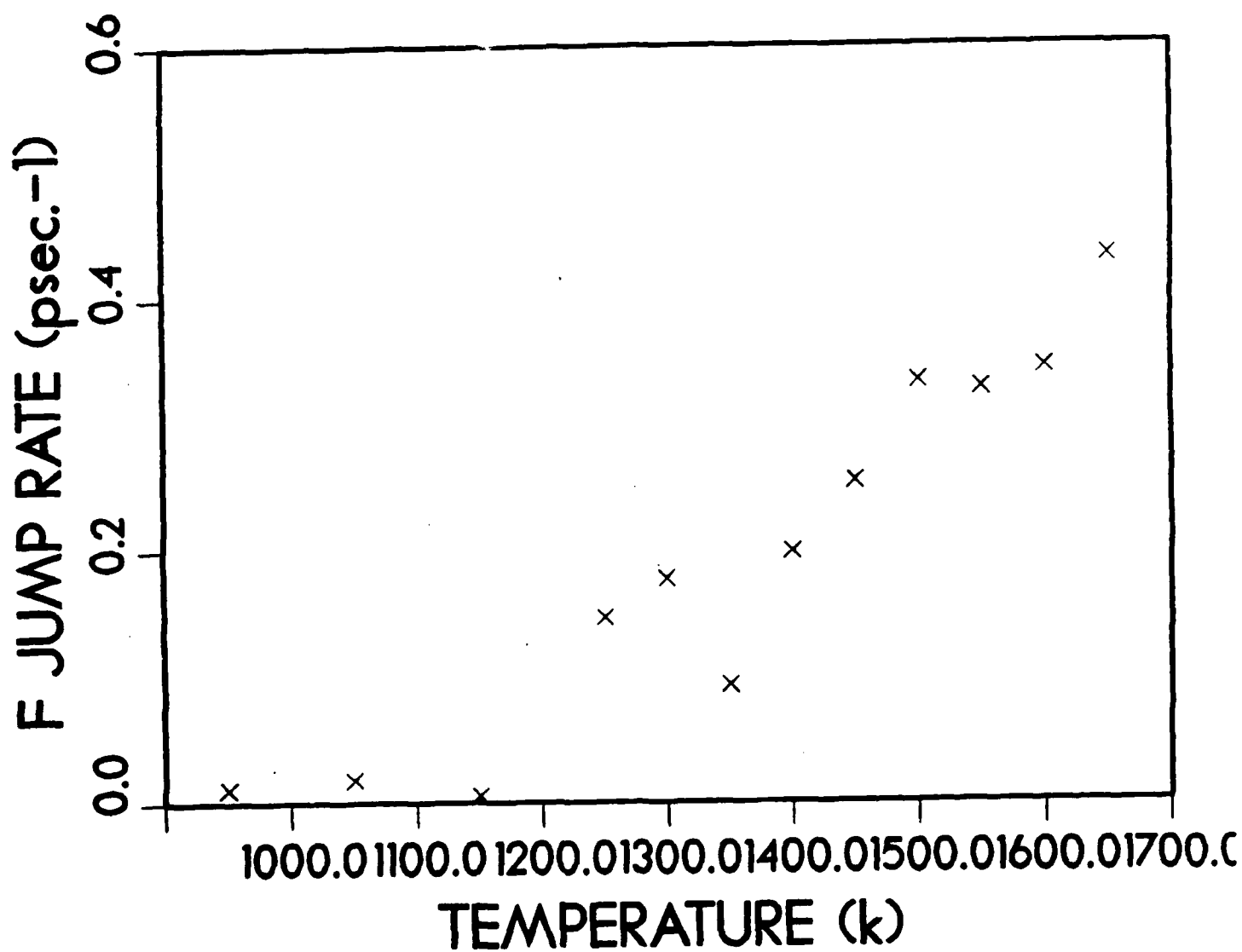


T_{SIC}^S — denotes the onset temperature
for surface superionic conductivity

Note the onset of superionic conductivity below T_{SIC}^b
(compare to Fig. 2a)

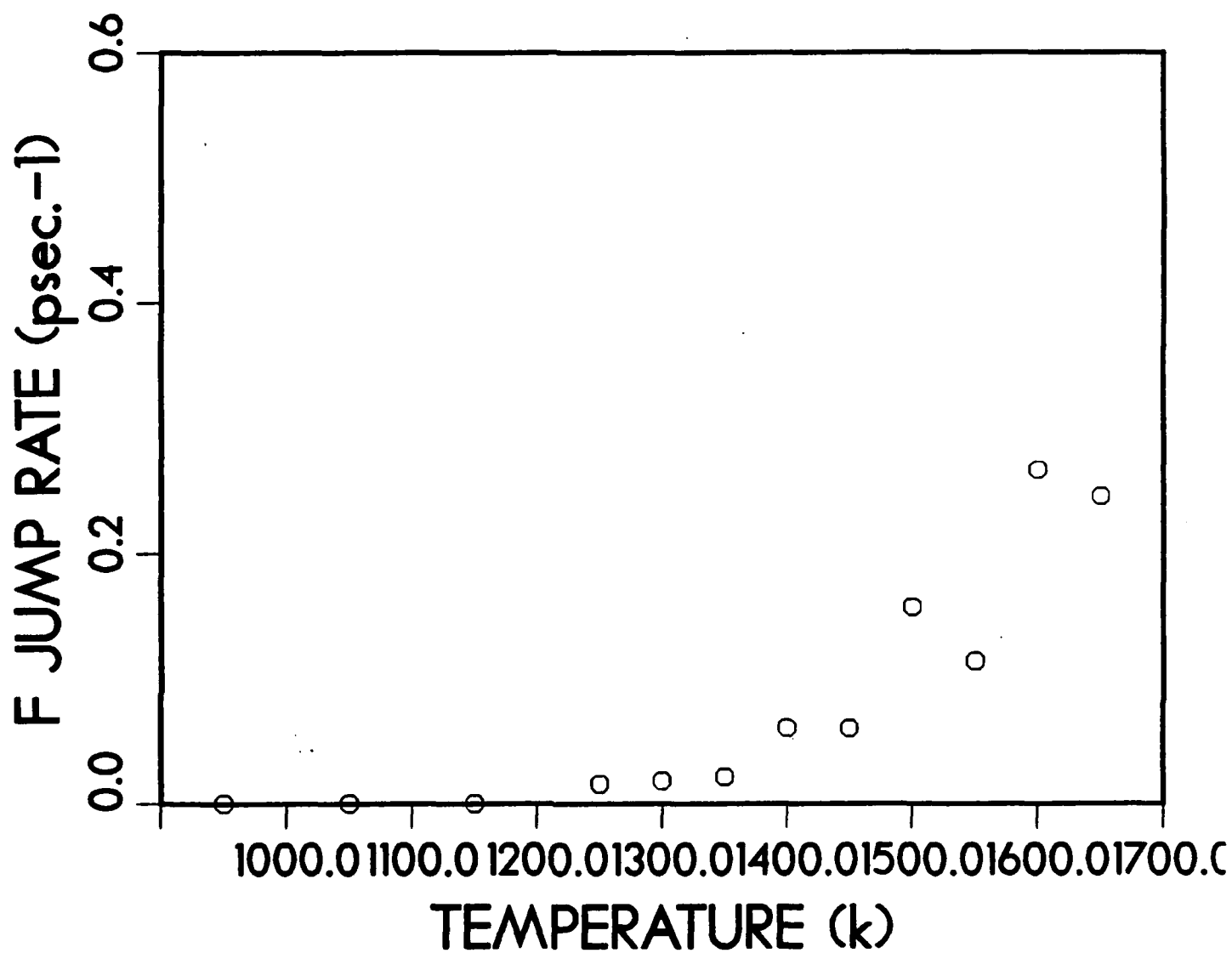
— Fig. 2c —

surface 2nd layer(110)



— Fig. 2d —

Surface 4th layer (110)



- Fig. 2e -

3. CONFERENCES AND SYMPOSIA PRESENTATIONS

1. Invited talk (U.L.) at the ONR Workshop on "New Theoretical and Computational Approaches to the Structure and Properties of Cracks in Solids", NIST, Washington, D.C., September 1989.
2. Invited talk (U.L.) at International Workshop on "Many-Atom Interactions in Solids", Pajulahti, Finland, June 1989.
3. AFOSR Molecular Dynamics Contractors Meeting, Captiva Island, Florida, November 1989.
4. Invited talk (U.L.) at the Gordon Conference on "Fundamentals of Tribology", New Hampshire, June 1990.
5. Invited talk (U.L.) at the "International Conference of Scanning Microscopy and Nanoscience", Baltimore, Maryland, July 1990.

pieces that will leave a residue.

Having dismissed polyols, Jung turned to a new base stock whose composition is proprietary information. Although this material does decompose at 700°F, it leaves little residue. Further, although the oil burns, it burns so slowly that oil loss is not a problem, says John Fairbanks of the Department of Energy, who oversees the joint Akzo/Cummins program. Only the thin film of oil along the top ring of the piston at the top of its stroke burns, so the oil losses are not much more than the losses of a conventional oil in a conventional engine.

Along with the base stock, Jung also developed a package of additives based on theoretical considerations. For instance, he says, inorganic chemistry can be used to predict which products are going to attach themselves most firmly to the metal engine parts and thus serve as useful antiwear additives.

Cummins has already tested the synthetic lubricant that Jung developed, and so far it looks like it will not only be a good high-temperature oil but that at lower temperatures it will be far superior to conventional oils, Fairbanks says. In one test, Cummins ran the oil for 300 hours at a top temperature of 850°F, and it had virtually no ash deposit and relatively little oil loss, Fairbanks says. Jung adds that it could be available commercially within a few years and that it will be priced about the same as current synthetic automobile oils, such as Mobil-1.

As a bonus, the new lubricant should help reduce automotive pollution, Fairbanks says. "In conventional engines, 30% to 60% of the particulate emissions come from lubricants," he says. But the Akzo lubricant "should volatilize directly into a gas and not form particulates, which will play a major role in reducing emissions."

At the Midwest Research Institute, Sutor also decided that hotter engines would demand a new approach to designing lubricants. "We got tired of trying what you can get off the shelf," Sutor says. So 2 years ago he went "back to first principles" and designed a lubricant "from a clean sheet of paper."

Like Jung, Sutor decided additives were to blame for much of the deposit formation and designed a new set of additives. Unlike Jung, he decided to try to make his base stock more resistant to oxidation. For instance, since longer chain lengths make the molecule more prone to oxidation, he chose a base stock with shorter chain lengths.

Then he went to chemistry to see if he could protect the sites on the base stock molecules that were particularly prone to oxidation. The oxidative attack comes at a particular spot on the chain, he discovered,

Getting a Grip on Rubbing Bodies

For most of its history, the "science of rubbing bodies" has been an empirical profession—more engineering than predictive science. "There is no unified theory of tribology," says Irwin Singer, a tribologist at the Naval Research Laboratory. And although tribologists believe they understand friction, wear, and lubrication qualitatively, they cannot usually make numerical predictions except by relying on models derived from experimental data.

In the past few years, several theorists have set out to remedy this situation. Their goal is to understand enough about what happens at a molecular level when two surfaces move against each other to be able to suggest new directions and new approaches on the experimental side of tribology. And, although the models they are developing cannot yet handle the complex interactions between surfaces and lubricants, the researchers believe they are laying the groundwork for true science.

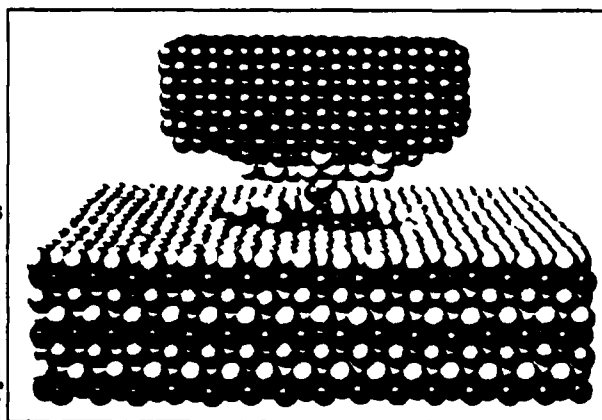
For example, Uzi Landman and David Luedtke, two physicists at Georgia Tech, have used molecular modeling on a Cray supercomputer to predict what will happen when the tip of a thin nickel needle is pushed down onto a flat gold surface and then lifted up again. In their model, the needle tip contained 2,000 nickel atoms, while the surface consisted of 8,000 gold atoms. The goal was to calculate the individual trajectories of all 10,000 atoms, which Landman and Luedtke did in two steps.

They first used basic quantum mechanics to determine the electrostatic potential in which each atom moves. "All of the questions of adhesion, cohesion, making of bonds, breaking of bonds—these are really quantum mechanics questions," Landman says. Once the researchers knew the potential, they could calculate the motion of each atom by a straightforward application of Newtonian physics. Straightforward, but definitely not simple. With 10,000 atoms involved, the supercomputer takes up to 150 hours to calculate a motion that in real time takes only a billionth of a second.

The computer simulation shows a quite peculiar action. As the nickel tip approaches the gold surface, the attractive force on the tip increases slowly. Then suddenly, when the tip is about 4 angstroms from the surface, the top layer of gold atoms on the surface breaks loose and bulges out to touch the tip. The gold atoms in the top layer of the surface are more strongly attracted to the nickel atoms in the tip than to their fellow gold atoms, Landman explains. If the tip is now retracted, it pulls a thin neck of gold atoms along with it. After this neck breaks, there is a one-atom-

thick coating of gold atoms on the nickel tip and the gold surface is left with one very thin column of atoms pointing up.

Nancy Burnham and Richard Colton at the Naval Research Laboratory subsequently used an atomic force microscope to check these calculations by observing the interaction between a nickel needle and a gold surface directly. And, Landman says,



Atomic attractions. As the nickel tip pulls away from the gold surface, it takes a layer of gold atoms (lighter spheres) with it.

the behavior they measured was exactly as predicted by the supercomputer.

Such simple theoretical models may be useful in understanding such things as how fractures form, Landman says, but the greater value will appear once researchers model much more complicated systems. "The stage is set for a full interaction between theory and experiment," Landman says. Eventually, he hopes that a theoretical understanding of the molecular forces between two surfaces or between a surface and a lubricant will give scientists a better understanding of what is going on at the macroscopic level. "To make progress in the molecular engineering of lubricants," he says, "you need to know the molecular details of the process." ■ R.P.

Dynamical simulations of stress, strain, and finite deformations

M. W. Ribarsky and Uzi Landman

School of Physics, Georgia Institute of Technology, Atlanta, Georgia 30332

(Received 31 May 1988)

Formulations and methodologies of molecular-dynamics simulations of material systems evolving under applied finite external perturbations are developed and discussed. Focusing on interfacial systems, composed of interfacing crystalline solids characterized by differing interatomic interactions and atomic sizes, the mechanisms and dynamics of response and stress relief in the elastic, plastic, and inelastic regimes are investigated. Critical values of the external perturbations (stress and strain) are determined, showing dependence on the nature of the interface and the ambient conditions (thermally adiabatic versus isothermal).

I. INTRODUCTION

Basic understanding of the structure and dynamics of materials and their properties often requires knowledge on a microscopic level of the underlying energetics and interaction mechanisms whose consequences we observe and measure. The structural, mechanical, and dynamical response of material systems to external stresses, on the atomic level, are key issues in developing a fundamental understanding of a number of systems and phenomena of coupled basic and technological interest such as tribology, lubrication, wear, material fatigue and yield, crack propagation, stress-induced phase and structural transformations, and hydrodynamical phenomena, to name just a few. Although the above-listed phenomena represent everyday experiences and have been observed and studied for a long time, detailed microscopic theories of them (with few exceptions) are lacking. Nevertheless large bodies of empirical data and in some cases phenomenological model descriptions have been developed.

Common observations related to the above phenomena, and of thermomechanical properties and response of materials in general, are usually made at the continuum level.¹ Consequently (and naturally) the development of theoretical understanding of these phenomena followed the "continuum modeling" approach.¹ The methodology of the development of these models is based on the principles of mass, momentum, and energy balance, and the formulation of constitutive equations. While the mathematical formulation of classical models of the mechanical response of matter (such as the classical theories of elasticity and hydrodynamics) achieved a high degree of sophistication, current focus is on the incorporation of the knowledge about the microscopic behavior of materials in continuum models which attempt to describe macroscopic observations. This is done via the introduction, into the continuum models, of a set of state variables which provide averaged (coarsened) representations of the relevant microscopic quantities. In addition we should note that most applied models of mechanical response are limited to the elastic (small spatial deformation) and linear (small rates of application of the external

perturbation) regimes. Attempts to incorporate inelastic response and nonlinear effects result in a great (often prohibitive) complexity.

Computer molecular-dynamics (MD) simulations²⁻⁹ where the evolution of a physical system is simulated, with refined temporal and spatial resolution, via a direct numerical solution to the model equations of motion are in a sense computer experiments which open new avenues in investigations of the microscopic origins of material phenomena. These methods alleviate certain of the major difficulties which hamper other theoretical approaches, particularly for complex systems such as those characterized by a large number of degrees of freedom, lack of symmetry, nonlinearities, and complicated interactions. In addition to comparisons with experimental data, computer simulations can be used as a source of physical information which is not accessible to laboratory experiments, and in some instances the computer experiment itself serves as a testing ground for theoretical concepts.

At this stage, the development and application of computer simulations to studies of materials phenomena, and in particular the mechanical, structural, and dynamical response of materials to external perturbations, can be used in order to investigate the microscopic mechanisms of material response and to determine the critical material parameters (cohesive energies, interaction potentials, atomic sizes, crystallographic structure) and ambient conditions (for example, thermally adiabatic versus isothermal conditions and dependencies on the strength and rate of applied external perturbations) which govern the observed trends. The information which can be obtained via microscopic simulations could then guide the formulation of continuum models, provide numerical values for certain physical material characteristic parameters which could be incorporated in such models, and provide guidance for the design and analysis of well-controlled experimental investigations.

Traditionally, MD simulations have been employed in studies of systems of fixed shape and size of the periodically replicated calculational cell (i.e., constant volume simulations). More recently methods for simulating systems in which the volume and shape of the calculational

cell may vary dynamically have been developed,¹⁰⁻¹⁵ opening the way to investigations of a large number of materials phenomena in which the dynamical freedom of the system to change volume and/or structure (or phase) is essential.¹⁵ In addition, a number of methods have been developed for simulations of flow and hydrodynamical systems,¹⁶⁻¹⁹ which allow detailed investigations of these nonequilibrium phenomena. Using molecular-dynamics techniques various studies of the mechanical properties of solids and fluids have been reported. Among the investigations of solid systems we note studies of stressed solids and crack propagation,²⁰⁻²⁵ dislocation energetics and dynamics,²³ structural transformations in crystal lattices under uniaxial tension or compression,^{11,15,26,27} sliding and migration of grain boundaries,¹⁵ simulations of plastic deformations and shock wave dynamics,^{28,29} studies of stressed interfaces,¹⁷ and calculations of elastic coefficients using MD simulations.³⁰

In this paper we investigate, using MD simulations the microscopic dynamical response, deformation, and stress-relief mechanisms at crystalline solid interfaces subject to externally applied perturbations. Studies of solid interfaces are of inherent as well as applied interest in the development of atomistic models of friction, solid lubrication, and wear phenomena, since plastic deformation which occurs in the vicinity of the interface between sliding materials is the principal mechanism for the dissipation of frictional work.¹ The objectives of these studies are (i) identification of the mechanisms for solid interfacial systems of deformation, stress accumulation and relief, and the dynamical response to external perturbations, (ii) identification of the dependence of the above phenomena on material characteristics, such as bonding strength, atomic sizes, and interface crystallography, and on ambient conditions (thermally adiabatic versus isothermal), and (iii) the development and critical assessment of MD simulation methods for investigations of the above phenomena. In Sec. II we discuss molecular-dynamics methodologies and techniques for simulations of finite deformations of material systems under stress. The setup of the systems and results of simulations using MD simulation methods, under several thermally adiabatic and isothermal conditions and for systems of different sizes and material characteristics are described and compared in Sec. III. A summary of our findings is given in Sec. IV.

II. MOLECULAR-DYNAMICS FORMULATION

In the molecular-dynamics (MD) method the equations of motion for a set of interacting particles are integrated numerically and properties of the system are obtained from the generated phase-space trajectories of the system.²⁻⁹ In the case of an extended system periodic boundary conditions (PBC's) are imposed while in simulations of finite aggregates⁶ no such device is used. The starting point of a MD simulation is a well-defined microscopic description of the physical system, in terms of a Hamiltonian or a Lagrangian from which the equations of motion are derived. In the early applications of the MD method to extended systems the simulations were

performed in the microcanonical (E, V, N) ensemble, i.e., the energy E , volume V , and number of particles N in the calculational cell (which is periodically repeated) are constants. The desire to investigate physical situations in which the volume and shape (geometry) of the material system may vary (in response to an external pressure or applied stress) as well as circumstances where isothermal (i.e., constant temperature T) pertain, motivated the development of new MD formulations, such as the ansatz Lagrangian,¹⁰⁻¹³ constrained dynamics,^{4,9} and the Nose-dynamics methods.⁹ In the following we review first the ansatz-Lagrangian method, as extended by Parrinello and Rahman¹¹ (PR) for calculations of systems under externally applied stresses, and its extensions to treat finite deformations.¹² Subsequently we discuss an alternative method for dynamical studies of deformations in which the system evolves under an imposed constant-strain rate. Finally, we describe a variant of the MD method for finite deformation studies and a general method which is particularly suited for investigations^{2,18,19} of systems in which flow phenomena may occur.

A. The ansatz-Lagrangian method: The (\mathcal{H}, τ, N) ensemble

In the PR formulation¹¹ the particles' coordinate vectors whose components are $r_{i\alpha}$ (where $i = 1, 2, \dots, N$ is a particle index and $\alpha = 1, 2, 3$ is a coordinate index) are expressed in terms of scaled coordinate vectors $s_{i\alpha}$ (where $0 \leq s_{i\alpha} \leq 1$, $i = 1, 2, \dots, N$ and $\alpha = 1, 2, 3$) and a matrix \underline{H} whose columns \underline{H}_1 , \underline{H}_2 , and \underline{H}_3 are the vectors \underline{A} , \underline{B} , \underline{C} which span the edges of the MD calculational cell,

$$r_{i\alpha} = \sum_{\beta=1}^3 H_{\alpha\beta} s_{i\beta} \quad (i = 1, 2, \dots, N; \alpha, \beta = 1, 2, 3). \quad (1)$$

The volume of the cell, Ω , is given by $\det(\underline{H}) \equiv |\underline{H}|$.

Regarding the components of the \underline{H} matrix as dynamical variables, Parrinello and Rahman¹¹ have originally proposed a Lagrangian (a Hamiltonian formulation can also be developed^{12,27}) from which the equations governing the time evolution of the $3N + 9$ degrees of freedom ($3N$ particle and nine calculational cell degrees of freedom) are obtained:

$$L_{PR} = \frac{1}{2} \sum_{i=1}^N [m_i \dot{s}_i^T \underline{G} \dot{s}_i - U(\{\underline{H} s_i\})] + K_{\text{cell}} - U_{\text{cell}}, \quad (2)$$

where dotted variables indicate differentiation with respect to time, the superscript T denotes a transpose, the metric tensor \underline{G} is defined as $\underline{G} = \underline{H}^T \underline{H}$, U is the potential energy of the particles (which depends on the specific form of the interparticle interaction), and the cell kinetic energy was chosen by PR as

$$K_{\text{cell}} = \frac{1}{2} W \text{Tr}(\dot{\underline{H}}^T \dot{\underline{H}}), \quad (3)$$

where W is a mass parameter. For the case of a system to which an external stress, specified by the stress tensor \underline{g} , is applied the potential energy, U_{cell} , is given by

$$U_{\text{cell}} = \Omega_0 \text{Tr}(\underline{g} \underline{\epsilon}), \quad (4)$$

where the strain tensor $\underline{\epsilon}$ can be written in terms of the metric tensor \underline{G} and the reference value, \underline{H}_0 , of \underline{H} , in the form

$$\underline{\epsilon} = \frac{1}{2}[(\underline{H}_0^{-1})^T \underline{G} \underline{H}^{-1} - \mathbf{1}]. \quad (5)$$

Using Eq. (5) in Eq. (4), and denoting by $P_e \equiv \frac{1}{3}\text{Tr}(\underline{q}_e)$ the external hydrostatic pressure, the expression for U_{cell} in the small-strain limit¹¹ [i.e., $\text{Tr}(\underline{\epsilon}) \simeq (\Omega - \Omega_0)/\Omega_0$] is

$$U_{\text{cell}} = P_e(\Omega - \Omega_0) + \frac{1}{2}\text{Tr}(\underline{\Sigma} \underline{G}), \quad (6)$$

where

$$\underline{\Sigma} = \Omega_0 \underline{H}_0^{-1}(\underline{q}_e - P_e \mathbf{1})(\underline{H}^{-1})^T \quad (7)$$

and $\Omega_0 = \det(\underline{H}_0)$. Note that for the case of an isotropic external stress $\underline{\Sigma} = 0$, the second term in Eq. (6) vanishes and only the contribution from the hydrostatic pressure, P_e , remains.

The equations of motion which are derived in the usual manner from the above Lagrangian [Eq. (2)] for the particles are

$$m_i \ddot{\mathbf{s}}_i = - \sum_{j=1}^N \chi_{ij}(\mathbf{s}_i - \mathbf{s}_j) - m_i \underline{\dot{G}}^{-1} \underline{\dot{G}} \mathbf{s}_i \quad (i = 1, 2, \dots, N), \quad (8a)$$

where $\chi_{ij} = r_{ij}^{-1}(\partial U / \partial r_{ij})$, and those describing the dynamical motion of the calculational cell are given by

$$W \ddot{\underline{H}} = (\underline{q} - P_e \mathbf{1}) \underline{A} - \underline{H} \underline{\Sigma}, \quad (8b)$$

where \underline{A} is the "area tensor," $\underline{A} = \Omega(\underline{H}^{-1})^T$ [i.e., $A_{\alpha\beta} = \partial \Omega / \partial H_{\alpha\beta}$], and the elements of the internal microscopic stress tensor \underline{q} are given by

$$\sigma_{\alpha\beta} = \Omega^{-1} \left[\sum_{i=1}^N \left[p_i \alpha p_i \beta / m_i - \sum_{j=i+1}^N \chi_{ij} r_{ij} \alpha r_{ij} \beta \right] \right] \quad (\alpha, \beta = 1, 2, 3) \quad (8c)$$

where $r_{ij} = |\mathbf{r}_i - \mathbf{r}_j|$ and the momentum $\mathbf{p}_i = m_i \underline{H} \dot{\mathbf{s}}_i$.

The above formulation generates an isoenthalpic-isostress $(\mathcal{H}, \sigma_e, N)$ ensemble (\mathcal{H} is the enthalpy) with the elastic energy given by [see Eq. (6)]

$$\begin{aligned} E_{el} &= P_e(\Omega - \Omega_0) + \Omega_0 \text{Tr}[(\underline{q}_e - P_e \mathbf{1}) \underline{\epsilon}] \\ &= P_e(\Omega - \Omega_0) + \frac{1}{2} \text{Tr}(\underline{\Sigma} \underline{G}). \end{aligned} \quad (9)$$

The sum of E_{el} and the particle kinetic and potential energies is a constant of the motion in this formulation.^{11,12}

Two issues raised at this point are (i) the appropriate choice of the reference state \underline{H}_0 ^{11,12} [see Eq. (5)], and (ii) the nonuniqueness¹² of the form for K_{cell} [Eq. (3)]. Considering issue (i) first it is noted that as far as the definition of the strain tensor $\underline{\epsilon}$ [Eq. (5)] is considered the choice of \underline{H}_0 is arbitrary.^{11,12} However, the choice of the reference system is of importance when considering the elastic energy, particularly when *finite deformations* are involved.¹² An expression for the virtual work δE performed in a virtual deformation (i.e., the elastic energy stored in the medium) of a deformable medium, whose volume in the deformed state is Ω , was derived by Mur-

naghan,³¹

$$\delta E \equiv E_{el} = \int_{\Omega} \text{Tr}[(\underline{H}_0 \underline{H}^{-1} \underline{q}_e \underline{H}^{-1T} \underline{H}_0^T) \delta \underline{\epsilon}] d\Omega, \quad (10)$$

with the strain tensor $\underline{\epsilon}$ defined by Eq. (5) and the *unstressed system*, \underline{H}_0 , as the *reference state*. The integral is to be performed over the final state, i.e., stressed body. The "calculational cell tensors" \underline{H}_0 and \underline{H} for the unstressed and stressed system, respectively, occur in Eq. (10) since a position \mathbf{r} in the deformed system relates to the corresponding position \mathbf{r}_0 in the undeformed body via the Jacobian $\underline{H} \underline{H}_0^{-1}$, i.e., $\mathbf{r} = \underline{H} \underline{H}_0^{-1} \mathbf{r}_0$. In the limit of the infinitesimal theory of elasticity Eq. (10) becomes

$$E_{el} = \int_{\Omega} \text{Tr}(\underline{q}_e \delta \underline{\epsilon}) d\Omega. \quad (11)$$

For a uniform system undergoing a *finite deformation* Eq. (10) takes the form

$$E_{el} = \Omega_0 \text{Tr}(\underline{\tau} \underline{\epsilon}), \quad (12)$$

where the "thermodynamic tension" $\underline{\tau}$ is defined^{31,32} by

$$\underline{\tau} = \frac{\Omega}{\Omega_0} \underline{H}_0 \underline{H}^{-1} \underline{q}_e (\underline{H}^{-1})^T \underline{H}_0^T. \quad (13)$$

For the *infinitesimal* case we obtain

$$E_{el} = \Omega_0 \text{Tr}(\underline{q}_e \underline{\epsilon}). \quad (14)$$

We emphasize that in Eq. (12) the reference state, \underline{H}_0 , is the *unstressed system*. In Eq. (14) however, the reference state is a system *under stress* and as proposed by PR,¹¹ in this case \underline{H}_0 could be chosen as the average of the stressed system, $\langle \underline{H} \rangle$. Since the thermodynamic tension $\underline{\tau}$ is the quantity appearing in the thermodynamic expressions,^{31,32} e.g., the enthalpy $\mathcal{H} = E + \Omega_0 \text{Tr}(\underline{\tau} \underline{\epsilon})$, where E is the particle energy, Ray and Rahman¹² proposed the isoenthalpic-isotension, (\mathcal{H}, τ, N) , ensemble where τ is constant [but not \underline{q}_e , see Eq. (13)]. For this ensemble the equations of motion for the particles are as given by Eq. (8a) and the equation for \underline{H} [Eq. (8b)] is replaced by

$$W \ddot{\underline{H}} = \underline{q} \underline{A} - \underline{H} \underline{\Gamma}, \quad (15a)$$

where

$$\underline{\Gamma} = \Omega_0 \underline{H}_0^{-1} \underline{\tau} (\underline{H}_0^{-1})^T. \quad (15b)$$

In some of the simulations discussed in the next section we have used the (\mathcal{H}, τ, N) ensemble. In the following section we formulate an alternative dynamical simulation method in which the system evolves under a constant-strain rate.

B. Constant-strain-rate simulations

In the constant-strain-rate (CSR) simulations the calculational cell deforms in a *prescribed way at a prescribed constant rate*. In this method only the particle equations of motion need to be solved since the evolution of the calculational box is given, i.e., the components of \underline{H} do not evolve freely. We remark that since for a given deformation (i.e., prescribed strain) the internal stresses, \underline{q} , see Eq. (8c), which the system develops (in equilibrium, or steady state in case of flow) in response to the deforma-

tion can be calculated, the CSR and (\mathcal{H}, τ, N) ensemble (see Sec. II A) simulations can be operated "self-consistently" by using these calculated stresses as applied external stresses in simulations where the dynamical evolution of the calculational cell is included^{11,12} (i.e., using the (\mathcal{H}, τ, N) ensemble, or the isoexternal-stress method described in Sec. C). The formulation of the CSR method is facilitated by defining the streaming velocity, \mathbf{u} , as

$$\mathbf{u} = \dot{\mathbf{H}} \mathbf{s} . \quad (16)$$

Using this definition the strain-rate tensor, $\dot{\gamma}$, is given by

$$\dot{\gamma} \equiv \nabla \mathbf{u} = (\mathbf{H}^{-1})^T \dot{\mathbf{H}}^T . \quad (17)$$

The equations of motion for the particles can be now written [compare to Eq. (8a)] as

$$\dot{\gamma} \equiv \nabla \mathbf{u} = (\mathbf{H}^{-1})^T \dot{\mathbf{H}}^T . \quad (17)$$

The equations of motion for the particles can be now written [compare to Eq. (8a)] as

$$m_i \dot{\mathbf{H}} \dot{\mathbf{s}}_i = - \sum_{j=1}^N \chi_{ij} \mathbf{r}_{ij} - (\mathbf{H}^{-1})^T \dot{\mathbf{H}}^T \mathbf{p}_i - m_i \dot{\mathbf{H}} \dot{\mathbf{s}}_i , \quad (18)$$

where the peculiar momentum \mathbf{p}_i is defined by

$$\mathbf{p}_i = m_i \dot{\mathbf{H}} \dot{\mathbf{s}}_i \quad (19a)$$

and

$$\dot{\mathbf{p}}_i = m_i (\dot{\mathbf{H}} \dot{\mathbf{s}}_i + \dot{\mathbf{H}} \dot{\mathbf{s}}_i) . \quad (19b)$$

Rearranging terms and using Eqs. (19), we write Eq. (18) as

$$\dot{\mathbf{p}}_i = - \sum_{j=1}^N \chi_{ij} \mathbf{r}_{ij} - \dot{\gamma} \mathbf{p}_i \quad (20)$$

and

$$\dot{\mathbf{r}}_i = \mathbf{p}_i / m_i + \dot{\gamma}^T \mathbf{r}_i . \quad (21)$$

We note that Eq. (20) is the same as the "Doll's tensor" equation of motion introduced by Evans and Hoover.¹⁶

As discussed by Ray and Rahman,¹² in the ansatz Lagrangian [Eq. (2)], terms involving $\dot{\mathbf{H}} \dot{\mathbf{s}}_i$ are omitted. Employing a Hamiltonian formulation these authors derived¹² an alternative equation of motion which includes the $\dot{\mathbf{H}} \dot{\mathbf{s}}_i$ terms [see Eq. (2.12) in Ref. 12],

$$m_i \dot{\mathbf{H}} \dot{\mathbf{s}}_i = - \sum_{j=1}^N \chi_{ij} \mathbf{r}_{ij} - m_i \ddot{\mathbf{H}} \dot{\mathbf{s}}_i - 2 m_i \dot{\mathbf{H}} \dot{\mathbf{s}}_i . \quad (22)$$

For a process in which the system is deformed at a constant strain rate, $\dot{\gamma}$ is constant for a Couette geometry (i.e., fluid sheared between two parallel plates held at a fixed distance from one another, see Sec. III C), the term involving $\ddot{\mathbf{H}}$ in Eq. (22) vanishes and using the definitions of $\dot{\gamma}$ [Eq. (17)] and the peculiar momentum, \mathbf{p}_i [Eq. (19a)], the above equation of motion becomes

$$\dot{\mathbf{p}}_i = - \sum_{j=1}^N \chi_{ij} \mathbf{r}_{ij} - \dot{\gamma}^T \mathbf{p}_i . \quad (23)$$

We remark that this equation involves the transpose of $\dot{\gamma}$ [compare to Eq. (20)], and is the same as the local-rest-frame dynamics ("Slod") equation of motion (transpose of the non-Newtonian dynamics "Doll's tensor") suggested and used by Evans and Morris.¹⁶

Thus we observe that for constant-strain rate the equations of motion generated via the Parrinello and Rahman,¹¹ and Ray and Rahman¹² formulations reduce to those used in the nonequilibrium-molecular-dynamics (NEMD) method.¹⁶ In the constant-strain-rate (CSR) simulations described below we have used Eqs. (23), following NEMD studies. However, we remark that simulations employing Eqs. (20) yield qualitatively similar results.

C. Isoexternal-stress formulation

In the previous two sections we discussed methods for molecular-dynamics simulations of system which undergo finite deformations, i.e., the isoenthalpic-isotension, (\mathcal{H}, τ, N) ensemble, and constant-strain-rate (CSR) methods. In order to allow simulations of systems under *constant external stress*, $\underline{\sigma}_e$, we have developed a new method which in addition avoids certain pathological circumstances which may be encountered when using the previous methods, particularly when flow develops. While we do not use this method of simulations in this paper, we include a brief discussion of it for completeness.

In order to develop an isoexternal-stress dynamical method, we consider the Lagrange equations of motion which include nonconservative forces,³³ \mathbf{Q}_i ,

$$\frac{d}{dt} \left[\frac{\partial L}{\partial \dot{q}_{i\alpha}} \right] - \left[\frac{\partial L}{\partial q_{i\alpha}} \right] = Q_{i\alpha} , \quad (24)$$

$$(\alpha = 1, 2, 3)(i = 1, 2, \dots, N + 9) ,$$

where the set of q_i 's and \dot{q}_i 's include the dynamical degrees of freedom of the particles and of the calculational cell. The virtual work, δE , done by the nonconservative forces is given by

$$\delta E = \sum_i \mathbf{Q}_i \cdot \delta \mathbf{q}_i . \quad (25)$$

Recalling the definition of the area tensor, $\underline{\mathcal{A}}$ [see Eq. (8b)] we note that the components $(\mathbf{A}_1, \mathbf{A}_2, \mathbf{A}_3)$ of $\underline{\mathcal{A}}$ are the areas of the calculational cell times their respective normals (i.e., $\mathbf{A}_1 = \mathbf{H}_2 \times \mathbf{H}_3$, etc.). Therefore due to a virtual deformation of the calculational cell (in which the vectors \mathbf{H}_α are changed by $\delta \mathbf{H}_\alpha$) each of the surfaces \mathbf{A}_α is displaced by $\delta \mathbf{H}_\alpha$. The amount of virtual work done in displacing each of the surfaces due to the force $\underline{\sigma}_e \mathbf{A}_\alpha$ is $\delta \mathbf{H}_\alpha^T \underline{\sigma}_e \mathbf{A}_\alpha$ (for $\alpha = 1, 2, 3$). For a general virtual displacement $\delta \underline{\mathcal{H}}$ the virtual work done is

$$\delta E = \text{Tr}(\delta \underline{\mathcal{H}}^T \underline{\sigma}_e \underline{\mathcal{A}}) , \quad (26)$$

which can be shown to be the same as the result given in Eq. (10) for a uniform system. Comparing Eqs. (25) and (26) the Lagrange equations of motion [Eq. (24)] for the calculational cell take the form

$$\frac{d}{dt} \left[\frac{\partial L}{\partial \dot{H}_{\alpha\beta}} \right] - \frac{\partial L}{\partial H_{\alpha\beta}} = \sum_\gamma \sigma_{e,\alpha\gamma}(t) \mathbf{A}_{\gamma\beta} \quad (\alpha, \beta = 1, 2, 3) , \quad (27)$$

where we have denoted the q 's and \dot{q} 's corresponding to the calculational box by H and \dot{H} and the possible depen-

dence of the external stress tensor, $\underline{\sigma}_e$, on time is indicated. Using the Lagrangian given in Eq. (2), but without the term U_{cell} which is explicitly accounted for in Eq. (27), equations of motion for the calculational cell tensor, \underline{H} can be derived yielding,

$$W\ddot{\underline{H}} = (\underline{\sigma} - \underline{\sigma}_e) \underline{A}, \quad (28)$$

in place of Eq. (8b), or (15a) in the previous formulations. The particle equations of motion remain unchanged [Eq. (8a)]. Note that here $\underline{\sigma}_e$ is *constant* unlike the case of the (\mathcal{H}, τ, N) ensemble equations of motion and that the question of reference state does not arise. The system however is nonconservative.

We turn next to the issue of the nonuniqueness of the form of the calculational cell kinetic energy, K_{cell} [see Eqs. (2) and (3)]. This question has been addressed before and it has been shown that any form for K_{cell} which is a function of \underline{H} and $\dot{\underline{H}}$ generates the isoenthalpic-isobaric ensemble for sufficiently large N .¹² Furthermore, note that for such choices the particle equations of motion [Eq. (8a)] are independent of K_{cell} as are also equilibrium equal-time ensemble averages.^{16,12}

It is natural to demand that the equations of motion governing the dynamical evolution of the system will be invariant under transformations connecting equivalent computational cells¹⁹ (which may differ in shape but are of the same volume, and contain equivalent sets of particles). Since $\underline{H} \equiv (\underline{H}_1, \underline{H}_2, \underline{H}_3)$, defining the computational cell, fully incorporates the periodicity of the system, i.e., any two equivalent points in the periodically replicated system may be connected by a vector $n_1 \underline{H}_1 + n_2 \underline{H}_2 + n_3 \underline{H}_3$ where n_1, n_2 , and n_3 are integers, we define¹⁹ the class of transformations under which the system is translationally invariant as T transformations. These transformations have the property that all the elements of the (3×3) transformation matrix \underline{T} are integers and that $\det(\underline{T}) = 1$ (to assure conservation of volume).

It has been recently shown¹⁹ that previous choices for K_{cell} [such as the Parrinello-Rahman form,¹¹ Eq. (3), and variants thereof¹²] lead to equations of motion for the calculational cell which do not obey the above invariance requirement. Moreover, it has been shown that using K_{cell} given by

$$K_{\text{cell}} = \frac{1}{2} W \text{Tr}(\dot{\underline{H}} \underline{A}^T \underline{A} \dot{\underline{H}}^T), \quad (29)$$

generates equations of motion invariant under T transformations and in addition leads to satisfaction of the virial theorem at equilibrium (where it is appropriate, i.e., isotropic pressure $\underline{\sigma}_e = \frac{1}{3} P_e \underline{1}$).

In addition to providing a more complete description by virtue of obeying a natural invariance requirement, this formulation presents a technical advantage which is of importance particularly in simulations of flow systems.¹⁸ Consider, for example, a fluid flowing under the influence of an external stress under steady-state conditions. For concreteness take the external stress tensor $\underline{\sigma}_e$ to be a symmetric tensor $\sigma_{\alpha\beta} = C(\delta_{\alpha 1} \delta_{\beta 3} + \delta_{\alpha 3} \delta_{\beta 1})$, where C is an arbitrary constant. Under the influence of the external stress the calculational cell will eventually be-

come extremely nonorthogonal (in fact due to the absence of effective resistance to flow, such skewed calculational cell may develop in fluid simulations even without external stresses). Suppose that the interparticle interaction potentials in the system extend to a finite range smaller than the linear dimension of the calculational cell. Then in calculating the force acting on particle i we need to include contributions from all particles located inside the range of interaction in the calculational cell and from their images in the first (so-called minimum image) periodic replications of the cell. As long as the calculational cell does not deviate much from being cubical (i.e., orthogonal) the search for periodic images can be implemented most efficiently by finding the nearest integer to each component of the scaled coordinates [see Eq. (1)], $s_j - s_j$. However, for very skewed cells there is no such efficient procedure and since this segment of the calculation is one of the most time consuming parts of the simulation this poses a serious impediment. A solution to this problem is to transform, in the course of the simulation, the skewed cell to an equivalent one which is more orthogonal, as often as necessary. This transformation involves only the small number of degrees of freedom associated with the calculational cell (\underline{H}). Of course, in order to afford such transformations one must require that the equations of motion governing the system evolution be invariant under these transformations, which is achieved via the choice of K_{cell} given in Eq. (29). Recent simulations in our laboratory¹⁸ of stressed systems beyond the yield point and of sheared fluids support the usefulness of the new method.

III. RESULTS

To investigate the properties and the dynamics, energetics and response of a solid to externally imposed forces we have performed molecular-dynamics simulations on a model system at different ambient conditions. To illustrate the different simulation modes discussed in the previous section we compare results obtained for systems in which the calculational cell was allowed to respond dynamically to an external thermodynamic tension (see Sec. II A) with those obtained for a calculational cell which is deformed (keeping the volume unchanged) at a constant-strain rate (the CSR method described in II B). The two simulation modes illustrate various aspects of the deformation process and the approach of the system to yield. The dynamical cell mode of simulation may be likened to the situation where a load and shear stress are applied to materials in frictional contact, resulting in processes which are accompanied by volume changes, while the constant-strain-rate mode corresponds to experiments in which a material pressed between two parallel moving plates (slabs, which are kept at constant distance) is strained. As the stress on the solid system is increased, or equivalently as the strain is increased, the materials deform, first elastically and then inelastically culminating in yield when a disruption of the material occurs. In this paper we investigate the response of the solid as it approaches the yield point. Studies beyond yield require a modification of the simulation procedure (see Sec. II C) and will be discussed elsewhere.¹⁸

A. System setup

In this study we focus on the mechanisms and dynamics of the response of a system containing an interface between two materials to external stresses. The model system which we employ in our simulations consists of N particles (N_A of type A and N_B of type B , $N_A + N_B = N$) interacting via pairwise 6-12 Lennard-Jones (LJ) potentials

$$V(r) = 4\epsilon_{\alpha\beta} \left[\left(\frac{\sigma_{\alpha\beta}}{r} \right)^{12} - \left(\frac{\sigma_{\alpha\beta}}{r} \right)^6 \right] \quad (\alpha, \beta) = A, B, \quad (30)$$

where A and B represent two types of materials. The solid is set up initially in a face-centered-cubic crystalline structure, with N_L (111) layers (N/N_L particles per layer) with the z axis along the [111] direction,³⁴ and three-dimensional periodic boundary conditions are used (see Fig. 1). The well-depth parameter ($\epsilon_{\alpha\beta}$) of the interaction potential between particles in layers $1-N_{LA}$ is taken to be twice that for particles in layers $N_{LA}+1-N$ (i.e., $\epsilon_{AA} = 2\epsilon_{BB}$) corresponding to a soft, solid, lubricating material (the B system) pressed between hard-material slabs (the A system). In order to isolate the dependence of the system response on the interaction strength (potential depth) parameter, ϵ , from that due to differences in the atomic sizes (and thus interatomic distances) associated with the parameter σ in the LJ potential, we have performed first simulations in which $\epsilon_{AA} = 2\epsilon_{BB}$ and $\sigma_{AA} = \sigma_{BB}$, and then simulations in which $\sigma_{BB} = 1.5\sigma_{AA}$. The interspecies LJ potential parameters were chosen as $\sigma_{AB} = (\sigma_{AA} + \sigma_{BB})/2$ and $\epsilon_{AB} = (\epsilon_{AA}\epsilon_{BB})^{1/2}$. In the following we use reduced units³⁵ where energy and temperature are expressed in units of ϵ_{AA} , length in units of σ_{AA} , stress in units of $(\epsilon_{AA}/\sigma_{AA}^3)$, and the time unit (t.u.) is $(m_A/\epsilon_{AA})^{1/2}\sigma_{AA}$. In the integration of the equations of motion we used a time step $\Delta t = 0.0075$ t.u. where

$$\text{t.u.} = (m_A/\epsilon_{AA})^{1/2}\sigma_{AA},$$

which results in energy conservation (to six significant figures) for extended runs.

In most of our simulations we have used systems consisting of $N = 1260$ particles with 18 (111) layers (N_L) and $N_{LA} = N_{LB} = 9$ (unless specified differently results are for this size systems). However, in order to investigate and assess system size dependencies we have also carried out comparative simulations for systems containing $N = 1890$ particles with $N_{LA} = 9$ (i.e., $N_A = 630$) and $N_{LB} = 18$ (i.e., $N_B = 1260$). Some results from these simulations will be exhibited when the size dependence is discussed.

B. Applied thermodynamic-tension simulations: (\mathcal{H}, τ, N) ensemble

1. Adiabatic conditions

In all our simulations we equilibrate first the initial system at a reduced temperature of $T = 0.11$ (note that a

pure bulk LJ crystal melts at $T \approx 0.7$, and thus, since $\epsilon_{BB} = \epsilon_{AA}/2$, the bulk melting point of the soft material, B , is half that of the A material). Subsequently we apply to the system a load along the [111] (z) direction (normal to the interface, as shown in Fig. 1) at a rate of $0.0025(\epsilon/\sigma^3)/\Delta t$ until a load value of 0.5 is reached. Following equilibration under this load we apply to the system a thermodynamic tension τ in the $[1\bar{1}0]$ direction (see Fig. 1) at a rate of $\dot{\tau}_{xx} = 0.00125(\epsilon/\sigma^3)/\Delta t$ and follow the evolution of the system until it fails [to keep the system against a rigid rotation a symmetric thermodynamic tension tensor τ is applied (i.e., $\tau_{xx} = \tau_{yy}$)].

To investigate the dependence on the thermal ambient conditions we distinguish between simulations where the system is thermally isolated during the application of the shear [discussed in (1)] and simulations where isothermal conditions are maintained [discussed in (2)]. The temporal history of the applied tension versus time for the adiabatic and isothermal conditions are shown in Figs. 2(a) and 2(b), respectively. As the system evolves under the applied shear it develops internal stresses which are calculated using the positions and forces on the particles using Eq. 8(c). For a rate of increase of the applied external shear which is much smaller than the characteristic relaxation rates of the material the system would evolve on a phase-space trajectory which corresponds to an equilibrium (or quasiequilibrium) path for which the values of the external and internal stresses are equal along the system evolution. For externally applied thermodynamic tension above a certain critical value [τ_c and the corresponding calculated critical external stress σ_c , see Eq. (13)] failure of the system will occur, evidenced by a drop of the internal stresses to zero (i.e., stress relief) and an unbounded variation of the volume of the system. Since the rate of increase of the applied thermodynamic tension, τ , indicated by the solid line (slanted) in Fig. 2, is not slow enough to allow the system to relax at all times, the critical values thus obtained serve only as rough estimates (upper bounds) to the true, quasistatic, critical values. Therefore, to obtain a more accurate estimate of the critical stress we have performed simulations at constant values of the thermodynamic tension indicated by

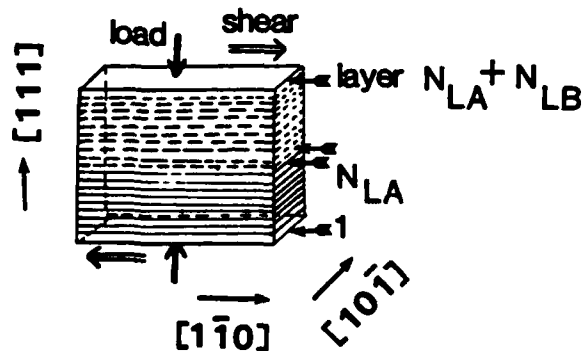


FIG. 1. A schematic of the calculational cell. N_{LA} is the number of layers in the A (hard) material and N_{LB} the number of layers in the B (soft) material. The interface is between layers N_{LA} and $N_{LA} + 1$. The directions of the applied load and shear stresses are indicated. Three-dimensional periodic boundary conditions are employed in the simulations.

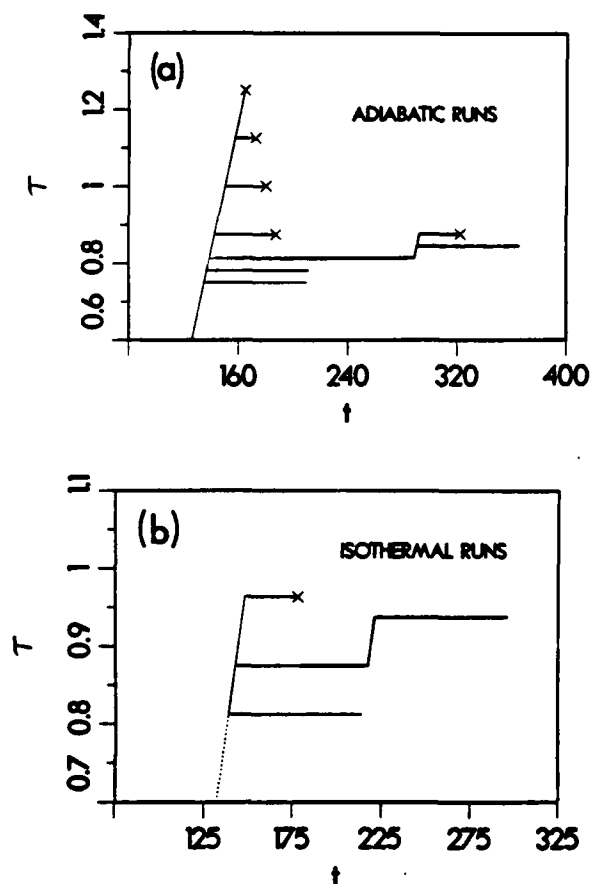


FIG. 2. Summary of the thermally adiabatic (a) and isothermal (b) (\mathcal{H}, τ, N) simulations. The applied thermodynamic tension τ_{xx} vs time (in reduced t.u.) is shown. The slanted solid line represents the rate of application of τ_{xx} (following equilibration under load). Horizontal lines correspond to simulations at constant τ_{xx} , at the values given by the intersection of the lines with the τ axis. The termination of a horizontal line by a symbol (\times) represents that at the corresponding time the system yielded in response to the applied perturbation. Lines which do not terminate by an \times correspond to τ values for which the system did not yield. From these simulations the critical values for structural transformation and eventual yield (given in Table I) were determined. Bold solid lines correspond to the system after slip and stacking-fault formation.

the horizontal solid lines in Fig. 2 (in these simulations the system is brought to the desired value of τ and then evolves under that constant value of the thermodynamic tension). In this figure the absence of a symbol (\times) at the end of a horizontal line indicates that the system did not yield for that value of τ , while a termination of the line by \times indicates yield at the corresponding time. We note that as the value of τ under which the system evolves is increased the time required for the system to yield shortens. The bold solid lines in Fig. 2 correspond to the system after slip and stacking-fault formation. From these simulations we obtain a value of $\tau_{c,xx} = 0.86 \pm 0.02$ for the critical thermodynamic tension (corresponding to $\sigma_{c,xx} = 0.95 \pm 0.03$), see Table I. Inspection of the real-space trajectories of the particles reveals that yield involves

TABLE I. Critical-yield values of the thermodynamic tension (τ_c), external stress (σ_{ex}), calculated via Eq. (13), and internal stresses (σ_c), calculated via Eq. (8c), obtained from adiabatic and isothermal simulations using the (\mathcal{H}, τ, N) ensemble. The τ_c , σ_{ex} , and σ_c values correspond to the critical values of the above quantities for structural transformations prior to yield (stacking fault or slip, as discussed in the text) in the (\mathcal{H}, τ, N) ensemble simulations. Under the constant-strain heading, results are given for the critical strain (γ_c) to bring about an inelastic structural transformation, in constrain-strain simulations, and the corresponding values of the internal stresses, (σ_c) for thermally adiabatic simulations of 18- and 27-layer systems, as well as results for isothermal constant-strain simulations of the 18-layer system. All quantities are in Lennard-Jones reduced units.

	Adiabatic (\mathcal{H}, τ, N)	Isothermal (\mathcal{H}, τ, N)
$\tau_{c,xx}$	0.8 ± 0.02	0.84 ± 0.03
$\sigma_{ex,xx}$	0.78 ± 0.01	0.83 ± 0.03
$\sigma_{c,xx}$	0.78 ± 0.01	0.84 ± 0.04
$\tau_{c,xx}$	0.86 ± 0.02	0.95 ± 0.01
$\sigma_{ex,xx}$	0.95 ± 0.03	0.99 ± 0.005
$\sigma_{c,xx}$	0.94 ± 0.02	1.00 ± 0.02
Constant strain		
	Adiabatic (18-layer)	Isothermal (18-layer)
$\gamma_{c,xx}$	0.063 ± 0.002	0.065 ± 0.003
$\sigma_{c,xx}$	0.975	1.02
γ_c/σ_c	0.065	0.064
Adiabatic (27-layer)		
$\gamma_{c,xx}$	0.076 ± 0.002	
$\sigma_{c,xx}$	1.14	
γ_c/σ_c	0.067	

interplanar motion of the (111) atomic layers (relative to one another) in accordance with observations that the main operative slip system in fcc crystals consists of (111) planes in the [110] direction.

For a certain range of values of τ the system undergoes structural transformations which do not result in total yield. This is indicated by the bold solid horizontal lines in Fig. 2 and the corresponding values are given in Table I under $\tau_{c,xx}$ (0.8 ± 0.2 for the adiabatic system and 0.84 ± 0.03 for the isothermal one). To investigate the mechanisms of response and stress relief prior to yield we have performed extensive studies of the behavior of the adiabatic system under an applied $\tau_{xx} = 0.81$. It should be noted that removing the external perturbation prior to the onset of the structural transformation results in the system returning to the average unstressed conditions, while when doing so past the structural transformation the system remains in the deformed state. Records of the average temperature (T), potential energy (E_p), kinetic energy (E_k), and elastic energy (E_{el}) [the work done on the system, see Eq. (12)] versus time (starting at $t = 140$ t.u., the intersection of the horizontal line corresponding to $\tau = 0.81$ with the solid line in Fig. 2) up to the yield point, are shown in Fig. 3. [Note that the sum of the energies in Figs. 3(b)–3(d) is constant] Inspection of the

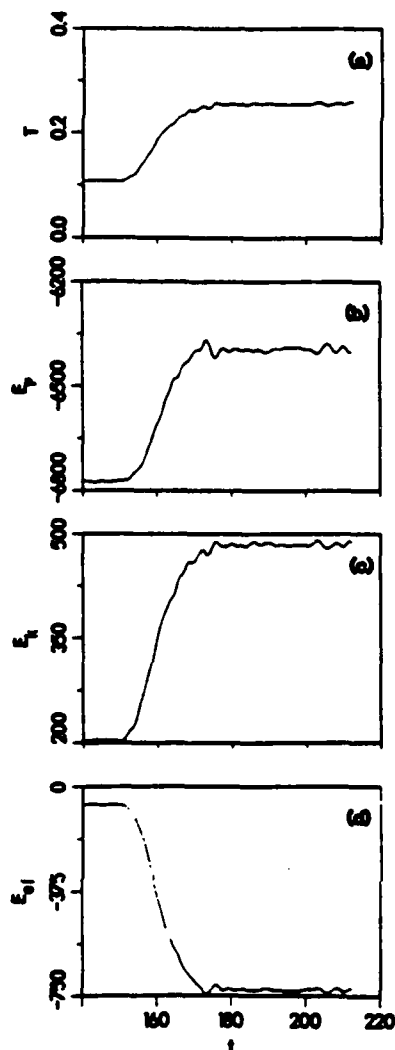


FIG. 3. Records of the temperature (T), potential energy (E_p), kinetic energy (E_k), and elastic energy (E_{el}) vs time (starting at $t=140$ t.u. obtained via an (\mathcal{H}, τ, N) simulation at $\tau_{xz}=0.81$ under thermally adiabatic conditions. The sharp changes in all quantities correspond to structural transformations. All quantities are in Lennard-Jones reduced units.

figures reveals that the average temperature of the system increases from the initial value (in reduced LJ units) of 0.11 achieving a new value of ~ 0.25 at about 175 t.u. Correspondingly, the magnitude of the system average potential energy decreases and the stored elastic energy increase in the above time interval. In addition we find that the volume of the system increases during that time period. Inspection of the structure of the system shows that during the time interval ~ 150 –175 t.u. the system undergoes structural transformations, occurring in the region occupied by the soft (solid lubricant) material (layers 10–18). The positions of atoms in a central $(11\bar{2})$ slice of the system before and after the transformation displayed in Figs. 4(a) and 4(b), respectively, show clearly the formation of stacking-fault region [i.e., change from the $abcabc \dots$ registry sequence, see Fig. 4(a)], in the soft material (open circles). In addition to the formation of the

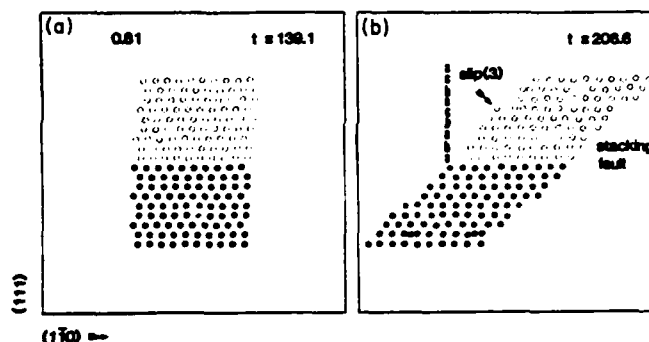


FIG. 4. Atomic trajectories for a $(11\bar{2})$ central slice of the system simulated with $\tau=0.81$: (a) at $t=139.1$ t.u. and (b) at $t=206.6$ t.u., i.e., past the structural transformation (see Fig. 3). As indicated in (b) the structural transformation consists of stacking-fault formations and slip (by three atomic rows).

stacking faults a slip region, where layers 15–18 shifted by three atomic rows to an equivalent registry, is detected. As seen the formation of the stacking fault involves layers 12 and 13. The details of this structural transformation are shown in Fig. 5 where particle positions in layers 12 (solid circles) and 13 (open circles) at three times [before (a), during (b), and after (c)], separated by $170 \Delta t$, are shown.

The mechanical response and energetic characteristics of the system can be investigated best via layer decomposition of the system properties. In Figs. 6(a) and 6(b) we depict the per-layer xz component of the internal stress for the interface layers (layer 5, 8, and 9 of the hard material and layers 10–14 of the soft material). From these figures we observe that the generation of the structural transition involves a gradual decrease in the internal σ_{xz} component in layers 11–14 of the soft material while the variation in the stress in layer 10 [the atomic plane of the soft material (B) adjacent to the hard material (A), see Fig. 1] is smaller. As seen from Fig. 6(a) the stress relief process and the associated structural transformation in the soft material are accompanied by a stress accumulation in the interfacial region of the hard material (layer 9). In addition we observe periodic oscillations in the internal stress (most pronounced for layers 11–14) past the structural transformation period, as the system relaxes in the new state after the structural transformation events. The energetics of the system is explored via the time records of the per-layer potential energies (E_p') and temperature (T') shown in Figs. 7(a) and 7(b), respectively. From the potential-energy curves we find that the potential energy of particles in layer 11 (second layer from the interface, see Fig. 1) in the soft material is initially lower than that of layers 12–14, which are further removed from the interface, since particles in that layer are within the range of the stronger interaction with the hard substrate [$\epsilon_{AB} = (\epsilon_{AA}\epsilon_{BB})^{1/2}$]. The potential energy of particles in the interfacial soft-material layer (layer 10) adjacent to the hard material is lower by about -0.4ϵ than the value for layer 11, and as seen from Fig. 6(a) the

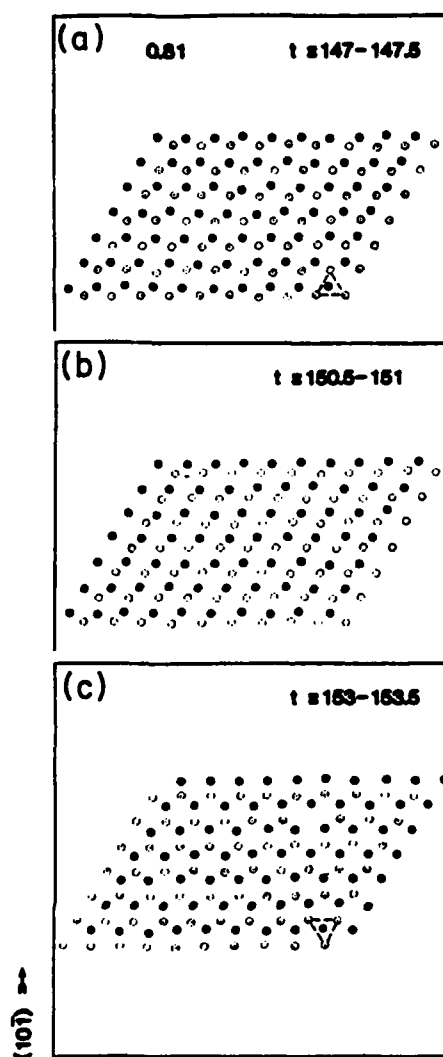


FIG. 5. Details of the system trajectories leading to the formation of a stacking fault. Atoms in layers 12 (solid circles) and 13 (open circles), in the soft material are shown before (a), mid-way through the stacking-fault formation (b), and after the layers have moved to the new registry (c). The atomic trajectories are for a simulation at $\tau_{xz}=0.81$ (as in Figs. 3 and 4).

extra stabilization "pins" this interfacial layer to the hard substrate. The potential energy of the topmost layer of the hard material [layer (9)] is lowered further by about -2.6ϵ . The potential energies of both layers 9 and 10 increase due to the structural transformation. Since the system in this set of calculations is thermally isolated, the structural change is accompanied by a temperature increase as seen from Fig. 7(b) (where the curves for successive layers, starting from 10 and up, are displaced vertically by 0.04ϵ). Note however that the final temperature after the transformation is below the melting temperature for both materials.

The variations of the external stress components for the total system [calculated from Eq. (13), for $\tau_{xz}=0.81$ and using the dynamically determined values of the matrix \mathbf{H}] are displayed in Fig. 8, versus time. We observe an increase in all components at the time of the structural

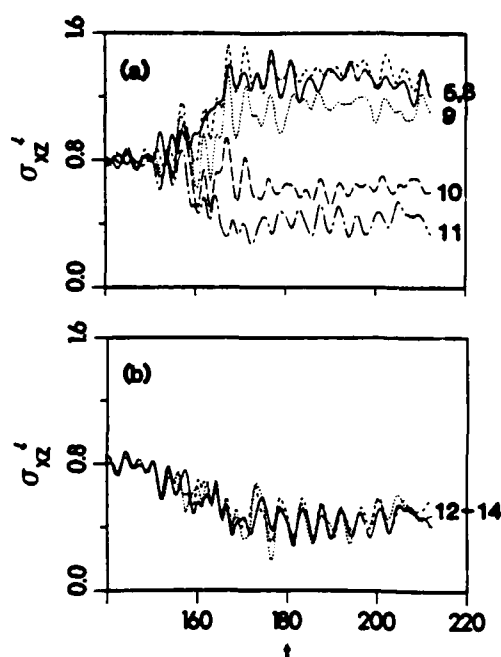


FIG. 6. Per-layer internal stresses (σ_{xz}^l) vs time (in t.u.) for a simulation at $\tau=0.81$ under adiabatic conditions. Layers 5, 8, and 9 in the hard material and 10 and 11 in the soft one are shown in (a). The stresses in layers 12-14 in the soft material are shown in (b). The interface is between layers 9 and 10. Note the variation in the internal stresses at the time of the structural transformation. The internal stresses in the interior of the soft material (10-14) decrease with layer 10 exhibiting pinning by the hard material. The stress relief in the soft material is accompanied by stress accumulation in the hard material (layers 5-9).

transformation. We also note the axial component, σ_{xx} , in the x direction (along the [111] direction, i.e., normal to the (111) planes) changes character from compressive (due to the initial load on the system) to tensile (positive value) past the structural transformation.

2. Isothermal conditions

To investigate the effect of the ambient thermal conditions we repeated the simulations described in (1) but controlled the temperature of the system, at a reduced temperature of 0.11, via periodic scaling of particle velocities. This system also exhibited structural changes (interlayer slip and stacking-fault generation, but at a higher value of $\tau_s=0.84$, as compared to the value for the adiabatic case ($\tau_s=0.80$). In addition, the volume increase after the transformation was very small. Applying higher values of τ to the system it eventually yielded at a critical value $\tau_c=0.95(\pm 0.01)$, again higher than in the adiabatic case ($\tau_c=0.86\pm 0.02$, see Table I). We conclude that the isothermal system withstands higher values of the external perturbation as compared to the adiabatic case. Since the heat generated during the transformation, which in the adiabatic case can be utilized to overcome potential barriers for structural transformations and

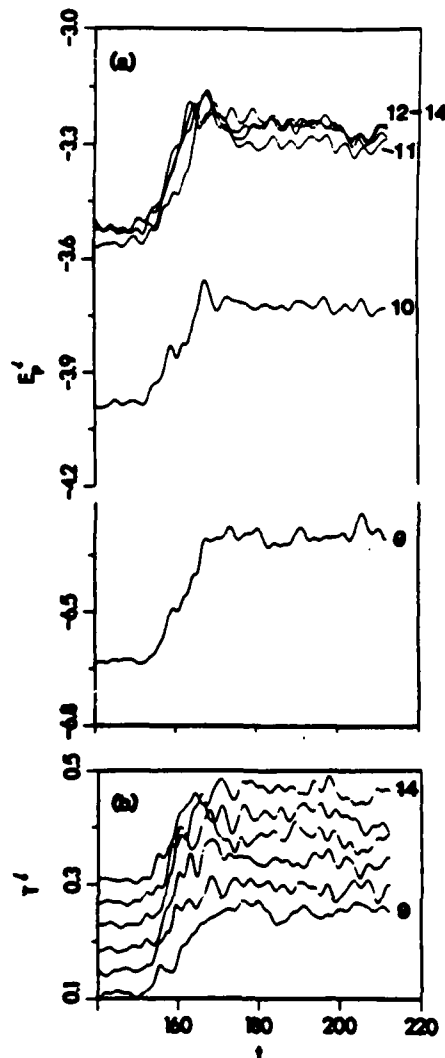


FIG. 7. Per-layer potential energies, E_p^i , in (a), and temperatures, T^i , in (b), for the system simulated at $\tau_{xz} = 0.81$ under adiabatic conditions.

yield, is dissipated to the reservoir under isothermal conditions, larger external forces are required in the latter case in order to bring about similar effects.

The behavior versus time of the xz component of the internal stress (σ_{xz}) in layers 9–14 at an applied $\tau = 0.87$, is shown in Fig. 9. It is seen that while the stresses in layers 10–14 of the soft material vary during the structural transformation they settle to values close to the initial ones. Inspection of the real-space particle trajectories for the system reveals that the system does evolve through deformed structures which contain stacking faults but it does not stabilize in these configurations. Furthermore, in the final state the intralayer registry is intact, which is consistent with the behavior of the internal stresses shown in Fig. 9.

3. The effect of atomic-size mismatch

In the simulations discussed above the materials on both sides of the interface differed by the potential well-depth parameter ϵ ($\epsilon_{BB} = 0.5\epsilon_{AA}$), but were character-

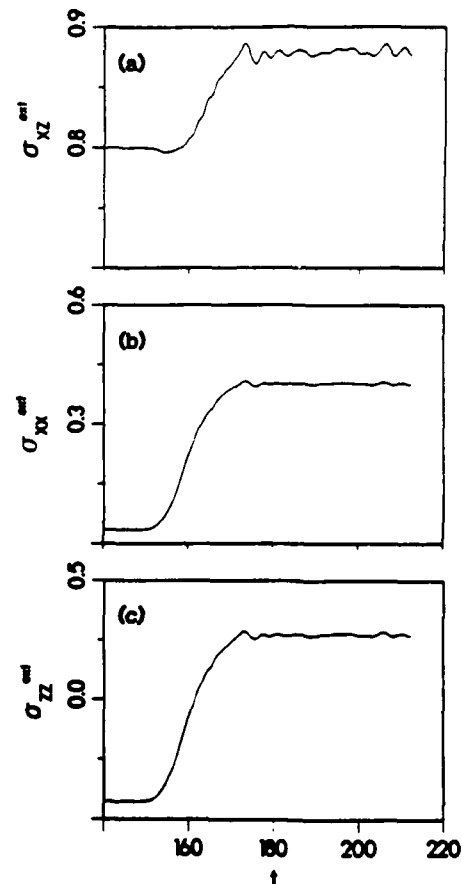


FIG. 8. The external stress components [calculated from Eq. (13)] for simulations at $\tau_{xz} = 0.81$ under adiabatic conditions vs time (in t.u.). Increases are observed in all components at the time of structural transformation. Note the change from compressive (due to the initial load) to tensile character in the axial component σ_{xz}^{ext} .

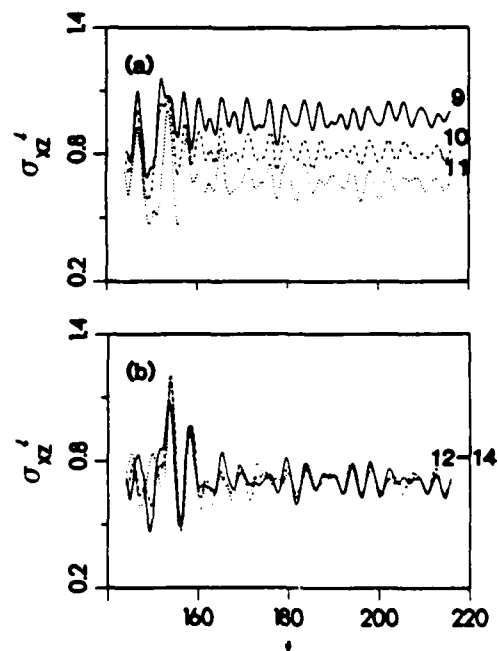


FIG. 9. Per-layer internal stresses (σ_{xz}^i) vs time (in t.u.) for a simulation under isothermal conditions at $\tau_{xz} = 0.87$. (a) Layers 9–11; (b) layers 12–14.

ized by the same value of the "atomic-size" parameter, $\sigma_{AA} = \sigma_{BB} = \sigma_{AB}$ [see Eq. (30)]. To investigate the dependence of the system properties on the mismatch in atomic sizes between the two interfacing materials we have performed simulations in which the well-depth parameters were chosen as before (see Sec. III A) but the σ parameters were chosen such that the atoms in the soft (*B*) material are characterized as having a larger size, i.e., $\sigma_{BB} = 1.5\sigma_{AA}$ and $\sigma_{AB} = 1.25\sigma_{AA}$. In these simulations the hard material (*A*) occupied six layers (numbered 1–6) and the soft material occupied nine layers (numbered 7–15), with 162 atoms per layer in the *A* material and 72 atoms per layer in the *B* (soft) material (the total number of particles was 1620).

A series of studies, similar to those described above, employing the (\mathcal{H}, τ, N) ensemble under thermally adiabatic conditions were performed. From these simulations we have determined that the critical-yield value of the thermodynamic tension in this system is $\tau_{c,xz} = 0.62 \pm 0.01$ (and the corresponding external stress $\sigma_{c,xz} = 0.51 \pm 0.01$), which are considerably lower than the corresponding values found for the equal-atomic size systems (see Table I). Moreover, unlike the previous cases, where yield was preceded by an external stress regime in which the system responded inelastically via a sequence of structural transformations, for the present system (in which the atomic sizes across the interface differ) no such behavior is observed. Time histories of the layer decomposed potential energy, E_p^l and internal stress, σ_{xz}^l , obtained in a simulation at a constant thermodynamic tension $\tau_{xz} = 0.52$ are shown in Figs. 10 and 11. First we observe that at yield the potential energy and internal stress

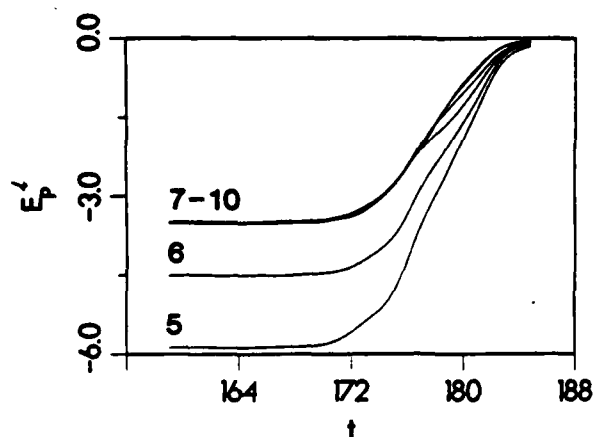


FIG. 10. Per-layer potential energies for a system containing an interface (between layers 6 and 7) between a hard (layers 1–6) and soft (layers 7–15) materials which are characterized in addition by different atomic-size parameters ($\sigma_{BB} = 1.5\sigma_{AA}$). Results are for simulations employing the (\mathcal{H}, τ, N) ensemble, under adiabatic conditions at $\tau_{xz} = 0.52$. Time is in units of t.u. and potential energy in reduced Lennard-Jones units. Note that the whole soft material responds in unison (layers 7–10). The increase in potential energy starting at ~ 172 t.u. corresponds to yield. No distinct structural transformations prior to yield (in contrast to the corresponding equal-atomic-size case discussed previously) were detected.

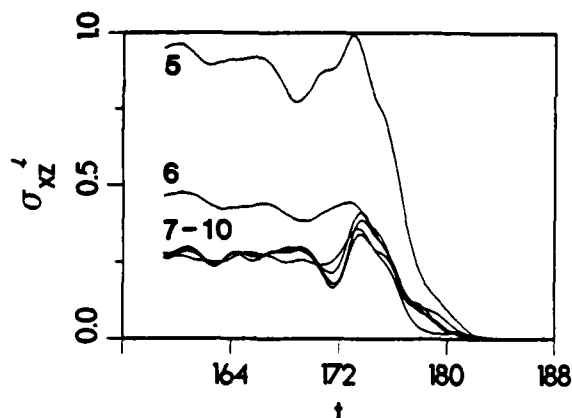


FIG. 11. Per-layer internal stresses in the system described in Fig. 10. Note the stress relief, resulting in yield indicated by the vanishing of the internal stresses.

vanish (stress relief). Secondly we note that the soft system (layer numbers larger than 6) does not exhibit "pinning" by the underlying hard substrate, although the strength of interaction between the two is the same as in the previous studies where such pinning was observed at the interface (see above). Thirdly the whole soft system responds in unison, starting at the interfacial layer and up into the material. These observations can be understood when considering that as a consequence of the larger atomic size the atoms of the soft material at the interface average over the corrugation of the potential due to the substrate, resulting in an effective potential surface which exhibits smaller variations for lateral displacements parallel to the interface plane, and consequently a reduced resistance to shear.

C. Applied strain simulations

We turn next to another mode of simulation in which instead of applying a thermodynamic tension, τ , the system is strained while maintaining a constant volume. The preparation of the system up to the application of external forces is the same as described in Secs. III A and III B. The starting point for these simulations is an equilibrium averaged system of 18 layers consisting of nine layers each of hard and soft materials (see Sec. III A), at a reduced temperature $T = 0.11$ under a load of 0.5. (The equilibrium averaged calculational cell is nearly orthogonal with a parallelepiped base with $H_{xx} = 11.04\sigma$, $H_{yy} = 6.69\sigma$, $H_{zz} = 16.25\sigma$, $H_{yz} = 3.86\sigma$, and all other components fluctuating about zero.) At this stage we apply a constant-strain rate $\dot{\gamma}$ in the $(11\bar{2})$ plane along the $[1\bar{1}0]$ direction (see Fig. 1), i.e.,

$$\dot{H}_{xz} = \dot{\gamma} H_{zz}$$

$$\dot{H}_{\alpha\beta} = 0 \quad (\text{for } \alpha\beta \text{ for which } \alpha \neq x \text{ and } \beta \neq z)$$

with the strain rate $\dot{\gamma} = 4 \times 10^{-3}$ t.u.⁻¹ (i.e., at this strain rate the value of H_{xz} grows from zero to about 30% of H_{zz} in 10^4 integration time steps).

As in the previous simulations (see Sec. III B) we have performed studies under both thermally adiabatic and isothermal conditions. Since the results are similar in both cases we focus on the former ones. Variations of the system temperature, T , and particle potential energy, E_p , versus the strain γ are shown in Fig. 12. As seen these quantities exhibit a characteristic nonmonotonous behavior with an increasing trend. The temperature of the system grows in a stepwise manner and the potential energy in a sawtooth fashion characterized by periods of increase in E_p followed by sharp drops occurring at the same strain values for which the step increases in T occur. To assess possible system size dependencies of the results we display in Fig. 13 similar results for a system in which the number of hard material layers (1–9) is as above but the number of layers of the soft material ($\epsilon_{BB} = \epsilon_{AA}/2$) is doubled (layers 10–27). This system was equilibrated as before and was simulated at a constant-strain rate of 2.8×10^{-3} t.u. $^{-1}$ (which is equivalent to that used for the smaller system). As evident the overall characteristics of the system temperature and potential energy are similar in both cases, particularly for strains up to and including the first nonmonotonic feature ($\gamma = 0$ to ~ 0.15). Comparison of the systems' response at higher strains indicates that the presence of a larger region of soft material makes the system more pliant. However as we discuss below the overall picture and certain quantitative conclusions are the same for the two system sizes.

To gain further detail about the process underlying the

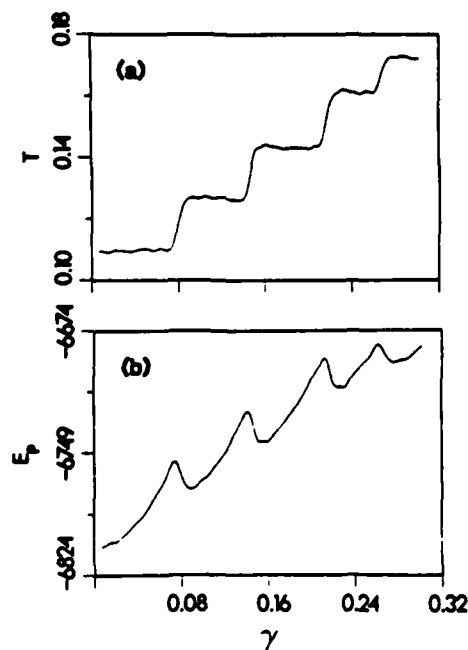


FIG. 12. Temperature (T) and potential energy (E_p) vs strain (γ) for a system composed of 9 layers of hard material and 9 layers of soft material ($\epsilon_{BB} = \epsilon_{AA}/2$), simulated under constant-strain rate ($\dot{\gamma} = 4 \times 10^{-3}$ t.u. $^{-1}$) and thermally adiabatic conditions. The steps in the curves are associated with structural transformations. All quantities are given in reduced Lennard-Jones units.

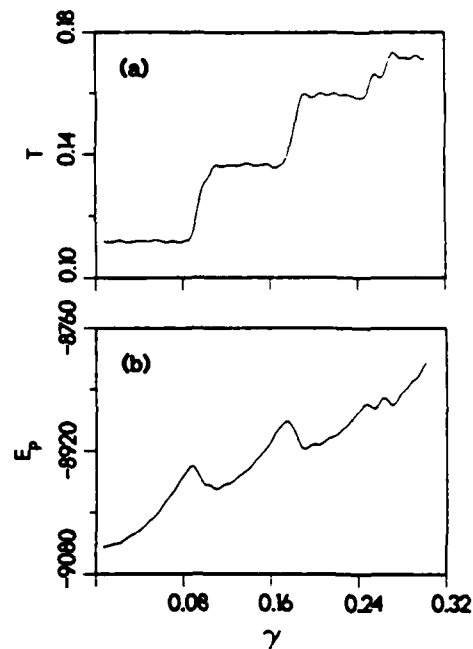


FIG. 13. Same as Fig. 12, but for a larger system size; nine layers of hard material (layers 1–9) and 18 layers of soft material (layers 10–27).

behavior exhibited in Figs. 12 and 13, we display in Figs. 14 and 15 temperature profiles, T' , decomposed into layers (and offset between layers by 0.03ϵ on the temperature axis) versus strain (γ) for the 18- and 27-layer systems, respectively. As seen the layer temperatures fluctuate in

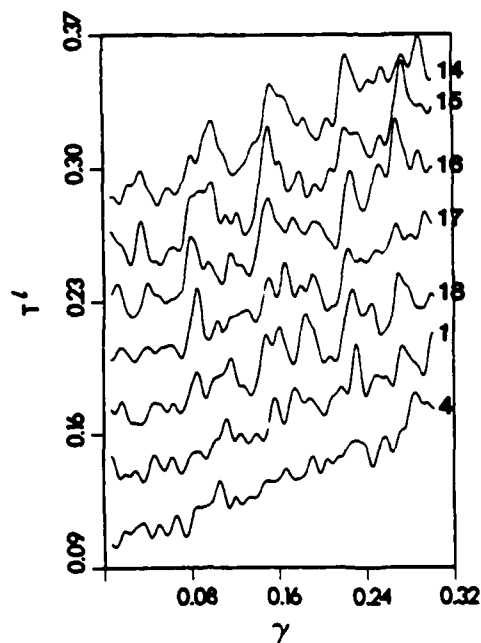


FIG. 14. Per-layer temperatures, T' , corresponding to the system described in Fig. 12. Note the general heating trend (thermally adiabatic simulations) and the stages of sharp temperature increases, occurring for strain $\gamma \gtrsim 0.08$, in layers 14–18, in the soft material, corresponding to structural transformations.

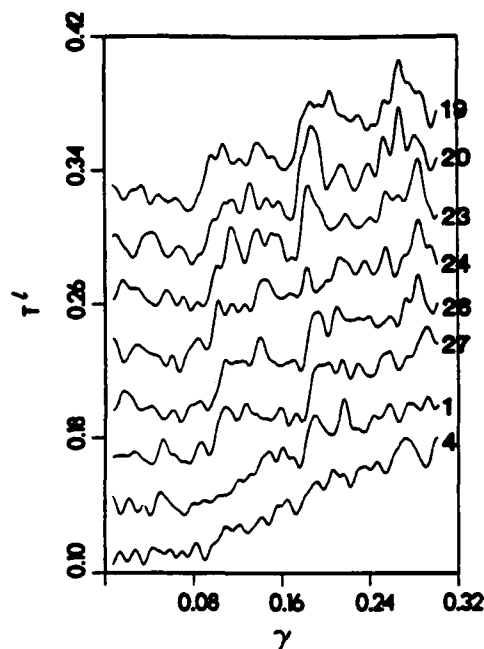


FIG. 15. Same as Fig. 14, for the larger system size (nine layers of hard and 18 layers of soft materials). Note sharp temperature increases in layers 19–27.

response to the applied strain with an overall heating trend. We remind the reader that in the 18-layer system the interface between the hard and soft material is between layers 9 and 10 (and due to the periodic boundary conditions also between 1 and 18), and in the 27-layer system it is located between layers 9 and 10 (and also between layers 1 and 27). A more detailed inspection of Figs. 14 and 15 reveals sharp temperature spikes in regions inside the soft materials (layers 14–18 in Fig. 14 and layers 19–27 in Fig. 15) occurring at characteristic values of the strain which compare with the values of γ at which the nonmonotonic behavior is seen in Figs. 12 and 13. These observations indicate that in response to the applied strain the system deforms by going over potential barriers between structural configurations. In fact examination of the real-space particle trajectories shows that at these characteristic strains interlayer slip is initiated between layers 15 and 16 for the 18-layer system and layers 23 and 24 for the larger one (both inside the soft material in regions removed from the material interface by about 3–5 atomic layers).

To gain further insight about the process of deformation we show in Figs. 16 and 17 layer profiles for the per-layer internal stresses versus strain in the 18- and 27-layer systems, respectively. It is seen that the stress component parallel to the strain direction, σ_{xx} , exhibits a sawtooth shape (much like the potential energies shown in Figs. 12 and 13) with the first peak occurring at $H_{xx} \sim 0.08H_{zz}$ (i.e., at a strain $\gamma = 0.08$). The rises in the stress correspond to stress accumulation and the subsequent drops to stress relief (as corroborated by inspection of real-space particle trajectories which reveal that the stress relief mechanism involves interlayer slip). The os-

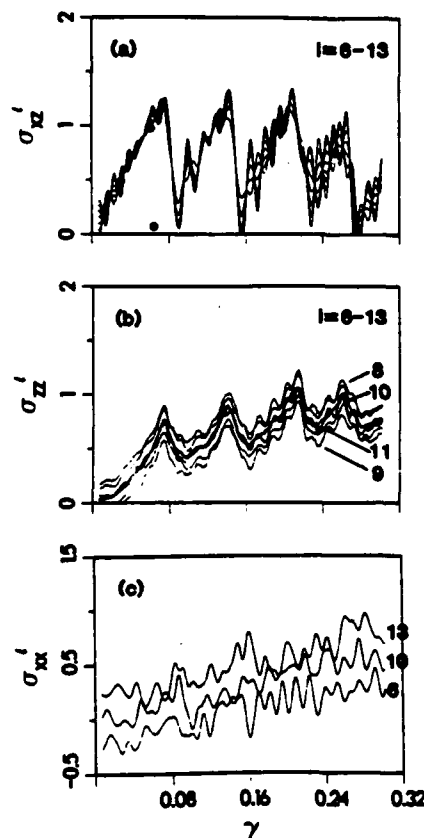


FIG. 16. Per-layer internal stress vs strain (γ) profiles for the σ'_{xx} [in (a)], σ'_{zz} [in (b)], and σ'_{zz} [in (c)], components for the system composed of nine layers of hard and nine layers of soft material, and simulated under adiabatic conditions. Note the monotonic increases in internal stress in σ'_{xx} and the axial component σ'_{zz} followed by sharp drops corresponding to structural transformations. The solid dots in (a) give the values of the internal stress component σ'_{xx} obtained via constant strain simulations at the corresponding values of γ . As seen, for values of $\gamma < 0.063$ (first two dots) the values of σ'_{xx} thus obtained coincide with those corresponding to the constant strain rate simulations. For $\gamma = 0.063 \pm 0.002$ the internal stress drops sharply, corresponding to a structural stress relieving transformation in the system. The constant-strain simulations were used to determine the critical stresses given in Table I. All quantities are in reduced Lennard-Jones units.

cillatory behavior seen in Figs. 16(a) and 17(a) after the slip is due to damped planar oscillations in the new structural configuration. The same general behavior is seen for the axial stress component, σ_{zz} (i.e., the stress component along the [111] direction [see Figs. 16(b) and 17(b)]). Note that for σ_{zz} the curves are bunched in groups with the interfacial layers (8,10, and 9,11) bounding the closely-packed stress curves corresponding to the middle region in the hard and soft materials (layers 6,7 and 12,13 for both system sizes). Finally, the axial stress component σ_{xx} , in the direction [110] of the applied strain, shown in Figs. 16(c) and 17(c), exhibits merely fluctuations with a rising trend [also seen for σ_{zz} , see Figs. 16(b) and 17(b)] which is a direct consequence of the

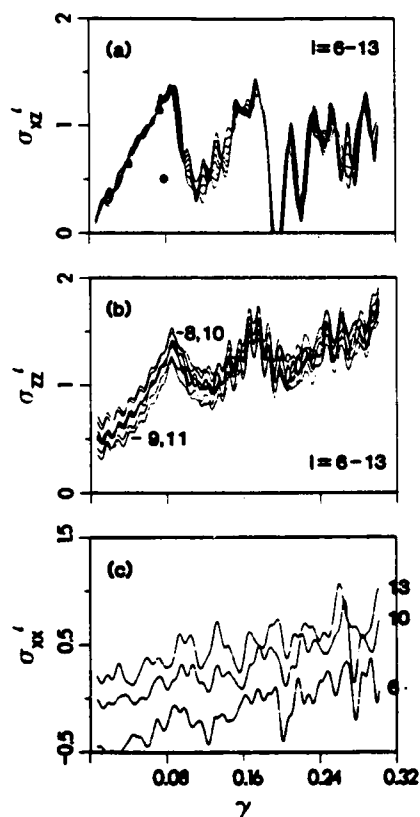


FIG. 17. Same as Fig. 16, but for the larger system, composed of nine layers of hard material and 18 layers (10–28) of soft material.

heating of the system. Note in addition the transition from compressive (due to the initial load) to tensile behavior as the strain increases. The difference between the character of variations in σ_{xx} (similarly σ_{yy}) and that of σ_{xz} and σ_{yz} is consistent with our observation that the stress relief mechanism is via processes in which (111) planes slip past one another with no significant intralayer distortions.

As already mentioned in Sec. III B the rate of application of the perturbation [applied shear stress (or thermodynamic tension) as discussed in Sec. III B and applied strain in this section] in MD simulations is faster than laboratory rates. In addition these rates are also too fast to allow an adiabatic (in the sense of dynamical relaxation on the atomic scale) response of the system. With regard to the first issue we refer to the studies of Moran, Ladd, and Hoover²⁸ who suggested on the basis of comparison between NEMD simulations and experiments that large-deformation and plastic-flow phenomena in close-packed metals obey a scaling relation which allows comparison between MD calculations and experimental data although the two differ by orders of magnitude in the rates of the applied shear. Moreover these authors suggest that these observations imply that plastic response and flow of these metals can be described by a single physical mechanism over a range of strain rates from 10 kHz to 1 THz (our values of $\dot{\gamma}$ using well depth, ϵ , and σ parameter values in the 6–12 LJ potential to ap-

proximate typical metals, are of the order of 10 GHz).

To address the second issue and determine accurately temporally adiabatic values for the critical strains (i.e., those at which inelastic structural deformations occur) in our system, we have performed for both system sizes simulations at constant strains approaching the value at which slip occurred [see first peak in Figs. 16(a) and 17(a) at $\gamma \sim 0.08$]. Thus in these series of simulations the system was allowed to fully relax under prescribed strains. The values for the internal stresses, σ_{xz} , obtained from these simulations are represented by solid dots in Figs. 16(a) and 17(a). First we note that for strains below the critical strain value the developed internal stresses in these simulations are the same as those obtained in the constant-strain-rate studies, which indicates that for this regime of strain values the system responds adiabatically even when the strain is applied at a rather high rate. Secondly, the values of the critical strain, γ_c , obtained in these simulations (see Table I, $\gamma_{s,xz} = H_{xz}/H_{zz} = 0.063 \pm 0.002$ for the 18-layer system and 0.076 ± 0.002 for the 27-layer system) are below that given by the constant-strain-rate simulations. Thirdly, the corresponding values of the internal stresses $\sigma_{s,xz}$ (0.975 and 1.14 for the small and large system, respectively, see Table I) are larger than the one obtained using the adiabatic (\mathcal{H}, τ, N) simulations (Sec. III B), and the one for the 27-layer system is somewhat higher than that of the smaller system. Note however, that the critical strain-to-stress ratio, γ_c/σ_c , is nearly the same for both systems (0.0634 and 0.0652, for the small and large systems, respectively). We conclude therefore that while the larger system exhibits a somewhat larger tolerance to strain (i.e., is more pliant) the elastic properties of our systems are independent of thickness at or above nine layers of soft material. Finally, we note that for strain values above γ_c , the systems exhibit slip accompanied by sharp drops in the value of the internal stress σ_{xz} (and similarly for σ_{yz}) indicating stress relief. We note that removing the strain for strain values below the critical value γ_c , results in a return of the system to the unstrained configuration, indicating that in this strain regime the system deforms elastically, while after removing the strain past the structural transformation (i.e., for values larger than γ_c) the system remains in the new structural configurations.

IV. SUMMARY

In this investigation we have studied the formulations of molecular-dynamics techniques for simulations of material systems evolving under applied finite external perturbations. Methodologies of simulations of phenomena involving finite deformations (plastic deformations, structural transformations, yield, and flow) have been discussed (Sec. II) and demonstrated (Sec. III). These simulations yield valuable information about the atomic scale mechanisms of materials' dynamical response to mechanical perturbations.

In these studies we focused on interfacial systems, composed of interfacing crystalline solids characterized by differing interatomic interaction strengths and in some

cases also by differing atomic sizes. Our main results may be summarized as follows.

(i) For interfacial systems which are characterized by differing interatomic interaction strengths (i.e., the interface is between a hard and soft material), the system responds to an applied nonisotropic perturbation (applied shear or strain) first elastically and then via stress relief mechanisms which involve structural transformations (stacking-fault formation and interlayer slip). For larger values of the external forces, eventual yield occurs.

(ii) Critical values of the external perturbation required in order to bring about inelastic response (structural transformations and yield) have been determined (see Table I). Our simulations demonstrate that these critical values are smaller for a system under thermally adiabatic conditions than for an isothermal environment. The origin of the difference lies in the dissipation of the generated thermal energy under isothermal conditions, which necessitates larger values of the external perturbations in order to overcome potential barriers for structural modifications and eventual yield.

(iii) The cohesive interatomic interactions at the interface between a hard substrate and a soft material result in "pinning" of the soft material at the interface (1–3 atomic layers). As a result the response of the system to the external perturbation (stress relief via plastic as well as structural transformations) occurs in a "shear band" consisting of a few atomic layers inside the soft material, which are located at about 1–3 layers away from the original (unstressed) interface. The stress relief in the soft material is accompanied by stress accumulation in the

hard substrate.

(iv) MD simulations for interfacing hard and soft materials, which in addition are characterized by differing atomic sizes, reveal the important role played by atomic-size mismatch in determining the atomic-scale mechanism of response. For such system it was found that no adhesive pinning occurs at the interface, and that the soft (and larger atomic size) material responds as a whole with no distinct structural transformations preceding the yield point. The critical-yield stress value for this system is significantly lower than that found for the corresponding equal-atomic-size system.

(v) Comparison of our results in this study for the [111] interface with our previous investigations of the [100] interface¹⁷ demonstrates the dependence of the critical values of the shear stresses on the crystallographical orientation of the interface, as well as of certain details of the stress relief mechanisms.

ACKNOWLEDGMENTS

This work is supported by the Hughes Aircraft Company, under the Defense Advanced Research Projects Agency (DARPA)–Hughes Tribological Fundamentals Program, DARPA Order No. 5177, U.S. Air Force Wright Aeronautical Laboratory (AFWAL) Contract No. F33615-C-5087 and by the U.S. Department of Energy (DOE) under Grant No. DE-FG05-86ER-45234. Most of the calculations were performed at the Pittsburgh Supercomputer Center.

¹L. Davison, *Mater. Res. Soc. Bull.* **8**, 14 (1988); see also *Approaches to Modeling of Friction and Wear*, edited by F. F. Ling and C. H. T. Pass (Springer, Berlin, 1988).

²U. Landman, in *Computer Simulation Studies in Condensed Matter Physics: Recent Developments*, edited by D. P. Landau and H. B. Schutter (Springer, Berlin, Heidelberg, 1988); see also other articles in this volume.

³U. Landman *et al.*, *Mater. Res. Soc. Sym. Proc.* **63**, 273 (1985); see also other articles in this volume.

⁴F. F. Abraham, *Adv. Phys.* **35**, 1 (1986); *J. Vac. Sci. Technol. B* **2**, 534 (1984).

⁵*Mater. Res. Soc. Bull.* **XIII** (2), 14–39, February 1988.

⁶U. Landman, R. N. Barnett, C. L. Cleveland, J. Luo, D. Scharf, and J. Jortner, in *Proceedings of the Symposia of the Topical Group on Few-Body Systems and Multiparticle Dynamics*, AIP Conf. Proc. No. 162, edited by D. A. Micha (AIP, New York, 1987), p. 200.

⁷D. W. Heerman, *Computer Simulation Methods* (Springer, Berlin, 1986).

⁸*Computer Simulations of Solids*, edited by C. R. A. Catlow and W. C. Machord (Springer, Berlin, 1982).

⁹W. G. Hoover, *Molecular Dynamics*, Vol. 258 of *Lecture Notes in Physics* (Springer, Berlin, 1986).

¹⁰H. C. Andersen, *J. Chem. Phys.* **72**, 2384 (1980).

¹¹M. Parrinello and A. Rahman, *J. Appl. Phys.* **52**, 7182 (1981).

¹²J. R. Ray and A. Rahman, *J. Chem. Phys.* **80**, 4423 (1984).

¹³For an extension to metallic systems see R. N. Barnett, C. L.

Cleveland, and U. Landman, *Phys. Rev. Lett.* **54**, 1679 (1985); **55**, 2035 (1985).

¹⁴W. G. Hoover, *Phys. Rev. A* **118**, 111 (1983).

¹⁵See reviews by S. Yip and M. Parrinello, in *Molecular-Dynamics Simulations of Statistical-Mechanical Systems*, Proceedings of the International School of Physics, "Enrico Fermi," Course XCVII, Varenna, 1985, edited by C. Ciccotti and W. G. Hoover (Societe Italiana di Fisica, Bologna, 1986).

¹⁶See recent reviews by D. J. Evans and G. P. Morriss, *Comput. Phys. Rep.* **1**, 297 (1984); D. J. Evans and W. G. Hoover, *Ann. Rev. Fluid Mech.* **18**, 243 (1986).

¹⁷M. W. Ribarsky and U. Landman, in *Approaches to Modeling of Friction and Wear*, edited by F. F. Ling and C. H. T. Pan (Springer-Verlag, New York, 1988), p. 159.

¹⁸S. Sutton, M. W. Ribarsky, and U. Landman, *J. Chem. Phys.* (to be published).

¹⁹C. L. Cleveland, *J. Chem. Phys.* (to be published).

²⁰G. J. Dienes and A. Paskin, in *Atomistic of Fracture*, edited by R. M. Latanision and J. R. Pickens (Plenum, New York, 1983), p. 671; A. Paskin, K. Sieradzki, D. K. Som, and G. J. Dienes, *Acta Metall.* **31**, 1253 (1983).

²¹B. DeCelis, A. S. Argon, and S. Yip, *J. Appl. Phys.* **54**, 4864 (1983), and references therein.

²²W. T. Ashurst and W. G. Hoover, *Phys. Rev. B* **14**, 1465 (1976).

²³W. G. Hoover, N. E. Hoover, and W. C. Moss, *J. Appl. Phys.* **50**, 829 (1979); see also A. J. C. Ladd and W. G. Hoover,

- Phys. Rev. B 26, 5469 (1982).
- ²⁴P. C. Gehlan, G. T. Hahn, and M. F. Kanninen, *Scr. Metall.* 6, 1087 (1972).
- ²⁵See review by M. I. Baskas and M. S. Daw in *Computer Simulations in Materials Science*, edited by R. J. Arsenault, J. Beeler, and D. M. Esterling (American Society for Metals, Cleveland, 1988).
- ²⁶R. Najafabadi and S. Yip, *Scr. Metall.* 17, 1199 (1983).
- ²⁷J. R. Ray and A. Rahman, *J. Chem. Phys.* 82, 4243 (1985).
- ²⁸B. Moran, A. J. C. Ladd, and W. G. Hoover, *Phys. Rev. B* 28, 1756 (1983).
- ²⁹B. L. Holian, *Phys. Rev. A* 37, 2562 (1988).
- ³⁰M. D. Kluge, J. R. Ray, and A. Rahman, *J. Chem. Phys.* 85, 4028 (1986); M. D. Kluge and J. R. Ray, *Phys. Rev. B* 37, 4132 (1988).
- ³¹F. D. Murnaghan, *Finite Deformations of an Elastic Solid* (Wiley, New York, 1951).
- ³²R. N. Thurston, in *Physical Acoustics*, edited by W. P. Mason (Academic, New York, 1964), Vol. 1, Pt. A.
- ³³H. Goldstein, *Classical Mechanics* (Addison-Wesley, Reading, Mass., 1950).
- ³⁴This interface orientation was chosen in view of our previous studies of the [001] interface (see Ref. 17), where it was found that slip occurs for the Lennard-Jones fcc system along the (111) planes. Note that the values for external stress given in Ref. 17, should be interpreted as those for the thermodynamic tension (see Sec. II).
- ³⁵If the interaction parameters are chosen such that they correspond to the cohesive energy and lattice constant of nickel ($\epsilon = 3.54 \times 10^{-13}$ erg, $\sigma = 2.49$ Å, and atomic mass $m = 9.75 \times 10^{-23}$ g) a reduced temperature $T = 0.11$ corresponds to 300 K, the reduced melting temperature $T_m = 0.7$ corresponds to 2000 K, the reduced unit of stress or load to 2.4×10^7 g/cm² (or 2.4×10^{10} dyn/cm²), and the reduced time unit (t.u.) corresponds to 4.1×10^{-13} sec.

Structural and dynamical consequences of interactions in interfacial systems

Uzi Landman, W. D. Luedtke, and M. W. Ribarsky
School of Physics, Georgia Institute of Technology, Atlanta, Georgia 30332

(Received 31 March 1989; accepted 3 April 1989)

Basic understanding of the structure and dynamics of materials and their response to external perturbations requires knowledge on the microscopic level, of the underlying energetics and atomic dynamics, whose consequences we observe and measure. Coupled with the above is the everlasting quest to observe and understand natural phenomena on refined microscopic scales, which provides the impetus for the development of experimental and theoretical techniques for the interrogation of materials with refined spatial and temporal resolution. In this paper we review molecular dynamics simulations for studies of the energetics and dynamical response of materials to external mechanical perturbations. Applications to investigations of solid and liquid interfacial systems under stress and to studies of the consequences of tip-substrate interactions in atomic force microscopy are demonstrated.

I. INTRODUCTION

Basic understanding of the structure and dynamics of materials and their properties often requires knowledge on a microscopic level of the underlying energetics and interaction mechanisms whose consequences we observe and measure. The everlasting quest to observe and understand nature on microscopic scales¹ is a dominant trend in science, leading to the development of conceptual, technological, and experimental devices which allow interrogation of nature with refined spatial and temporal resolution. Elucidation of the structure, dynamics, mechanical properties, and response of material systems to external perturbations on the atomic level, are key issues in developing a fundamental understanding of varied systems and phenomena of coupled basic and technological interest, such as surface and interface systems, surface reactions and catalysis, electrochemical interfaces, understanding of structure-function relationships in biomolecular systems, microelectronics materials, tribology, lubrication, wear, material fatigue and yield, crack propagation, stress induced phase and structural transformations, and hydrodynamical phenomena in confined fluid systems, to name just a few. Although most of the above listed phenomena represent everyday experiences and have been observed and studied for a long time, detailed microscopic theories of them (with few exceptions) are lacking. Nevertheless large bodies of empirical data and in some cases phenomenological model descriptions have been developed.

On the experimental front the developments of the surface force apparatus (SFA)^{2,3} scanning tunneling microscopy (STM)⁴ and of the related atomic force microscopy (AFM)⁵ broaden our perspectives and abilities to probe the morphological and electronic structure and the nature of interatomic forces in materials, open new avenues⁶ for microscopic investigations and manipulations of technological systems and phenomena such as tribology,^{3,7} lithography and in biochemical applications,⁶ and present exciting possibilities for the development of miniaturized electronic, magnetic and optical devices.

In the latter two techniques a sharp tip is brought close to the surface and either the tunneling current (STM) or deflection of a flexible cantilever holding the tip (AFM) are monitored, either by tunneling or by optical interferometry as the surface is scanned. Since the proximity of the tip to the surface may induce structural modifications in both the substrate and the tip, the nature of the tip-substrate interactions and their consequences are key issues in the development of these spectroscopies (as is the issue of probe-system interaction in all methods of microscopic resolution). Of particular interest are questions related to the dynamical response of the substrate (and tip) which may result in temporary or permanent modifications of the local properties, and those related to the effect of system conditions (such as temperature) which may influence the response as well as affect the spatial resolution. It has been indeed suggested⁸ that STM images can be dominated by elastic deformations induced by the tip-substrate interatomic forces and a transition from a tunnel regime to point contact has been observed.⁹

Recently, the AFM has been applied to study the topography and frictional forces at the atomic scale.⁷ Furthermore, recent investigations³ of the dynamical properties of molecularly thin liquid films confined between two surfaces, using an extension of the SFA, have demonstrated the direct consequences of microscopic molecular structure and interactions on the structural and dynamical properties of such systems both under static and steady-state shear-flow conditions.

On the theoretical front computer molecular dynamics (MD) simulations¹⁰⁻¹⁹, which are in a sense computer experiments where the evolution of a physical system is simulated, with refined temporal and spatial resolution, via a direct numerical solution of the model equations of motion, open new avenues in investigations of the microscopic origins of material phenomena. These methods alleviate certain of the major difficulties which hamper other theoretical approaches, particularly for complex systems such as those characterized by a large number of degrees of freedom, lack of symmetry, nonlinearities and complicated interactions. In

addition to comparisons with experimental data which provide guidance in the interpretation of data and the impetus for new measurements, computer simulations can be used as a source of physical information which may not be accessible to laboratory experiments, and in some instances the computer experiment itself serves as a testing ground for theoretical concepts.

In this paper we review recent molecular dynamics studies of systems and phenomena related to the rapidly evolving field of nanoscience. We address and demonstrate investigations of three issues: (i) the consequences of dynamical tip-substrate interactions, (ii) the nature of bounded thin fluid films in equilibrium and in steady-state flow under shear, and (iii) the microscopic energetics, dynamics and response of interfacial systems to external perturbations.

II. CONSEQUENCES OF TIP-SUBSTRATE INTERACTIONS

To investigate the consequences of the dynamical interactions between the tip and the substrate in AFM we have performed MD simulations, employing the Stillinger-Weber (SW) potentials for silicon²⁰ which include two- and three-body interactions and which have been used recently in a number of investigations of bulk, surface and interface properties of this material.¹⁷⁻²⁴ Since both the substrate and tip consist of the same material, these simulations correspond to the case of a reactive tip-substrate system. Our simulations,^{17-19,23} in both the constant-tip-height and constant-force scan modes, reveal that the *local* structure of the surface can be stressed and modified as a consequence of the tip-substrate dynamical interaction, even at tip-substrate separations which correspond to weak interaction. For large separations these perturbations anneal upon advancement of the tip while permanent damage can occur for smaller separations. For the material that we simulated (Si), we do not find long-range elastic deformations, which may occur in other circumstances⁸ depending upon the elastic properties of the material and the nature of interactions. Furthermore, we find that the characteristics of the data depend upon the geometry of the scan, the degree of perfection of the substrate and the temperature. We identify various dynamical events including stick-slip phenomena, which could be experimentally resolved, using current estimates,^{5,6} and which would influence the analysis of data, as well as pointing to ways in which the tip could be used for atomic scale manipulations of the material.

In our simulations the system consists of N_L layers of dynamic Si particles with n_L atoms per layer, exposing the (111) surface, and interacting with two layers of a static Si substrate of the same structure. In simulations involving a small tip $N_L = 4$ and $n_L = 49$, while in simulations involving larger tips $N_L = 6$ and $n_L = 100$. The two-dimensional calculational cell, defined by the $(1\bar{1}0)$ and $(10\bar{1})$ vectors, is periodically repeated parallel to the (111) plane. Two types of tips were employed in our simulations. First, we have used a sharp tip simulated by four Si atoms in an initial tetrahedral configuration, "mounted" on and interacting with two layers of silicon atoms which serve as a holder. In addition we have employed larger tips consisting of 102 atoms, which

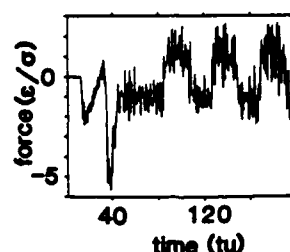


FIG. 1. Total F_z force (in units of 1.6572×10^{-9} N) on the small rigid silicon tip as it is lowered to a distance of 1.227 Å, equilibrated and scans along the surface. Time is in units of $tu = 7.6634 \times 10^{-14}$ s. Note the sharp variation in the force as the tip is lowered and the periodic oscillations reflecting the atomic structure of the surface during the scan ($t \geq 60$).

were either ordered [exposing a 16 atoms (111) planar facet] or disordered. The equations of motion, governed by the SW potential,²⁰ are integrated using a fifth-order predictor-corrector algorithm with a time step $\Delta t = 1.15 \times 10^{-3}$ ps, [or 0.015 time units (tu) where $tu = 7.6634 \times 10^{-14}$ s]. Throughout we use $\epsilon = 50$ kcal/mol as the unit of energy, $\sigma = 2.0951$ Å as the unit of length, and $\epsilon/\sigma = 1.65728 \times 10^{-9}$ N as the unit of force. The kinetic temperature is controlled to room temperature via scaling of particle velocities in the bottom layer of the dynamic substrate. Both constant-tip-height and constant-force scan modes were simulated.

First we investigate the process of lowering a tip towards the substrate which is then followed by either raising of the tip or scanning laterally across the surface in either a constant height or constant-force mode. The total force in the normal (z) direction on a rigid four-atom tip (arranged as a tetrahedron) is shown in Fig. 1. Starting with the system at equilibrium and outside the range of interaction with the substrate [see snapshot of the system initial configuration in Fig. 2(a)] the tip is lowered slowly toward the surface. Initially the tip experiences an attractive force ($F < 0$) accompanied by a lifting of the surface atom right below the lowermost tip atom, as seen in the snapshot given in Fig. 2(b). As the tip approaches the surface the attraction diminishes culminating in a repulsion ($F_z > 0$ at ~ 30 tu in Fig. 1) which turns into an attraction in a sudden manner (see Fig. 1 at ≤ 40 tu). Inspection of the real space trajectory of the system reveals that these events are associated with a formation of an interstitial defect where the surface atom is pushed into the interstitial position in the second layer. Further relaxation of the system at tip-to-substrate separation of 1.227 Å (corresponding to a repulsive region of the interatomic potential) results in a *net attractive* force caused by the *tip-induced local reconstruction* [see Fig. 2(c)]. At this point the lateral scan begins (in the $[110]$ direction) at a rate which assures tip-substrate relaxed configurations throughout the scan. As the tip scans (at constant height) over the surface the recorded normal force on it oscillates with the periodicity of the substrate, being repulsive ($F_z > 0$) when the tip traverses the region between atoms and attractive over the substrate atoms (Fig. 1, $t \geq 60$ tu). Snapshots of the system at different tip locations (starting from the tip-substrate equilibrated configuration shown in Fig. 2(d) and

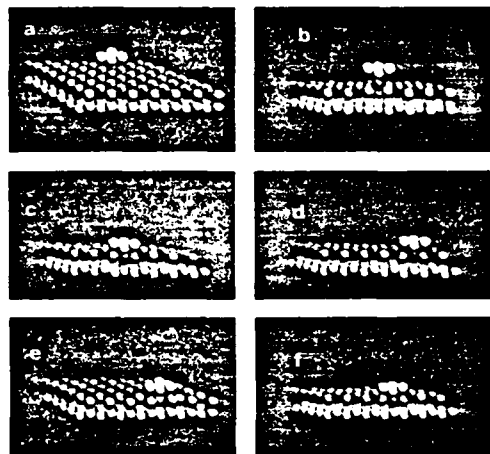


FIG. 2. Snapshots of small static tip-substrate atomic configurations. Tip atoms in bright white and topmost substrate layer as dark spheres. (a) Tip outside range of interaction; (b) tip lowered towards the surface, "lifting" the atom underneath it; (c) tip equilibrated with the surface at the lowered position (1.227 Å from the nominal position of the surface plane), demonstrating the formation of an interstitial defect under the tip (note location of the dark ball directly under the tip); (d) initial configuration before scan (translation of the tip to the left) begins; (e) configuration when the tip scans between substrate atoms; (f) configuration when the tip translated by one unit cell distance, inducing a new interstitial surface defect. The previous tip-induced interstitial [see (d)] returns to his original location in the first atomic layer.

moving the tip laterally to the left) show that when in the region between atoms the tip-induced interstitial returns to his original location in the first atomic layer [see Fig. 2(e)] and a new interstitial defect is generated when the tip moves to a location over the next atom in the surface row [Fig. 2(f)].

The consequences of the interaction between a large dynamic tip consisting of 102 atoms, arranged in four layers and exposing a 16-atom (111) facet, are exhibited in Fig. 3 where snapshots of the system configurations initially [Fig. 3(a)], at the lowered tip configuration [Fig. 3(b)], and after raising the tip [Fig. 3(c)], are shown. As seen, for this reactive system, lifting of the tip results in the formation of a "connective neck" consisting mostly of tip atoms. The variations in the normal component of the force on the tip atoms F_z , potential energy of the tip atom E_p , and their kinetic temperature T , are shown in Fig. 4(b)–4(d), respectively, as well as the temperature of the dynamic substrate and height of the tip assembly from the surface in Figs. (4e) and 4(a), respectively. The snapshots in Fig. 3(a)–3(c) correspond to times $t = 0, 50$, and 120 in Fig. 4. As seen from Fig. 4(b) at the equilibrium configuration, with the tip resting in contact with the surface, the total normal component of the force on the tip atoms is attractive ($F_z < 0$ in the time interval, $20 < t < 60$ tu). Subsequent raising of the tip ($t > 60$) results in an increased attraction between the tip and the substrate atoms and an increase in the potential energy [see Fig. 4(c)] of the tip atoms as the initial crystalline structure of the tip is modified due to strained bonding to the substrate. Further raising of the tip ($t \sim 100$) results in disruption of some of the bonds between the tip and substrate atoms, resulting in a sudden decrease in the force between them [see Fig. 4(b)],

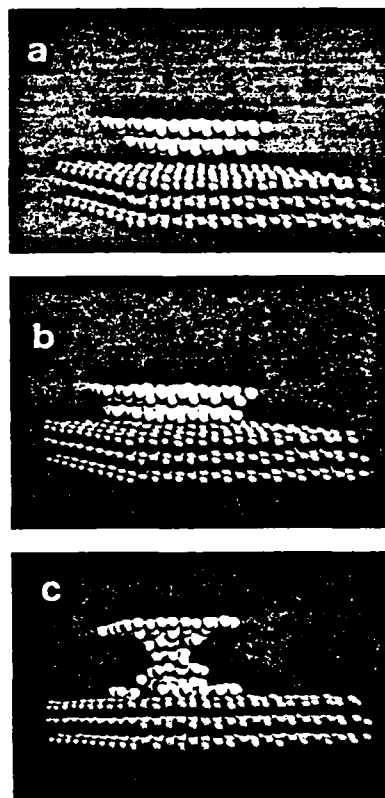


FIG. 3. Atomic configurations as a large faceted dynamical tip initially equilibrated outside the range of interaction (a), is lowered to a distance of 2.91 Å from the surface (b), and following equilibration is raised (c).

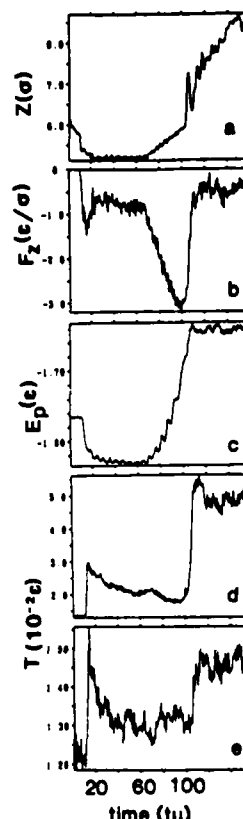


FIG. 4. Variation vs time (in $tu = 7.6634 \times 10^{-14}$ s) of: (a) Center of mass height of the tip-holder assembly, Z ; (b) normal force on the tip, F_z (in units of $e/\sigma = 1.6572 \times 10^{-9}$ N); (c) potential energy of the tip atoms, E_p ; (d) temperature of the tip atoms, (e) kinetic temperature of the dynamic substrate. Simulations are for lowering and raising of a large (102 atom) faceted ordered dynamical tip. See corresponding atomic configurations in Fig. 3.

an increase in the potential energy and a sudden rise in the tip and local substrate temperature [see Figs. 4(d) and 4(e)], yielding eventually the atomic configuration shown in Fig. 3(c).

In constant-force scanning simulations, in addition to the particle equations of motion, the center of mass of the tip-holder assembly, Z , is required to obey $M\ddot{Z} = (\vec{F}(t) - \vec{F}_{\text{ext}}) \cdot \hat{Z} - \gamma\dot{Z}$ where \vec{F} is the total force exerted by the tip-atoms on the static holder at time t , which corresponds to the force acting on the tip atoms due to their interaction with the substrate, \vec{F}_{ext} is the desired (prescribed) force for a given scan, γ is a damping factor, and M is the mass of the holder. In these simulations the system is brought to equilibrium for a prescribed value of $F_{z,\text{ext}}$, and the scan proceeds as described above while the height of the tip-holder assembly adjusts dynamically according to the above feedback mechanism.

In Figs. 5(a)–5(d) and Fig. 6 we show the results for a constant-force scan, for $F_{z,\text{ext}} = -13 \text{ } \epsilon/\sigma$ (corresponding to $-2.15 \times 10^{-8} \text{ N}$, i.e., negative load). In these simulations the substrate consists of six dynamic layers with 100 atoms per layer. Side views of the system trajectories at the beginning and end stages of the scan are shown in Figs. 5(a) and 5(b), and 5(c), respectively. As seen, the tip-substrate interactions induce local modifications of the substrate and tip structure, which are transient (compare the surface structure under the tip at the beginning of the scan [Fig. 5(a)], exhibiting outward atomic displacements of the top-layer atoms, to that at the end of the scan [Fig. 5(c), where that region relaxed to the unperturbed configuration]. The recorded force on the tip holder along the scan direction (x)

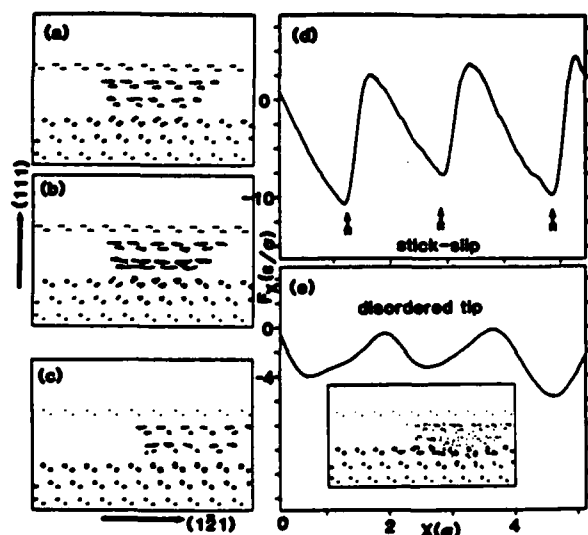


FIG. 5. (a)–(c) Particle trajectories in a constant-force simulation, $F_{z,\text{ext}} = -13.0$ (i.e., $-2.15 \times 10^{-8} \text{ N}$), viewed along the $(10\bar{1})$ direction just before (a) and after (b) a stick-slip event and towards the end of the scan (c), for a large, initially ordered, dynamic tip. (d) The recorded F_x , exhibiting stick-slip behavior. (e) The F_x force in a constant-force scan ($F_{z,\text{ext}} = 1.0$) employing a glassy static tip, exhibiting the periodicity of the substrate. Shown in the inset are the real-space trajectories towards the end of the scan, demonstrating the tip-induced substrate local modifications.

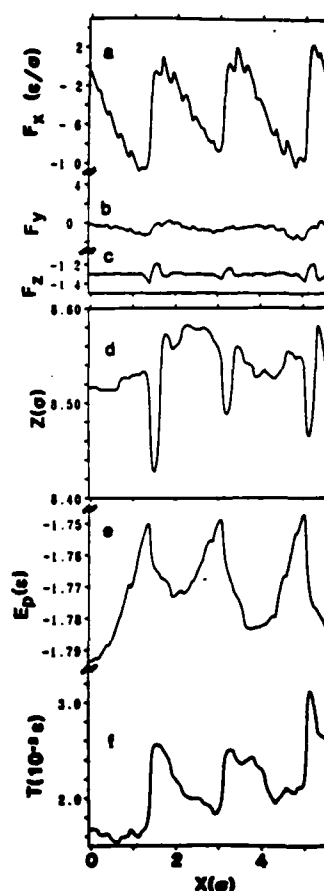


FIG. 6. Constant-force scan simulation at $F_{z,\text{ext}} = -13$ (i.e., negative load of $-2.15 \times 10^{-8} \text{ N}$), employing a large (102 atoms) faceted, ordered dynamical tip. (a)–(c) Variations of the force F_x (along the scan direction) and of the force components normal to it, F_y and F_z . Forces in the units of $1.6572 \times 10^{-9} \text{ N}$. Note that the recorded force in the z direction fluctuates around the prescribed value; (d) center-of-mass height of the tip-holder assembly; (e) potential energy E_p of the tip atoms; (f) kinetic temperature of the tip atoms. Note the discontinuous variation and asymmetry in F_x , signifying stick-slip behavior, and the accompanying variations in E_p and T .

is shown in Fig. 5(d) and in Fig. 6(a), exhibiting a periodic modulation, portraying the periodicity of the substrate. At the same time the normal force F_z fluctuates around the prescribed value [Fig. 6(c)] and no significant variations are observed in the force component normal to the scan direction [F_y in Fig. 6(b)].

Most significant is the stick-slip behavior signified by the asymmetry in F_x [observed also in the real-space atomic trajectories in Figs. 5(a) and 5(b)]. Here, the tip atoms closest to the substrate attempt to remain in a favorable bonding environment as the tip-holder assembly proceeds to scan. When the forces on these atoms due to the other tip atoms exceed the forces from the substrate, they move rapidly by breaking their current bonds to the surface and forming new bonds in a region translated by one unit cell along the scan direction. The detailed energetics of the atomic-scale stick-slip phenomenon can be elucidated from the variations in the potential and kinetic energies of the tip atoms along the scan, shown in Fig. 6(e) and 6(f), respectively. As seen, during the stick stage, the potential energy of the strained bonds between the tip and substrate atoms increases. The slip stage is signified by a discontinuity in the force along the scan direction [F_x , in Fig. 6(a)], and by a sharp decrease in the potential energy [Fig. 6(e)], which is accompanied by a sudden increase in the kinetic temperature of the tip atoms [Fig. 6(f)] as a result of the disruption of the bonds to the substrate and rapid motion of the tip atoms to the new equilibrium positions. We note that the excess kinetic energy

(local heating) acquired by the tip during the rapid slip, dissipates effectively during the subsequent stick stage, via the tip to substrate interaction [see the gradual decrease in T in Fig. 6(f), following the sudden increase].

We note that our constant-force simulation method corresponds to the experiments in Ref. 7 in the limit of a stiff wire (lever) and thus the stick-slip phenomena which we observed are a direct consequence of the interplay between the surface forces between the tip and substrate atoms and the interatomic interactions in the tip. The F_x force which we record corresponds to the frictional force. From the extrema in F_x [Figs. 5(d) or 6(a)] and the load ($F_{z,ext}$) used we obtain a coefficient of friction $\mu = |F_x|/|F_{z,ext}| = 0.77$, in the range of typical values obtained from tribological measurements in vacuum, although we should caution against taking this comparison rigorously.

Results for a constant-force scan at a positive load ($F_{z,ext} = 0.1$, i.e., 1.66×10^{-10} N), employing the large faceted tip, are shown in Fig. 7. As seen from Fig. 7(d), the center-of-mass height of the tip and holder assembly from the surface, Z , exhibits an almost monotonic decrease during the scan, in order to keep the force on the tip atoms around the prescribed value of 0.1 [see Fig. 7(e)]. At the same time the potential energy of the tip increases. This curious behavior corresponds to a "smearing" of the tip as revealed from the real-space trajectories shown in Figs. 7(a)–7(c). Compari-

son of the atomic configurations at the beginning [Fig. 7(a)], during the scan [Fig. 7(b) corresponding to $X \sim 1\sigma$, demonstrating a slip] and towards the end of the scan [Fig. 7(c)] shows that as a result of the interactions between the tip and substrate atoms, the bottom layer of the tip adheres to the substrate and thus in order to maintain the same force on the tip holder throughout the scan (as required in the constant-force scan mode) the tip assembly must move closer to the substrate. These simulations demonstrate that in reactive tip-substrate systems, even under relatively small loads, rather drastic structural modifications may occur, such as "coating" of the substrate by the tip (or vice versa).

The frictional force obtained in simulations employing a disordered rigid 102-atom tip, prepared by quenching of a molten droplet, scanning under a load $F_{z,ext} = 1.0$ are shown in Fig. 5(e). The significance of this result lies in the periodic variation of the force, reflecting the atomic structure of the substrate. This demonstrates that microscopic investigations of structural characteristics and tribological properties of crystalline substrates are not limited to ordered tips.⁷

Finally, we note two most recent studies of tip-substrate interactions involving other materials. Employing an empirically constructed graphite potential and a potential for diamond²⁴ (both based on a reparametrization of the SW potentials, and in the case of graphite augmented by interlayer Lennard-Jones interactions), it was shown^{24a} that for forces stated in the experimental literature, a monoatomic tip would cause very large relaxations of the graphite substrate extending over a large spatial extent,⁸ with an eventual penetration of the surface at $\sim 5 \times 10^{-8}$ N. Furthermore, it was shown that by assuming that the AFM tip carries a graphite flake, a wide variety of images seen by the atomic force microscope can be reproduced and correlated with relative rotations of the flake with respect to the scanned substrate. In other studies,²⁵ employing the embedded atom method (EAM), interactions between metal tips and metal substrates have been investigated. These studies demonstrate that as a consequence of the metallic cohesion, metallic tips lowered onto metallic substrates adhere to the substrate ("pressure welding") resulting in plastic deformation upon separation signified by a pronounced hysteresis in the force versus distance records (upon loading and unloading), similar to the observations in recent AFM experiments.²⁶

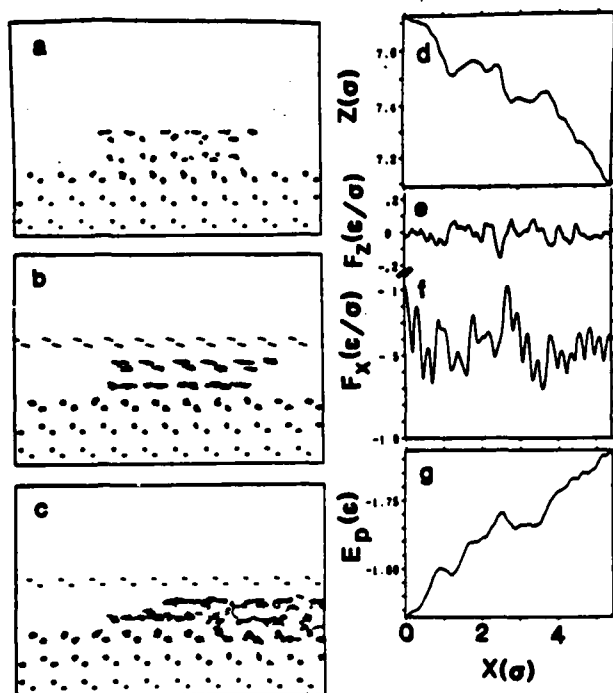


FIG. 7. Constant scan simulation at $F_{z,ext} = 0.1$ (i.e., 1.6572×10^{-10} N), employing a large (102 atoms), initially, ordered dynamic tip. (a)–(c) Real-space particle trajectories at selected times during the scan, beginning (a), middle (b), and end (c), respectively. Note that the bottom layer of the tip adheres to the substrate surface (c); (d) Center-of-mass height of the tip-holder assembly during the scan, as a function of scan distance, $\sigma = 2.0951$ Å. Note the decrease in height associated with the adherence of the bottom tip atoms to the substrate [see (c)]. (e), (f) Normal force F_z and tangential force in the direction of the scan F_x during the scan. (g) Potential energy of the tip atoms E_p during the scan.

III. DYNAMICS OF BOUNDED THIN LIQUID FILMS

Studies of nonequilibrium systems, flow in particular, present immense theoretical and technical challenges. Coupled with the basic conceptual problems presented by nonequilibrium phenomena is the technological motivation related to the molecular design of fluids of desired rheological²⁷ and hydrodynamical characteristics for lubrication purposes. Lubricating fluids are made usually of polymeric molecules (sometime in colloidal suspension) which are characterized by structural and shear-stress relaxation times ranging from milliseconds to minutes, and the relevant flow rates are of the order of the reciprocal of these times. Thus, the Weissenberg number²⁷ for these materials (the product of shear rate and relaxation time) is of the order of

unity. While simulations of phenomena on the above time scales are computationally prohibitive, it is possible to study the nature of the rheological processes occurring in these systems via simulations of simpler fluids sheared at the same Weissenberg number.²⁸ Simple Lennard-Jones systems exhibit such "corresponding state" behavior.

To investigate the nature and properties of bounded thin fluid films at equilibrium and under shear, we have conducted systematic MD simulations of such systems under various external conditions and for a variety of interaction parameters. We demonstrate our results for a system composed of: (i) two fcc solid slabs each consisting of three dynamic and three static layers (with 70 particles/layer) exposing the (111) surface with the particles interacting via a 6-12 Lennard-Jones (LJ) potential [see Eq. (1), Sec. IV]. While periodic boundary conditions are imposed in directions parallel to the surface plane the system (dynamic solids and confined fluid) thickness in the [111] direction evolves dynamically under a load of $0.25 \epsilon_{ss}/\sigma_{ss}^3$ (where ϵ_{ss} and σ_{ss} are the LJ parameters for the intersolid interactions), and (ii) 150 fluid particles of equal size, bounded between the dynamic solid interfaces, and interacting between themselves via a LJ potential with a well depth parameter $\epsilon_{ff} = \epsilon_{ss}/10$, and with the solid by $\epsilon_{fs} = (\epsilon_{ss}\epsilon_{ff})^{1/2}$. The temperature of the system is controlled at $T = 0.074$ (in reduced LJ units, i.e., ϵ_{ss}), slightly above the melting temperature of the fluid, via scaling of particles' velocities in the two dynamic layers which are not in direct contact with the liquid in each of the bounding solid slabs, which thus serve as a heat bath (i.e., particles in the solid layers at the interface and the fluid particles evolve freely with no temperature control, transferring heat to the substrate slab in a natural manner).

The density profile in the direction normal to the interface ([111], Z direction) at equilibrium ($T = 0.074$) is shown in Fig. 8(b) exhibiting layering in the fluid,²⁹ and short-time real-space trajectories of the solid and fluid layers at the interface exhibiting intralayer order and interlayer registry are shown in Fig. 9(a). The slab thickness (in units of $7\sigma_{ss}$) vs time (in reduced LJ time units, tu) is shown in Fig. 8(a) with the end of the equilibrium simulation corresponding to $t < 75$. At time $t = 75$ we apply a sudden shear velocity of $0.1 \sigma_{ss}/tu$ along the $[1, \bar{1}, 0]$ (x) direction to the static portions of the solid slabs (which as a result start translating in opposite directions since the velocities are applied to the opposing solid slabs in opposite senses). As seen from Fig. 8(a), upon application of the shear perturbation, the thickness of the system initially increases slightly (in major part in the fluid region which is set in motion in response to the shear perturbation) followed first by a steady decrease and subsequently by an abrupt drop (at $t \approx 165$). Inspection of the density profiles at an intermediate time $\sim t = 160$ [Fig. 8(c)] and after steady-state is achieved [$t \approx 210$, Fig. 8(d)] reveals that the change in the fluid film thickness is due to a collapse of the system from three to two fluid layers, which corresponds to an increase in areal density of the fluid layers by $\sim 20\%$. The pronounced intralayer structure of the fluid during steady-state shear is shown in Fig. 9(b). Accompanying this structural transition in the fluid is a marked increase in the peak-to-peak fluctuations of the internal shear

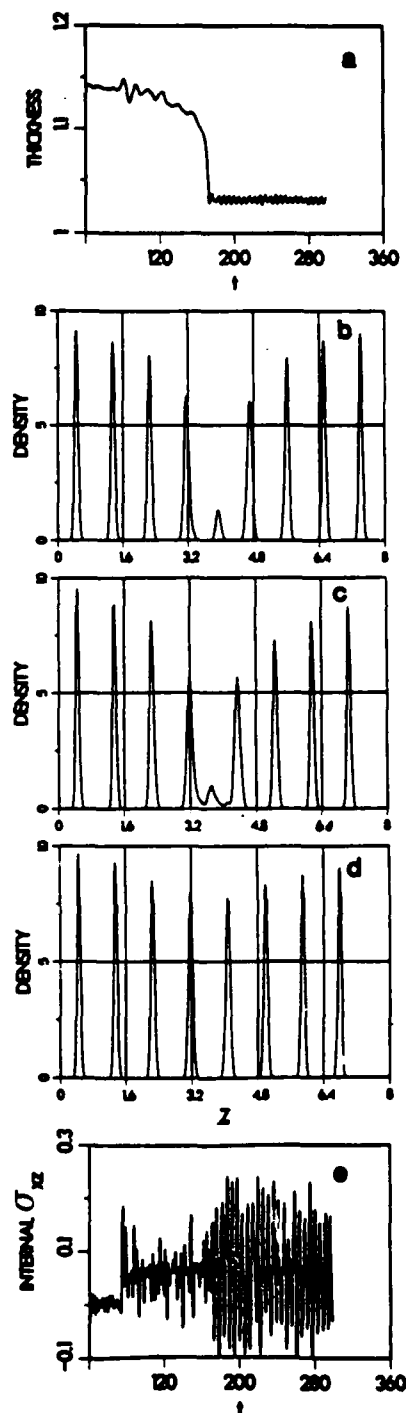


FIG. 8. Results of MD simulations of a fluid confined between parallel solid regions. (a) System thickness (in units of $7\sigma_{ss}$) vs time [in LJ tu]. For $t < 70$ system at equilibrium at $T = 0.074 \epsilon_{ss}$. For $t > 75$ system under shear. (b) Density profile in the z ([111]) direction of the sheared system at $t = 130$ showing three dynamic solid layers on each side of a layered fluid (middle three layers). The middle fluid layer contains ~ 20 particles. (c) Same as (b) but under shear at $t = 160$ [see (a)]. (d) Same as (a) but at steady state under shear ($t = 210$) exhibiting the transition to a two-layer, structured fluid. z distance in (b)–(d) in units of σ_{ss} . (e) Internal shear stress (σ_{xz} , in units of $\epsilon_{ss}/\sigma_{ss}^3$) in the system vs time exhibiting an increase in peak-to-peak fluctuation upon the structural transition in the fluid.

stress (σ_{xz}) of the system (calculated from the instantaneous trajectories) as seen in Fig. 8(e). The very regular fluctuations in thickness (after collapse) seen in Fig. 8(a) coincide in frequency, with the passing of $(1, \bar{1}, 0)$ rows in the

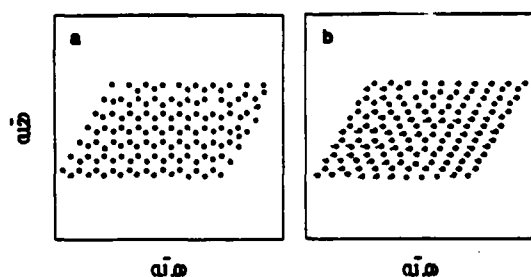


FIG. 9. (a) Short-time real-space trajectories of particles in the interfacial solid (filled circles) and fluid (empty circles) layers, exhibiting intralayer order and interlayer registry at equilibrium. (b) Same as (a) at steady state under shear. Note that the fluid layer under these conditions is denser than at equilibrium [compare to (a)]. The positions of the atoms at the start of the short-time interval are in the middle of the circles.

slip plane, indicating persistent order on both sides of the slip plane. These phenomena have similar characteristics to those observed recently by Israelachvili using an extension of the surface force apparatus,³ indicating a structural dynamical mechanism which (in addition to film drainage) can be operative in such systems. We should note that for the above shear velocity the collapse of the film does not occur for a fluid film consisting of 160 particles. The properties and response of the system (including film drainage) for various film thicknesses, loads and shear velocities are under investigation. Finally, we note that in simulations of thick fluid films (e.g., three times thicker than in the above example), under low shear rates we have found¹⁷ similar interfacial layering (involving 2–3 fluid layers) which decays into the middle of the fluid film, with the latter region exhibiting properties (viscosity and structure) similar to a bulk fluid under similar conditions. However, at higher shear rates the interfacial liquid-layering is much less pronounced and in addition non-Newtonian flow occurs.

Finally, recent theoretical studies in our laboratory³⁰ have shown evidence for shear-induced ordering in atomic and molecular liquids which have been subsequently observed using the surface force apparatus.^{30b}

These results and studies of the dependencies of the flow characteristics on the strength of the fluid–solid interaction and the composition and complexity of the fluid demonstrate the potential utility of MD simulations in tribological molecular design problems.

IV. DYNAMICAL SIMULATIONS OF STRESS, STRAIN AND FINITE DEFORMATIONS

Common observations related to tribological phenomena, and of thermomechanical properties and response of materials in general, are usually made at the continuum level.³¹ Consequently, (and naturally) the development of theoretical understanding of these phenomena followed the “continuum modelling” approach.³¹ The methodology of the development of these models is based on the principles of mass, momentum and energy balance, and the formulation of constitutive equations. While the mathematical formulation of

classical models of the mechanical response of matter (such as the classical theories of elasticity and hydrodynamics) achieved a high degree of sophistication, current focus is on the incorporation of knowledge about the microscopic behavior of materials in continuum models which attempt to describe macroscopic observations. This is done via the introduction, into the continuum models, of a set of state variables which provide averaged (coarsened) representations of the relevant microscopic quantities. In addition we should note that most applied models of mechanical response are limited to the elastic (small spatial deformation) and linear (small rates of application of the external perturbation) regimes. Attempts to incorporate inelastic response and non-linear effects result in a great (often prohibitive) complexity.

To gain knowledge about the energetics and atomic scale mechanisms and to identify and determine characteristic material and ambient parameters which underlie and govern the properties and response of materials requires experimental and theoretical methods which probe physical systems with refined spatial and temporal resolution. As we discussed above molecular dynamics (MD) simulations afford such investigations.

Traditionally, MD simulations have been employed in studies of systems of fixed shape and size of the periodically replicated calculational cell (i.e., constant volume simulations). More recently, methods for simulating systems in which the volume and shape of the calculational cell may vary dynamically have been developed,^{32–38} opening the way to investigations of a large number of materials phenomena in which the dynamical freedom of the system to change volume and/or structure (or phase) is essential. In addition, a number of methods have been developed for simulations of flow and hydrodynamical systems^{39–42} which allow detailed investigations of these nonequilibrium phenomena. Using molecular dynamics techniques various studies of the mechanical properties of solids and fluids have been reported. Among the investigations of solid systems we note studies of stressed solids and crack propagation,^{43–48} dislocation energetics and dynamics,⁴⁶ structural transformations in crystal lattices under uniaxial tension or compression,^{33,37,49,50} sliding and migration of grain boundaries,³⁷ simulations of plastic deformations³⁸ and shock wave dynamics,^{51,52} studies of stressed interfaces,^{38,40} and calculations of elastic coefficients using MD simulations.⁵³

We have investigated^{38,40} using MD simulations the microscopic dynamical response, deformation, and stress relief mechanisms at crystalline solid interfaces subject to externally applied perturbations. (Constant thermodynamic tension, constant strain-rate and isoexternal-stress simulations have been performed.) The objectives of these studies were: (i) identification of the mechanisms for solid interfacial systems of deformation, stress accumulation and relief and the dynamical response to external perturbations, (ii) identification of the dependence of the above phenomena on material characteristics, such as bonding strength, atomic sizes and interface crystallography and on ambient conditions (thermally adiabatic versus isothermal), and (iii) the development and critical assessment of MD simulation methods for investigations of the above phenomena.

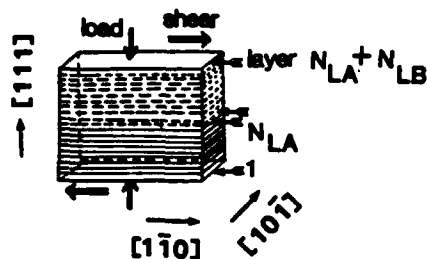


FIG. 10. A schematic of the calculational cell. N_{LA} is the number of layers in the A (hard) material and N_{LB} the number of layers in the B (soft) material. The interface is between layers N_{LA} and $N_{LA} + 1$. The direction of the applied load and shear stresses are indicated. Three-dimensional periodic boundary conditions are employed in the simulations.

In these studies we focus on the mechanisms and dynamics of the response of a system containing an interface between two materials to external stresses. The model system which we employ in our simulations consists of N particles (N_A of type A and N_B of type B , $N_A + N_B = N$) interacting via pairwise 6-12 Lennard-Jones (LJ) potentials:

$$V(r) = 4\epsilon_{\alpha\beta} \left[\left(\frac{\sigma_{\alpha\beta}}{r} \right)^{12} - \left(\frac{\sigma_{\alpha\beta}}{r} \right)^6 \right], (\alpha, \beta) = A, B, \quad (1)$$

where A and B represent two types of materials. The solid is set up initially in a fcc crystalline structure, with N_L (111) layers (N/N_L particles per layer) with the Z axis along the $[111]$ direction,³⁴ and three-dimensional periodic boundary conditions are used (see Fig. 10). The well-depth parameter ($\epsilon_{\alpha\beta}$) of the interaction potential between particles in layers 1 through N_{LA} is taken to be twice that for particles in layers $N_{LA} + 1$ through N (i.e., $\epsilon_{AA} = 2\epsilon_{BB}$) corresponding to a soft, solid, lubricating material (the B system) pressed between hard-material slabs (the A system). In order to isolate the dependence of the system response on the interaction strength (potential depth) parameter ϵ from that due to differences in the atomic sizes (and thus interatomic distances) associated with the parameter σ in the LJ potential, we have performed first simulations in which $\epsilon_{AA} = 2\epsilon_{BB}$ and $\sigma_{AA} = \sigma_{BB}$, and then simulations in which $\sigma_{BB} = 1.5\sigma_{AA}$. The interspecies LJ potential parameters were chosen as $\sigma_{AB} = (\sigma_{AA} + \sigma_{BB})/2$ and $\epsilon_{AB} = (\epsilon_{AA}\epsilon_{BB})^{1/2}$. In the following we use reduced units³⁵ where energy and temperature are expressed in units of ϵ_{AA} , length in units of σ_{AA} , stress in units of $(\epsilon_{AA}/\sigma_{AA}^3)$ and the time unit (tu) is $(m_A/\epsilon_{AA})^{1/2}\sigma_{AA}$. In the integration of the equations of motion we used a time step $\Delta t = 0.0075$ tu which results in energy conservation (to six significant figures) for extended runs.

Following equilibration of the initial system at a reduced temperature of $T = 0.11$ (note that a pure bulk LJ crystal melts at $T \approx 0.7$, and thus, since $\epsilon_{BB} = \epsilon_{AA}/2$, the bulk melting point of the soft material B is half that of the A material) under a load of 0.5 in the $[111]$ (Z) direction we apply the external perturbation. In simulations of applied thermodynamic tension [isoenthalpic, isotension and constant number of particle, N , simulations, i.e., the (\mathcal{H}, τ, N) ensemble] we apply to the system a thermodynamic tension tensor τ (which is related to the external stress tensor) in the $[1, \bar{1}, 0]$ direction (see Fig. 10) at a rate of $\dot{\tau}_{xx} = 0.00125 (\epsilon/\sigma^3)/\Delta t$

and follow the evolution of the system until it fails [to keep the system from a rigid rotation a symmetric thermodynamic tension tensor τ is applied, (i.e., $\tau_{xx} = \tau_{yy}$)].

To investigate the dependence on the thermal ambient conditions we distinguish between simulations where the system is thermally isolated during the application of the shear and simulations where isothermal conditions are maintained. As the system evolves under the applied shear it develops internal stresses which are calculated using the positions and forces on the particles.³⁸ These simulations allow us to determine the nature of structural transformations and the critical external stresses (or critical strains in constant strain-rate simulations) which characterize the transition from elastic to inelastic response regimes, and the critical yield stress (where the internal stresses vanish).

The mechanical response and energetic characteristics of the system can be investigated via layer decomposition of the system properties. Results at a constant external $\tau_{xx} = 0.81$ and adiabatic thermal conditions for a system composed of nine layers each of equal size particles of hard and soft materials (with 70 particles/layer and the interface located between layers 9 and 10), which exhibited yield at a critical value of $\tau_{c,xx} = 0.86$, are shown in Figs. 11 and 12. Inspection of the real space trajectories revealed that at this value of stress (which is below the critical yield value) the system undergoes a structural transformation involving interlayer motion leading to stacking fault generation (between layers 12 and 13) inside the soft material and slip.

In Fig. 11(a) and 11(b) we depict the per layer xz component of the internal stress for the interface layers (layer 5, 8, and 9 of the hard material and layers 10-14 of the soft mate-

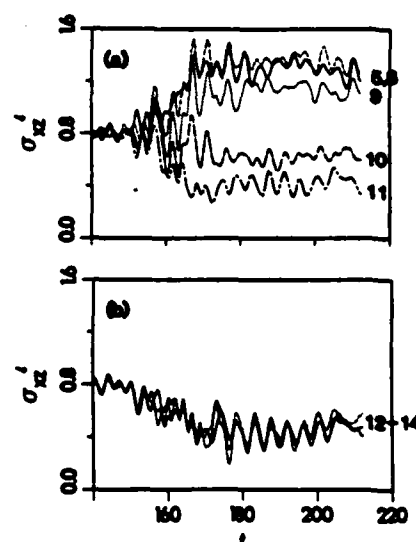


FIG. 11. Per-layer internal stresses (σ'_{xx}) vs time (in tu) for a simulation at $\tau_{xx} = 0.81$ under adiabatic conditions. Layers 5, 8, and 9 in the hard materials and 10 and 11 in the soft ones are shown in (a). The stresses in layers 12-14 in the soft material are shown in (b). The interface is between layers 9 and 10. Note the variation in the internal stresses at the time of the structural transformation. The internal stresses in the interior of the soft material (10-14) decrease with layer 10 exhibiting pinning by the hard material. The stress relief in the soft material is accompanied by stress accumulation in the hard material (layers 5-9).

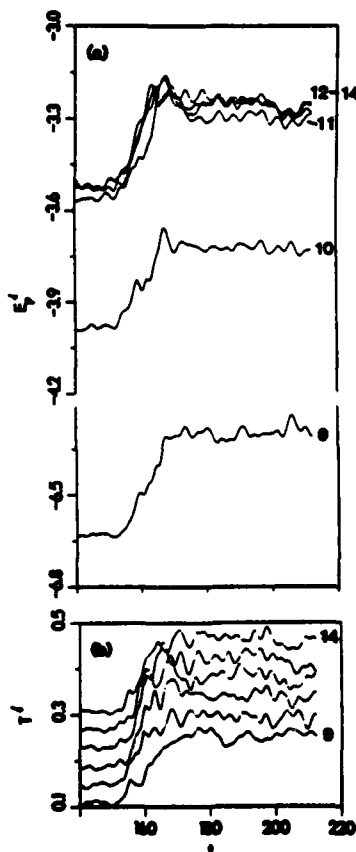


FIG. 12. Per layer potential energies, E_p' , in (a), and temperatures T' in (b), for the system simulated at $\tau_{xz} = 0.81$ under adiabatic conditions.

rial). From these figures we observe that the generation of the structural transition involves a gradual decrease in the internal σ_{xz} component in layers 11–14 of the soft material while the variation in the stress in layer 10 [the atomic plane of the soft material (*B*) adjacent to the hard material (*A*), see Fig. 10] is smaller. As seen from Fig. 11(a) the *stress relief* process and the associated structural transformation in the *soft material* are accompanied by a *stress accumulation* in the *interfacial region of the hard material* (layer 9). In addition we observe periodic oscillations in the internal stress (most pronounced for layers 11–14) past the structural transformation period, as the system relaxes in the new state after the structural transformation events.

The energetics of the system is explored via the time records of the perlayer potential energies (E_p') and temperature (T') shown in Figs. 12(a) and 12(b), respectively. From the potential energy curves we find that the potential energy of particles in layer 11 (second layer from the interface, see Fig. 10) in the soft material is initially lower than that of layers 12–14, which are further removed from the interface, since particles in that layer are within the range of the stronger interaction with the hard substrate [$\epsilon_{AB} = \epsilon_{AA}\epsilon_{BB}^{1/2}$]. The potential energy of particles in the interfacial soft material layer (layer 10) adjacent to the hard material is lower by about -0.4ϵ than the value for layer 11. This extra stabilization “pins” this interfacial layer to the hard substrate. The potential energy of the topmost layer of the hard material (layer 9) is lower further by about -2.6ϵ . The potential energies of both layers 9 and 10 increase due to

the structural transformation. Since the system in this set of calculations is thermally isolated, the structural change is accompanied by a temperature increase as seen from Fig. 12(b) (where the curves for successive layers, starting from 10 and up, are displaced vertically by 0.04ϵ). Note however that the final temperature after the transformation is below the melting temperature for both materials.

To investigate the dependence of the system properties on the mismatch in atomic sizes between the two interfacing materials, we have performed simulations in which the well-depth parameters were chosen as before but the σ parameters were chosen such that the atoms in the soft (*B*) material are characterized as having a larger size, i.e., $\sigma_{BB} = 1.5\sigma_{AA}$ and $\sigma_{AB} = 1.25\sigma_{AA}$. From these simulations we have determined that the critical yield value of the thermodynamic tension in this system is $\tau_{c,xz} = 0.62 \pm 0.01$ (and the corresponding external stress $\sigma_{c,xz} = 0.51 \pm 0.01$), which are considerably lower than the corresponding values found for the equal-atomic size systems. Moreover, unlike the previous cases, where yield was preceded by an external stress regime in which the system responded inelastically via a sequence of structural transformations, for the present system (in which the atomic sizes across the interface differ) no such behavior is observed. Furthermore, the whole soft system responds in unison, starting at the interfacial layer and up into the material. These observations can be understood when considering that as a consequence of the larger atomic size the atoms of the soft material at the interface average over the corrugation of the potential due to the substrate, resulting in an effective potential surface which exhibits smaller variations for lateral displacements parallel to the interface plane, and consequently a reduced resistance to shear.

The results of our extensive investigations³⁸ may be summarized as follows: (i) For interfacial systems which are characterized by differing interatomic interaction strengths (i.e., the interface is between a hard and soft material), the system responds to an applied nonisotropic perturbation (applied shear or strain) first elastically and then via stress relief mechanisms which involve structural transformations (stacking fault formation and interlayer slip). For larger values of the external forces, eventual yield occurs. (ii) Critical values of the external perturbation required in order to bring about inelastic response (structural transformations and yield) have been determined. Our simulations demonstrate that the critical values are smaller for a system under thermally adiabatic conditions than for an isothermal environment. The origin of the difference lies in the dissipation of the generated thermal energy under isothermal conditions, which necessitates larger values of the external perturbations in order to overcome potential barriers for structural modifications and eventual yield. (iii) The cohesive interatomic interactions at the interface between a hard substrate and a soft material result in “pinning” of the soft material at the interface (1–3 atomic layers). As a result the response of the system to the external perturbation (stress relief via plastic as well as structural transformations) occurs in a “shear band” consisting of a few atomic layers inside the soft material, which for our model system are located at about 1–3

layers away from the original (unstressed) interface. The stress relief in the soft material is accompanied by stress accumulation in the hard substrate. (iv) MD simulations for interfacing hard and soft materials, which in addition are characterized by differing atomic sizes, reveal the important role played by atomic size mismatch in determining the atomic-scale mechanism of response. For such system it was found that no adhesive "pinning" occurs at the interface, and that the soft (and larger atomic size) material responds as a whole with no distinct structural transformations preceding the yield point. The critical yield stress value for this system is significantly lower than that found for the corresponding equal-atomic-size system. (v) Comparison of our results in this study for the [111] interface with our previous investigations of the [100] interface⁴⁰ demonstrates the dependence of the critical values of the shear stresses on the crystallographic orientation of the interface, as well as of certain details of the stress relief mechanisms.

ACKNOWLEDGMENTS

These studies were supported by the U. S. DOE Grant No. FG05-86ER-45234, the DARPA-Hughes, Tribological Fundamentals Program and the NSF Tribology Program. Most of the simulations were performed on the CRAY-XMP at NMFEC, Livermore, California, the CDC CYBER-990 at the Georgia Institute of Technology and at the Pittsburgh supercomputer center.

- ¹R. P. Feynman, in *Miniaturization*, edited by H. D. Gilbert (Reinhold, New York, 1961), p. 282.
- ²J. N. Israelachvili, *Acc. Chem. Res.* **20**, 415 (1987); *Proc. Nat. Acad. Sci. U.S.A.* **84**, 4722 (1987).
- ³J. N. Israelachvili, P. M. McGuiggan, and A. M. Homola, *Science* **240**, 189 (1988).
- ⁴G. Binnig, H. Rohrer, Ch. Gerber, and E. Weibel, *Phys. Rev. Lett.* **50**, 120 (1983); G. Binnig and H. Rohrer, *IBM J. Res. Dev.* **30**, 355 (1986).
- ⁵G. Binnig, C. F. Quate, and Ch. Gerber, *Phys. Rev. Lett.* **56**, 930 (1986).
- ⁶P. K. Hansma and J. Tersoff, *J. Appl. Phys.* **61**, R1 (1986); R. J. Colton and J. S. Munday ONR Review (in press).
- ⁷C. W. Mate, G. M. McClelland, R. Erlandsson, and S. Chiang, *Phys. Rev. Lett.* **59**, 1942 (1987).
- ⁸J. M. Soler, A. M. Baro, N. Garcia, and H. Rohrer, *Phys. Rev. Lett.* **57**, 444 (1986); see comment by J. B. Pethica, *ibid.* **57**, 3235 (1986).
- ⁹J. M. Gimzewski and R. Moller, *Phys. Rev. B* **36**, 1284 (1987).
- ¹⁰See articles in *Molecular Dynamics Simulations of Statistical-Mechanical Systems*, Fermi School, XCVII, Corso, Varenna, 1985, edited by G. Cicotti and W. G. Hoover (Soc. Ital. di Fisica, Bologna, 1986).
- ¹¹U. Landman, R. N. Barnett, C. L. Cleveland, W. D. Luedtke, M. W. Ribarsky, D. Scharf, and J. Jortner, in *Material Research Society Symposium Proceedings* (Materials Research Society, Boston, 1985), Vol. 63, p. 273.
- ¹²F. F. Abraham, *Adv. Phys.* **35**, 1 (1986); *J. Vac. Sci. Technol. B* **2**, 534 (1984).
- ¹³*Mater. Res. Soc. Bull.* **XIII** (2), 14 (1988).
- ¹⁴U. Landman, R. N. Barnett, C. L. Cleveland, J. Luo, D. Scharf, and J. Jortner, *AIP Conf. Proc.* **162**, 200 (1987).
- ¹⁵D. W. Heerman, *Computer Simulation Methods* (Springer, Berlin, 1986).
- ¹⁶*Computer Simulations of Solids*, edited by C. R. A. Catlow and W. C. Machord (Springer, Berlin, 1982).
- ¹⁷U. Landman, in *Computer Simulation Studies in Condensed Matter Physics: Recent Developments*, edited by D. P. Landau, K. K. Mon, and H.-B. Schuttler (Springer, Berlin, 1988).
- ¹⁸See U. Landman and W. D. Luedtke in *Atomistic Modeling in Materials: Beyond Pair-Potentials*, edited by V. Vitek (Plenum, New York, 1988).
- ¹⁹See U. Landman, D. W. Luedtke and M. W. Ribarsky, in *New Materials Approaches to Tribology: Theory and Applications*, edited by L. E. Pope, L. Fehrenbacher and W. O. Winer (Materials Research Society, Boston, 1989).
- ²⁰F. H. Stillinger and T. A. Weber, *Phys. Rev. B* **31**, 5262 (1985).
- ²¹U. Landman, W. D. Luedtke, R. N. Barnett, C. L. Cleveland, M. W. Ribarsky *et al.*, *Phys. Rev. Lett.* **56**, 155 (1986); F. F. Abraham and J. Q. Broughton, *ibid.* **59**, 64 (1987); W. D. Luedtke and U. Landman, *Phys. Rev. B* **37**, 4656 (1988); U. Landman, W. D. Luedtke, M. W. Ribarsky, R. N. Barnett, and C. L. Cleveland, *Phys. Rev. B* **37**, 4637, 4647 (1988); F. F. Abraham and I. P. Batra, *Surf. Sci.* **163**, L752 (1985).
- ²²F. F. Abraham, I. P. Batra, and S. Ciraci, *Phys. Rev. Lett.* **60**, 1314 (1988).
- ²³U. Landman, W. D. Luedtke, and A. Nitzan, *Surf. Sci.* **210**, L177 (1989).
- ²⁴(a) F. F. Abraham and I. P. Batra, *Surf. Sci. Lett.* **209**, L125 (1989); (b) W. D. Luedtke and U. Landman (unpublished).
- ²⁵W. D. Luedtke, U. Landman, and R. N. Barnett (to be published).
- ²⁶N. A. Burnham, I. L. Singer, and R. J. Colton (private communication).
- ²⁷H. A. Barnes, *Dispersion Rheology* (Royal Society of Chemistry, London, 1980).
- ²⁸D. M. Heyes, *Mol. Phys.* **57**, 1265 (1986).
- ²⁹For MD results and earlier references about layering of interfacial fluids see U. Landman, R. N. Barnett, C. L. Cleveland, and R. H. Rast, *J. Vac. Sci. Technol. A* **3**, 1574 (1985).
- ³⁰(a) M. W. Ribarsky, U. Landman, and W. D. Luedtke (to be published), reported at the 35th AVS National Symposium, October, 1988, Atlanta, Ga. (b) J. N. Israelachvili (private communication).
- ³¹See review on "Continuum Modeling" by L. Davison in *Mat. Res. Soc. Bull.* **8**, 14 (1988); see also *Approaches to Modeling of Friction and Wear*, edited by F. F. Ling and C. H. T. Pan (Springer, Berlin, 1988).
- ³²H. C. Andersen, *J. Chem. Phys.* **72**, 2384 (1980).
- ³³M. Parrinello and A. Rahman, *J. Appl. Phys.* **52**, 7182 (1981).
- ³⁴J. R. Ray and A. Rahman, *J. Chem. Phys.* **80**, 4423 (1984).
- ³⁵For an extension to metallic systems see R. N. Barnett, C. L. Cleveland, and U. Landman, *Phys. Rev. Lett.* **54**, 1679 (1985); *ibid.* *Phys. Rev. Lett.* **55**, 2035 (1985).
- ³⁶W. G. Hoover, *Phys. Rev. A* **118**, 111 (1983).
- ³⁷See reviews by S. Yip and M. Parrinello in Ref. 10.
- ³⁸M. W. Ribarsky and U. Landman, *Phys. Rev. B* **38**, 9522 (1988).
- ³⁹See recent reviews by D. J. Evans and G. P. Morriss, *Comput. Phys. Rep.* **1**, 297 (1984), and D. J. Evans and W. G. Hoover, *Ann. Rev. Fluid Mech.* **18**, 243 (1986).
- ⁴⁰M. W. Ribarsky and U. Landman in *Approaches to Modeling of Friction and Wear*, edited by F. F. Ling and C. H. T. Pan (Springer-Verlag, New York, 1988), p. 159.
- ⁴¹S. Sutton, M. W. Ribarsky, and U. Landman, *J. Chem. Phys.* (to be published).
- ⁴²C. L. Cleveland, *J. Chem. Phys.* **89**, 4987 (1988).
- ⁴³G. J. Dienes and A. Paskin, in *Atomistic of Fracture*, edited by R. M. Latanision and J. R. Pickens (Plenum, New York, 1983), p. 671; A. Paskin, K. Sieradzki, D. K. Som, and G. J. Dienes, *Acta Metall.* **31**, 1253 (1983).
- ⁴⁴B. DeCelia, A. S. Argon, and S. Yip, *J. Appl. Phys.* **54**, 4864 (1983) and references therein.
- ⁴⁵W. T. Ashurst and W. G. Hoover, *Phys. Rev. B* **14**, 1465 (1976).
- ⁴⁶W. G. Hoover, N. E. Hoover, and W. C. Moss, *J. Appl. Phys.* **50**, 829 (1979); see also A. J. C. Ladd and W. G. Hoover, *Phys. Rev. B* **26**, 5469 (1982).
- ⁴⁷P. C. Gehlan, G. T. Hahn, and M. F. Kanninen, *Scri. Metall.* **6**, 1087 (1972).
- ⁴⁸See review by M. I. Baskas and M. S. Daw in *Computer Simulations in Materials Science*, edited by R. J. Arsenault, J. Beeler, and D. M. Esterling (American Society for Metals, Cleveland, 1988).
- ⁴⁹R. Najafabadi and S. Yip, *Scri. Metall.* **17**, 1199 (1983).
- ⁵⁰J. R. Ray and A. Rahman, *J. Chem. Phys.* **82**, 4243 (1985).
- ⁵¹B. Moran, A. J. C. Ladd, and W. G. Hoover, *Phys. Rev. B* **28**, 1756 (1983).
- ⁵²B. L. Holian, *Phys. Rev. A* **37**, 2562 (1988).

⁵³M. D. Kluge, J. R. Ray, and A. Rahman, J. Chem. Phys. 85, 4028 (1986); M. D. Kluge and J. R. Ray, Phys. Rev. B 37, 4132 (1988).

⁵⁴This interface orientation was chosen in view of our previous studies of the [001] interface (see Ref. 40), where it was found that slip occurs for the Lennard-Jones fcc system along the (111) planes. Note that the values for external stress given in Ref. 40, should be interpreted as those for the thermodynamic tension.

⁵⁵If the interaction parameters are chosen such that they correspond to the cohesive energy and lattice constant of nickel ($\epsilon = 3.54 \times 10^{-13}$ erg, $\sigma = 2.49$ Å, and atomic mass $m = 9.75 \times 10^{-23}$ g) a reduced temperature $T = 0.11$ corresponds to 300 K, the reduced melting temperature $T_m = 0.7$ corresponding to 2000 K, the reduced unit of stress or load to 2.4×10^7 g/cm² (or 2.4×10^{10} dynes/cm²), and the reduced time unit (tu) corresponds to 4.1×10^{-13} s.

SURFACE SCIENCE LETTERS

**DYNAMICS OF TIP-SUBSTRATE INTERACTIONS
IN ATOMIC FORCE MICROSCOPY ***

Uzi LANDMAN, W.D. LUEDTKE and A. NITZAN

School of Physics, Georgia Institute of Technology, Atlanta, GA 30332, USA

Received 22 November 1988; accepted for publication 5 December 1988

Dynamical interactions between a scanning tip and a silicon substrate are investigated using molecular dynamics simulations of both the constant-height and constant-force scan modes. Localized temporary and permanent modifications of the substrate occur, depending on tip-substrate separation and scan geometry. Implications for resolving structural and force characteristics in scanning tip spectroscopies, employing atomically sharp as well as large ordered or disordered tips are discussed.

The developments of scanning tunneling microscopy [1] (STM), the related atomic force microscopy (AFM) [2], and the surface force apparatus (SFA) [3,4] revolutionized our perspectives and abilities to probe the morphological and electronic structure and the nature of interatomic forces in materials, as well as opened new avenues [5] for microscopic investigations and manipulations of technological systems and phenomena such as tribology [4,6], lithography and in biochemical applications. In both STM and AFM a tip is brought close to the surface and either the tunneling current (STM) or deflection of the cantilever holding the tip (AFM) are monitored as the surface is scanned. Of particular interest are questions related to the nature of the tip-substrate interactions and the dynamical response of the substrate (and tip) which may result in temporary or permanent modifications of the local properties [7,8] and be reflected in the recorded data.

In this paper we investigate the dynamics of the tip-substrate interactions via molecular dynamics simulations employing a realistic interatomic interaction potential for silicon (the Stillinger-Weber (SW) potential [9]) which has been used recently in a number of investigations [10-14] of bulk, surface and interface properties of this material. Since both the substrate and tip consist of the same material, these simulations correspond to the case of a reactive tip-substrate system [11-14]. Our simulations [12-14], in both the constant-

* Work supported by US DOE under grant No. FG05-86ER45234, and by the DARPA-Hughes Tribology Program.

tip-height and constant-force scan modes, reveal that the local structure of the surface can be stressed and modified as a consequence of the tip-substrate dynamical interaction, even at tip-substrate separations which correspond to weak interaction. For large separations these perturbations anneal upon advancement of the tip while permanent damage can occur for smaller separations. For the material that we simulated (Si), we do not find long-range elastic deformations, which may occur in other circumstances [7] depending upon the elastic properties of the material and the nature of interactions. The characteristics of the data depend upon the geometry of the scan, the degree of perfection of the substrate and the temperature. We identify various dynamical events including stick-slip phenomena, which could be experimentally resolved, using current estimates [1,2,5], and which would influence the analysis of data, as well as pointing to ways in which the tip could be used for atomic scale manipulations of the material.

In our simulations the system consists of 4 layers of dynamic Si particles with 49 (or 100) atoms per layer, exposing the (111) surface, and interacting with 2 layers of a static Si substrate of the same structure (calculations with systems of 6 dynamic layers and a larger number of particles/layer yield very similar results). The 2D calculational cell, defined by the $(1\bar{1}0)$ and $(10\bar{1})$ vectors, is periodically repeated parallel to the (111) plane. Two types of tips were employed in our simulations. First, we have used a sharp tip [1,2,5] simulated by 4 Si atoms in an initial tetrahedral configuration, "mounted" on and interacting with 2 layers of silicon atoms which serve as a holder. In addition we have employed larger tips consisting of 102 atoms, which were either ordered (exposing a 16 atoms (111) planar facet) or disordered. The equations of motion, governed by the SW potential [9], which contains 2- and 3-body interactions (V_2 and V_3 respectively), are integrated using a 5th order predictor-corrector algorithm with a time step $\Delta t = 1.15 \times 10^{-3}$ ps (or 0.015 tu where $\text{tu} = 7.6634 \times 10^{-14}$ s). Throughout we use $\epsilon = 50$ kcal/mol as the unit of energy, $\sigma = 2.0951$ Å as the unit of length, and $\epsilon/\sigma = 1.65728 \times 10^{-9}$ N as the unit of force. The reduced units of length X^* , Y^* and Z^* , along the $(1\bar{1}0)$, $(10\bar{1})$ and (111) directions are 12.82σ , 12.82σ , and 5.8333σ , respectively. The kinetic temperature is controlled via scaling of particle velocities in the bottom layer of the dynamic substrate.

Both constant-tip-height and constant-force scan modes were simulated. In the first mode following equilibration at room temperature, with the tip outside the range of interaction, the tip is lowered slowly ($5.4 \times 10^{-4} \sigma/\Delta t$) to a prescribed height. Studies at 3 initial tip heights, h_i ($i = 1, 3$), corresponding to distances of 2.91, 2.345 and 1.227 Å between the lowest tip atom and the uppermost layer of the substrate, were performed. h_1 , h_2 and h_3 correspond to the attractive, equilibrium, and repulsive regions of the interparticle potential, respectively. To faithfully simulate the laboratory process, which is much slower than can be achieved in computer simulations, and record data for

structurally relaxed tip-substrate configurations we have adopted the following scan and data accumulation procedure: (a) The system is first equilibrated for $200 \Delta t$ with the tip at the desired height. (b) Lateral scans (along X^* (110)) consist of: (i) equilibration for $150 \Delta t$ followed by $150 \Delta t$ of data collection and averaging, (ii) motion of the tip assembly for $50 \Delta t$ to a new scan point (8 scan points per 2D unit cell length, covering in each lateral scan 3 unit cells), after which step (i) is repeated. In exploratory studies we found that the results of the simulations are not modified in any substantial way by increasing the equilibration periods. Results for 2 lateral scans at each height are described, denoted by $h_i(1)$ for the scan on top of an atomic row, and by $h_i(2)$ for the scan mid-distance between rows.

In the constant-force simulations in addition to the particle equations of motions the center of mass of the tip-holder assembly, Z , is required to obey $M\ddot{Z} = (F(t) - F_{\text{ext}}) \cdot \hat{Z} - \gamma\dot{Z}$ where F is the total force exerted by the tip atoms on the static holder at time t , which corresponds to the force acting on the tip atoms due to their interaction with the substrate, F_{ext} is the desired (prescribed) force for a given scan, γ is a damping factor and M is the mass of the holder. In these simulations the system is brought to equilibrium for a

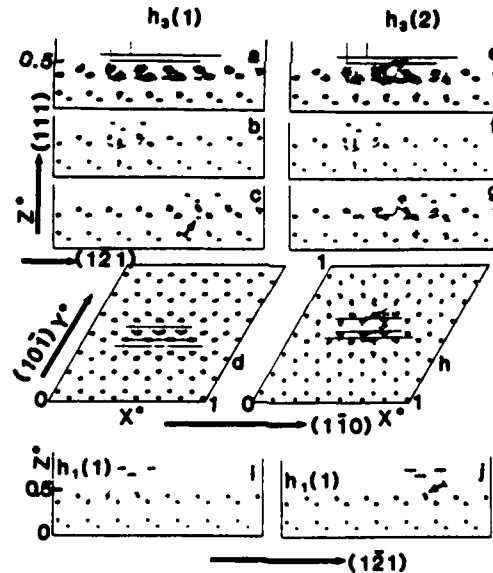


Fig. 1. (a-d) Particle trajectories for the low-tip, $h_3(1)$, scan: (a, d) complete scan; (b, c) at beginning and towards the end of the scan, respectively. In (a-c) view along the (101) direction, in (d) view along (111). (e-h) same as (a-d) for between-the-rows, $h_3(2)$, scan; note the damage caused in the substrate. (i, j) trajectories at the beginning and towards the end of the high-tip, $h_1(1)$ scan. Arrows in (c) and (j) point to induced defects. The tip atoms are located on the horizontal lines above the substrate, scanning from left to right.

prescribed value of F_{ext} , and the scan proceeds as described above while the height of the tip-holder assembly adjusts dynamically according to the above feed-back mechanism.

In fig. 1 we show particle trajectories, viewed from the side along the (101) direction and from the top (along the (111) direction, d and h) for constant tip-height simulations and a static tip (i.e., hard but reactive tip), at two tip heights, h_1 and h_3 . Trajectories for a complete scan at the low tip height $h_3(1)$, are shown in a and d (the scan direction is from left to right). The horizontal lines are the static tip-particle trajectories (only 3 tip particles out of the 4 are visible from this viewing direction). In figs. 1b and 1c particle trajectories are shown at the beginning and towards the end of the scan. As seen in fig. 1b the interaction with the tip triggers local displacements of substrate particles. In particular, the atom in the top layer right below the tip drops to an *interstitial position* in the second layer. This is seen clearly in fig. 1c, where the interstitial atom is marked by an arrow. Note that once the tip advances, the localized defect induced by the tip anneals (compare the left part of the scan in figs. 1b and 1c). In comparison, locating the tip at $h_1(1)$, in the region of attractive interaction, results in a *localized outward displacement* of atoms in the substrate top layer (see figs. 1i and 1j, where the displaced particle is marked by an arrow). The dependence on the scan geometry which affects the relative tip to substrate atoms bond distances, orientations and coordination and subsequently the resultant forces, is demonstrated by comparing the trajectories shown in figs. 1a-1d and 1e-1h. As seen, the between-row scan, $h_3(2)$, produces a more significant damage to the surface due to the bonding geometry generating top layer vacancies (2 atoms attached to the tip, figs. 1e and 1g).

Records of the forces on the tip atoms for the three scan heights versus tip location and versus time are shown in figs. 2a-2f and 2g and 2h, respectively. We start with the time-histories of the $h_1(1)$ and $h_3(1)$ scans (figs. 2g and 2h). For the high-tip scan, $h_1(1)$ (fig. 2g) the tip experiences throughout an attractive force ($F_z < 0$) towards the substrate, increasing as the tip advances laterally in the regions between substrate atoms. A different situation is encountered in the low-tip scan, $h_3(1)$ (fig. 2h). Here, as the tip is lowered it initially attracts to the surface, followed by a decrease in the force as the tip enters the repulsive region, and subsequently experiencing a repulsive interaction ($F_z > 0$ at ~ 30 tu). This is then followed by a sharp attraction (~ 40 tu), culminating in a resultant *attractive force* ($F_z \approx -1 \epsilon/\sigma$), although the tip at this point is in intimate contact with the surface, which would have been expected to yield a strong repulsion. The dynamical mechanism underlying the observed attraction is the generation of surface interstitial defects (see also figs. 1a-1d). Thus, the interaction with the tip can induce *local* rearrangement in the substrate and consequently can alter (even reverse the sign) of the resultant recorded forces. Further lateral scanning over substrate atoms is

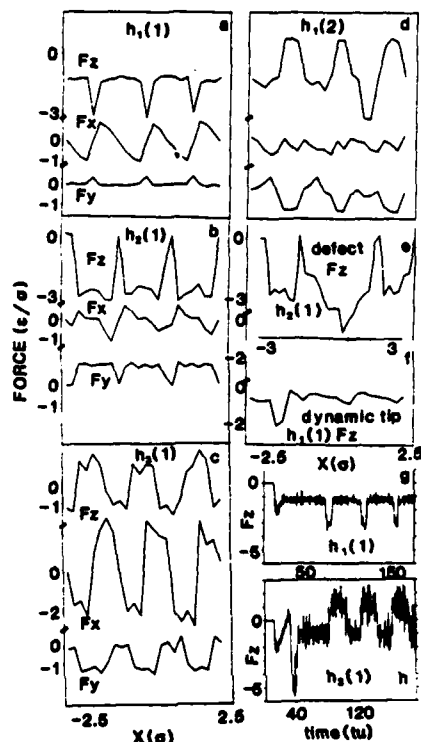


Fig. 2. (a-c) Forces on the tip atoms for the high, intermediate and low tip scans along the X ($1\bar{1}0$) direction for scan 1. (d) Forces on the tip for the between-the-rows scan (2); the F_z force on the tip in a $h_2(1)$ scan for a defective surface is shown in (e) and in an $h_1(1)$ scan for a dynamic tip (f); (g, h) F_z force on the tip in high, $h_1(1)$, and low, $h_3(1)$, scans versus time, respectively. These time records include the stage of lowering the tip. All others start after equilibration at the indicated height. Distance in units of σ , time in units of t_u and force in units of $\epsilon/\sigma = 1.6572 \times 10^{-9}$ N.

characterized by periodic oscillations in the force which reflect the substrate periodicity.

The dependence of the character of the recorded forces versus position on tip height is illustrated in figs. 2a-2c for scan 1. These records were obtained after the initial equilibration, with the tip lowered to the desired height. Significant variations in the magnitudes and character of the forces are observed depending upon the tip separation from the surface. For example, the F_z component at $h_1(1)$ is overall attractive with sharp negative spikes which for the intermediate tip height, $h_2(1)$, turn into broad attractive plateaus when the tip is scanning between surface atoms. For the low-tip configuration, fig. 2c, passage between surface atoms is exhibited by broad repulsive peaks. Spatial variations of the potential energy surface are exhibited

by comparison of the two scans at the h_1 height (figs. 2a and 2d). Note in particular the changes in F_z , and the change in magnitudes of F_x and F_y . These characteristics portraying the surface structure and the spatial variation of the potential are within the current estimates of resolution in AFM [2].

A comparison between the F_z records for an ideal surface (fig. 2b) and for a defective surface (fig. 2e) reveals the scale and character of variations caused by microscopic modifications in the surface morphology. Here, the surface was initially equilibrated with a top layer vacancy at the location of the fourth atom from the right in the row directly under the lower-most tip atom (see fig. 1d). Examination reveals that in course of the scan the tip caused major rearrangement of the defective region via a complicated sequence of atomic displacements involving first and second layer atoms.

Simulations were also performed, at constant-height, for tip atoms which were allowed to evolve dynamically. The recorded F_z force for a high-tip scan, $h_1(1)$, shown in fig. 2f, exhibits a decrease in magnitude originating from a relaxation of the tip, occurring mainly at the beginning of the scan, and shifts and pronounced asymmetry of characteristic features (compare to F_z in fig. 2a), connected with a stick-slip behavior exhibited by the lower-most tip atom as the scan progresses (see below).

We turn next to *constant-force simulations* employing an initially ordered tip consisting of 102 atoms (exposing a 16 atom (111) facet) scanning a 6 layer substrate with 100 atoms/layer. In these simulations both the substrate and tip atoms respond dynamically and the scan rate is half of that described above. In fig. 3 we show results for a scan, for a constant force value $F_{z,ext} = -13.0$ (i.e., 2.15×10^{-8} N). Side views of the system trajectories at the beginning and end stages of the scan are shown in figs. 3a, 3b and 3c, respectively. As seen the tip-substrate interaction induces local modifications of the substrate and tip structure, which are transient and similar to those observed in the constant-height simulations. The recorded force on the tip-holder in the X^* direction is shown in fig. 3d. While the normal force, F_z , fluctuates around the prescribed value as required, the force along the scan direction (F_x , in fig. 3d) exhibits a periodic modulation portraying the periodicity of the substrate. Most significant is the stick-slip behavior signified by the asymmetry in F_x (observed also in the real-space atomic trajectories in figs. 3a and 3b). Here, the tip atoms closest to the substrate attempt to remain in a favorable bonding environment as the tip-holder assembly proceeds to scan. When the forces on these atoms due to the other tip atoms exceed the forces from the substrate, they move rapidly to minimize the F_x force, by breaking their current bonds to the surface and forming new bonds in a region translated by one unit cell along the scan direction. We note that our constant-force simulation method corresponds to the experiments in ref. [6] in the limit of a stiff wire (lever) and thus the stick-slip phenomena which we observed are a direct consequence of the interplay between the surface forces

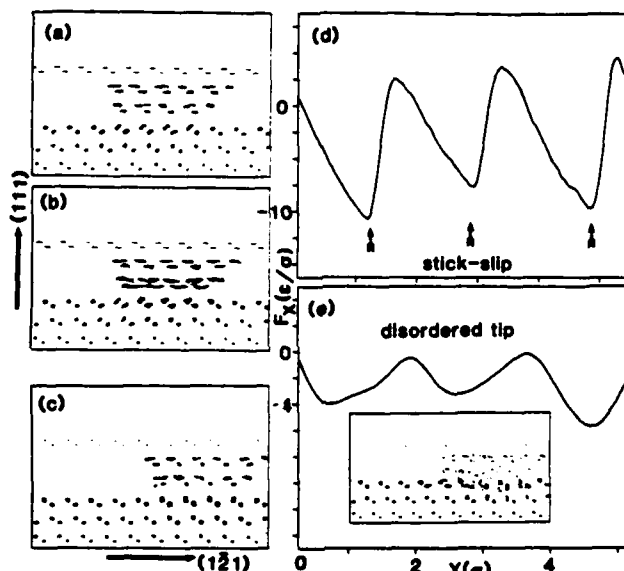


Fig. 3. (a-c) Particle trajectories in a constant-force simulation viewed along the $(10\bar{1})$ direction just before (a) and after (b) a stick-slip event and towards the end of the scan (c), for a large, initially ordered, dynamic tip. (d) The recorded F_x , exhibiting stick-slip behavior. (e) The F_x force in a constant-force scan ($F_{z,\text{ext}} = 1.0$) employing a glassy static tip, exhibiting the periodicity of the substrate. Shown in the inset are the real-space trajectories towards the end of the scan, demonstrating the tip-induced substrate local modifications.

and interatomic interactions in the tip. The F_x force which we record corresponds to the frictional force. From the extrema in F_x (fig. 3d) and the load ($F_{z,\text{ext}}$) used we obtain a coefficient of friction $\mu = |F_x|/|F_{z,\text{ext}}| = 0.77$, in the range of typical values obtained from tribological measurements in vacuum.

Finally, we show in fig. 3e the frictional force obtained in simulations employing a disordered static 102-atom tip, prepared by quenching of a molten droplet, scanning under a load $F_{z,\text{ext}} = 1.0$. The significance of this result lies in the periodic variation of the force reflecting the atomic structure of the substrate. This demonstrates that microscopic investigations of structural characteristics and tribological properties of crystalline substrates are not limited to ordered tips [6].

References

- [1] G. Binnig, H. Rohrer, Ch. Gerber and E. Weibel, Phys. Rev. Letters 50 (1983) 120; G. Binnig and H. Rohrer, IBM J. Res. Develop. 30 (1986) 355.
- [2] G. Binnig, C.F. Quate and Ch. Gerber, Phys. Rev. Letters 56 (1986) 930.
- [3] J.N. Israelachvili, Acc. Chem. Res. 20 (1987) 415.

- [4] J.N. Israelachvili, P.M. McGuiggan and A.M. Horrolo, *Science* 240 (1988) 189.
- [5] P.K. Hansma and J. Tersoff, *J. Appl. Phys.* 61 (1986) R1;
R.J. Colton and J.S. Murday, *ONR Rev.*, in press.
- [6] C.M. Mate, G.M. McClelland, R. Erlandsson and S. Chiang, *Phys. Rev. Letters* 59 (1987) 1942.
- [7] J.M. Soler, A.M. Baro, N. Garcia and H. Rohrer, *Phys. Rev. Letters* 57 (1986) 444;
see comment by J.B. Pethica, *Phys. Rev. Letters* 57 (1986) 3235.
- [8] J.K. Gimzewski and R. Moller, *Phys. Rev. B* 36 (1987) 1284.
- [9] F.H. Stillinger and T.A. Weber, *Phys. Rev. B* 31 (1985) 5262.
- [10] U. Landman, W.D. Luedtke, R.N. Barnett, C.L. Cleveland, M.W. Ribarsky, E. Arnold, S. Ramesh, H. Baumgart, A. Martinez and B. Khan, *Phys. Rev. Letters* 56 (1986) 155;
F.F. Abraham and J.Q. Broughton, *Phys. Rev. Letters* 59 (1987) 64;
W.D. Luedtke and U. Landman, *Phys. Rev. B* 37 (1988) 4656;
U. Landman, W.D. Luedtke, M.W. Ribarsky, R.N. Barnett and C.L. Cleveland, *Phys. Rev. B* 37 (1988) 4637, 4647;
F.F. Abraham and I.P. Batra, *Surface Sci.* 163 (1985) L752.
- [11] F.F. Abraham, I.P. Batra and S. Ciraci, *Phys. Rev. Letters* 60 (1988) 1314.
- [12] See U. Landman and W.D. Luedtke, in: *Atomistic Modeling in Materials: Beyond Pair-Potentials*, Ed. V. Vitek (Plenum, New York, 1988).
- [13] See U. Landman, in: *Computer Simulation Studies in Condensed Matter Physics: Recent Developments*, Eds. D.P. Landau, K.K. Mon and H.-B. Schuttler (Springer, Berlin, 1988).
- [14] See U. Landman, D.W. Luedtke and M.W. Ribarsky, in: *New Materials Approaches to Tribology: Theory and Applications*, Eds. L.E. Pope, L. Fehrenbacher and W.O. Winer (MRS, Boston, 1989).

4

Accepted in Science
To be published;
April 27, 1990

Atomistic Mechanisms and Dynamics of Adhesion, Nanoindentation and Fracture

Uzi Landman and W. D. Luedtke

School of Physics, Georgia Institute of Technology, Atlanta, GA 30332

and

Nancy A. Burnham and Richard J. Colton

Surface Chemistry Branch, Code 6177, Naval Research Laboratory,

Washington, DC 20375-5000

Abstract

Molecular dynamics simulations and atomic force microscopy are employed to investigate the atomistic mechanisms of adhesion, contact formation, nano-indentation, separation and fracture which occur when a nickel tip interacts with a gold surface. The theoretically predicted and experimentally measured hysteresis in the force versus tip-to-sample distance relationship, found upon approach and subsequent separation of the tip from the sample, is related to inelastic deformation of the sample surface characterized by adhesion of gold atoms to the nickel tip and formation of a connective neck of atoms. At small tip-sample distances, mechanical instability causes the tip and surface to jump-to-contact which leads to adhesion induced wetting of the nickel tip by gold atoms. Subsequent indentation of the substrate results in the onset of plastic deformation of the gold surface. The atomic-scale mechanisms underlying the formation and elongation of a connective neck, which forms upon separation, consist of structural transformations involving elastic and yielding stages.

INTRODUCTION

Understanding the atomistic mechanisms, energetics and dynamics underlying the interactions and physical processes which occur when two materials are brought together (or separated) is fundamentally important to basic and applied problems such as adhesion [1-7], contact formation [3-16], surface deformations [17-22,7,16], materials elastic and plastic response characteristics [17-22], materials hardness [23-25], microindentation [6,10,24-27], friction and wear [16,18b,28-30] and fracture [31,32]. These considerations have motivated for over a century [17,18,1,3] extensive theoretical and experimental research endeavors of the above phenomena and their technological consequences. Most theoretical approaches to these problems, with a few exceptions [7,14-16], have been anchored in continuum elasticity and contact mechanics [17-22]. Similarly, until quite recently [33-36] experimental observations and measurements of surface forces and the consequent materials response to such interactions have been macroscopic in nature.

The everlasting quest to understand and observe natural phenomena on refined microscopic scales has led to the development of conceptual and technological devices allowing the interrogation of materials with increasing resolution. On the experimental front the developments of the surface force apparatus (SFA) [34], of scanning tunneling microscopy (STM) [35] and of the related atomic force microscopy (AFM) [33], broaden our perspectives and abilities to probe the morphology, electronic structure and nature of interatomic forces in materials, as well as enhance our ability to manipulate materials on the atomic scale [36].

On the theoretical front, recent advances in the formulation and evaluation of the energetics and interatomic interactions in materials [7,37] coupled with the development and implementation of computational methods and simulation techniques [7,38], open new avenues for investigations

of the microscopic origins of complex materials phenomena. In particular large-scale molecular dynamics computer simulations, which are in a sense computer experiments, where the evolution of a system of interacting particles is simulated with high spatial and temporal resolution via direct integration of the particles' equations of motion, have greatly enhanced our understanding of a broad range of materials phenomena.

Although our knowledge of interfacial processes occurring when two material bodies are brought together has significantly progressed since the original presentation by Heinrich Hertz before the Berlin Physical Society in January 1881 of his theory of the contact of elastic bodies [17], full microscopic understanding of these processes is still lacking. Moreover, it has been recognized that continuum mechanics is not fully applicable as the scale of the material bodies and the characteristic dimension of the contact between them are reduced [22,39]. Furthermore, it had been observed [18b,25] that the mechanical properties of materials exhibit a strong dependence on the size of the sample (small specimens appear to be stronger than larger ones). Since the junctions between contacting solids can be small, their mechanical properties may be drastically different from those of the same materials in their bulk form. Consequently, the application of the newly developed theoretical and experimental techniques to these problems promises to provide significant insights concerning the microscopic mechanisms and the role of surface forces in the formation of microcontacts and to enhance our understanding of fundamental issues pertaining to interfacial adherence, microindentation, structural deformations, and the transition from elastic to elastoplastic or fully developed plastic response of materials. Additionally, studies such as those described in this paper allow critical assessment of the range of validity of continuum-based theories of these phenomena and could inspire improved analytical formulations. Finally, knowledge of the

interactions and atomic-scale processes occurring between small tips and material surfaces, and their consequences, is of crucial importance to optimize, control, interpret and design experiments employing the novel tip-based microscopies [6,7,13,14,16, 30,33-36,40-45].

To this end we investigate in this paper theoretically [7] and experimentally [6] the interactions between a metallic tip (Ni) and a gold surface, chosen mainly due to differences in their mechanical properties such as elastic moduli, yield, hardness and strength parameters (e.g., the elastic moduli are $21 \times 10^{10} \text{ N/m}^2$ and $8.2 \times 10^{10} \text{ N/m}^2$ for Ni and Au, respectively [46]). The theoretical studies employed molecular dynamics (MD) simulations [7,16] with interatomic interactions described via the many-body potentials obtained by the embedded-atom method (EAM) [47] which have been recently applied with significant success in studies of bulk and surface properties of a number of metallic systems and their alloys. The experimental measurements were performed using AFM configured to measure the force between a tip mounted on a cantilever and the sample surface as a function of tip-to-sample separation [6,45].

Our theoretical simulations reveal the onset of an instability as the tip approaches the sample causing a jump-to-contact (JC) such as described first [14] via calculations employing Lennard-Jones (LJ) potentials and further investigated more recently using different potentials for nickel [15] and other materials [7]. We find that for our system the JC phenomenon is associated primarily with a tip-induced sample deformation which begins when the distance between the proximal atomic layers of the two interfacing materials is approximately 4.2 \AA (i.e., at a separation larger than the equilibrium crystalline interlayer spacings), and that the process involves large atomic displacements ($\sim 2 \text{ \AA}$) occurring over a short time span of $\sim 1 \text{ psec}$. Furthermore, we discovered that lifting the tip from the surface after

contact results in an inelastic deformation of the sample exhibiting ductile extension and the eventual tear, or fracture, of the topmost Au layer which adheres to the Ni tip. The above processes are portrayed in both the results of the simulations and measurements as a marked hysteresis in the force versus distance relationship recorded along the axis of the tip-sample approach/separation. In fact, the process of tear, observed in the simulations during tip-sample separation, is akin to mode-I ductile fracture [31] (i.e., load normal to the fracture plane). Allowing the tip to further advance and penetrate the sample surface beyond the point of contact indents the surface and results in further deformation of the sample characterized by an adhesion-induced flow of gold atoms which wet the edges of the Ni tip, generation of slip planes in the Au lattice and formation of point defects. Separating the tip and sample causes the sample to deform ductilely producing an extended crystalline "neck" that stretches between the sample and adherent layers on the tip until the neck eventually breaks. Throughout much of the elongation process the neck maintains a crystalline layered structure while reducing in cross-sectional area as it extends. The elongation mechanism revealed by the simulations consists of a sequence of elastic and plastic (yielding) stages accompanied by atomic structural rearrangement. Based on the above observations we associate the calculated and measured hystereses in the force versus distance curves with the formation, stretching and breaking of bonds due to adhesion, cohesion and decohesion, and with inelastic deformations induced by the tip-to-substrate interaction.

METHODOLOGY

Prior to the presentation of our results we provide pertinent details of our studies, noting common as well as distinguishing characteristics between the theoretical and experimental modes of investigation.

A. MD Simulations

MD simulations were performed for an Au (001) sample containing 3 static (bottom) and 8 dynamic layers, each consisting of 450 atoms per layer. The sample interacts with a dynamic Ni tip consisting of 1400 atoms arranged originally as a pyramidal (tapered) tip with the bottom layer (closest to the sample) consisting of 72 atoms exposing a (001) surface, the next layer consisting of 128 atoms and the remaining 6 layers containing 200 atoms each. This gives the tip an effective radius of curvature of $\sim 30 \text{ \AA}$ (which is approximately 50-100 times smaller than the tip employed in the experiment). In addition the tip interacts with a static Ni holder consisting of 1176 atoms arranged in three (001) layers. The simulations were performed at 300K with temperature control imposed only on the deepest dynamic layer of the Au sample closest to the static layers. No significant variations in temperature were observed during the simulations. The equations of motion were integrated using a 5-th order predictor-corrector algorithm with a time step $\Delta t = 3.05 \text{ fsec}$.

As aforementioned the interatomic interactions which govern the energetics and dynamics of our system are modeled via the embedded-atom method (EAM) [47] which has been applied recently with significant success to study equilibrium and nonequilibrium properties and processes in metallic elemental and alloy systems [47-49]. In this method, the dominant contribution to the cohesive energy of the material is viewed as the energy to embed an atom into the local electron density provided by other atoms of the system. This background density is determined for each atom as the superposition of electronic densities from the other atoms, evaluated at the location of the atom in question. Thus, the total cohesive energy is represented in the EAM by a many-body embedding functional, supplemented by parametrized short-range pair interactions due to inter-core repulsion. The parameters of the pair-

potentials are determined via fitting to a number of bulk equilibrium properties of the metals and their alloys, such as lattice constants, heats of sublimation, elastic constants, vacancy-formation energies and heats of solution [47].

Following equilibration of the system at 300K with the tip outside the range of interaction, the tip was lowered slowly toward the surface. For the initially equilibrated system we find multilayer relaxation [50] of the Au(001) surface, whereby the first (topmost)-to-second interlayer spacing, d_{12} , contracts by 7.5% and d_{23} expands by 3.5% relative to the interlayer spacing in the bulk. The layer relaxation at the surface of the Ni tip is insignificant and at equilibrium the sides of the tapered part of the tip expose small (111) facets. The calculated surface energies (at 0K) for Ni (001) and Au (001) are 1657 mJ/m^2 and 964 mJ/m^2 , respectively, in close agreement with calculations [47a] employing a slightly different parameterization of the EAM potentials.

Motion of the tip occurs by changing the position of the tip-holder assembly in increments of 0.25 \AA over 500 At. After each increment the system is fully relaxed, i.e., dynamically evolved, until no discernable variations in system properties are observed beyond natural fluctuations.

B. AFM Measurements

Forces may be measured experimentally using AFM [6,33]; both attractive and repulsive forces can be measured as well as the adhesive force necessary to separate the tip and sample surface after contact. Fig. 1 depicts schematically the forces acting between the tip (which is mounted on a cantilever beam) and sample as a function of the separation D between the cantilever tip and sample. The arrows are used to guide the eye throughout the full interaction cycle. The cycle starts with the sample far away and the

cantilever in its rest position. As D decreases, the cantilever bends towards the sample such that at any equilibrium separation D the attractive force, F , balances the restoring force of the cantilever defined by its effective spring constant k times its deflection. However, if the magnitude of the gradient of the attractive force dF/dD exceeds k (point A), the cantilever will jump into contact with the sample (point A'). This instability is governed by the stiffness of the cantilever beam relative to the long-range forces, while in the MD simulations, where the cantilever is modeled by a rigid tip-holder (i.e., an infinitely stiff cantilever beam), the jump-to-contact instability is driven by the inherent stiffness (related to the cohesive strength) of the tip and substrate materials.

On reversing the direction of the sample, the cantilever will jump away from the sample at B to some point B' giving rise to hysteresis in the measured force curve, the magnitude of which depends on k and F . Thus in the experiment, the degree of resolution, i.e., the ability to track the force versus distance curve for all tip-to-surface separations, depends on the selection of the cantilever. For example, if k is at any time less than dF/dD , the dotted segment of the interaction force curve $D_A \leq D \leq D_B$ (see Fig. 1) is inaccessible. However, if k is always greater than dF/dD , as for our experiment, the cantilever dependent instability can be practically eliminated, thus enabling a faithful measurement of the consequences of the tip-to-sample interatomic interactions and the resultant hysteresis, due to adhesion, in the force versus separation curve.

The AFM instrument employs a cantilever beam made from Ni wire (0.25 mm dia.) and bent into the shape of a 'L' whose long and short dimensions are approximately 6 and 2 mm, respectively. The short part of the bent wire was chemically etched with hydrochloric acid into a tip with a radius of curvature of ~ 200 nm as determined by scanning electron microscopy. The cantilever's

spring constant is calculated to be ~ 5000 N/m. Its deflection is measured with a tunneling microscope. Details of the instrumentation are described elsewhere [6]. Whereas in the simulation the tip is moved, in the experiment the sample is moved by means of a piezoelectric actuator at a rate of 5 nm/sec. Sample velocity was chosen to be intermediate to the thermal drift rate (< 1 nm/min) and tunneling microscope slew rate (~ 100 nm/sec).

The AFM measurements were done in a dry box under dry nitrogen using tips and samples that were prepared in air and then quickly transferred to the dry box. The sample was an evaporated Au film (approximately 100 nm thick) that was cleaned in a solution of sodium dichromate and concentrated sulfuric acid and rinsed with distilled water until the surface was hydrophilic.

RESULTS AND DISCUSSION

Measured and simulated force versus distance curves are shown in Figs. 2 and 3, respectively, as well as the calculated potential energy versus distance (Fig. 3c). In both cases results for tip-to-sample approach followed by separation are shown, for adhesive contact (Figs. 2a and 3a) and indentation (Figs. 2b and 3b,3c) studies. As discussed above, the simulations correspond to a case of a rigid cantilever and therefore the recorded properties of the system as the tip-holder assembly approaches or retracts from the sample portray directly consequences of the interatomic interactions between the tip and the sample. The distance scale that we have chosen in presenting the calculated results is the separation (denoted as d_{hs}) between the rigid (static) holder of the tip and the static gold lattice underlying the dynamic substrate. The origin of the distance scale is chosen such that $d_{hs} = 0$ after jump-to-contact occurs ($d_{hs} \geq 0$ when the system is not advanced beyond the JC point and $d_{hs} < 0$ corresponds to indentation). Since the dynamic Ni tip and Au substrate atoms displace in response to the interaction

between them, the distance d_{hs} does not give directly the actual separation between regions in the dynamic tip and substrate material. The actual relative distances, d_{ts} , between the bottom part of the tip (averaged z-position of atoms in the bottom-most layer of the tip) and the surface (averaged z-position of the topmost layer of the Au surface, calculated for atoms in the first layer away from the perturbed region in the vicinity of the tip) are given by the letter symbols in Fig. 3(a,b) Note that the distance between the bottom of the tip and the gold atoms in the region immediately underneath it may differ from d_{ts} . Thus for example when $d_{hs} = 0$ (point D in Figs. 3a,b) the tip to unperturbed gold distance, d_{ts} , is 3.8 Å, while the average distance between the bottom layer of the tip and the adherent gold layer in immediate contact with it is 2.1 Å.

A. Tip-Sample Approach

Comparison of Figs. 2a and 3a reveals similarity between the measured and calculated curves showing a monotonic increase in the magnitude of the attractive force as the tip approaches the sample and a hysteresis during separation. Note, however, that in the experiment (Fig. 2a) the magnitude of the force and the distance from the surface at which it begins to deviate from zero are much larger than in the calculated data (Fig. 3a). These differences are due primarily to differences in tip size and to the neglect of long-range interactions (e.g., van der Waals forces) in the calculations. Also, in the experiment, it is difficult to determine where the cantilever tip is in relation to the surface until contact has already been made. Therefore it is likely that a slight indentation has occurred in the data shown in Fig. 2a. This problem can be alleviated in future experiments by using phase sensitive detection to denote contact and reverse the direction of the sample motion. Other differences between theory and experiment include tip or sample roughness and exposure to air during sample preparation. We stress that in

our experiments cantilever-dependent instability has been ruled out as a possible origin of the observed hysteresis. Furthermore, hysteresis in the piezoelectric actuators used in the instrument is negligible. Rather, the hysteresis originates from dynamical processes induced by the tip-substrate adhesive interactions as revealed by the simulations.

Following an initial slow variation of the force between the Au substrate and the Ni tip we observe in the simulations the onset of an instability, signified by a sharp increase in the attraction between the two (see Fig. 3a as well as Figs. 3b and 3c where the segments corresponding to lowering of the tip up to the point D describe the same stage as that shown in segment AD in Fig. 3a.) which is accompanied by a marked decrease in the potential energy of the system (see sudden drop of E_p in Fig. 3c as d_{hs} approaches zero from the right). We note the rather sudden onset of the instability which occurs only for separations d_{hs} smaller than 0.25 \AA (marked by an arrow on the curve in Fig. 3a). Our simulations reveal that in response to the imbalance between the forces on atoms in each of the materials and those due to intermetallic interactions a jump-to-contact (JC) phenomenon occurs via a fast process where Au atoms in the region of the surface under the Ni tip displace by approximately 2 \AA toward the tip in a short time span of $\sim 1 \text{ ps}$ (see bulging of the gold surface shown in Fig. 4a where the atomic configuration after the JC is depicted). After the jump-to-contact occurs the distance between the bottom layer of the Ni tip and the layer of adherent Au atoms in the region immediately underneath it decreases to 2.1 \AA from a value of 4.2 \AA . In addition to the adhesive contact formation between the two surfaces an adhesion-induced partial wetting of the edges of the Ni tip by Au atoms is observed (see Fig. 4a).

The jump-to-contact phenomenon in metallic systems is driven by the marked tendency of the atoms at the interfacial regions of the tip and

substrate materials to optimize their embedding energies (which are density dependent, deriving from the tails of the atomic electronic charge densities) while maintaining their individual material cohesive binding (in the Ni and Au) albeit strained due to the deformation caused by the atomic displacements during the JC process.

Further insight into the JC process is provided by the local hydrostatic pressure in the materials (evaluated as the trace of the atomic stress tensors [51]) shown in Fig. 5a after contact formation (i.e., point D in Fig. 3a). The pressure contours reveal that atoms at the periphery of the contact zone (at $X = \pm 0.19$ and $Z = 0.27$) are under extreme tensile stress ($\sim 10^5 \text{ atm} = -10^{10} \text{ N/m}^2 = -10 \text{ GPa}$). In fact we observe that the tip as well as an extended region of the substrate in the vicinity of the contact zone are under tension. Both the structural deformation profile of the system and the pressure distribution which we find in our atomistic MD simulations are similar, in general terms, to those described by certain modern contact mechanics theories [19-22] where the influence of adhesive interactions is included.

B. Tip-Substrate Separation After Contact

Starting from contact the force versus distance (F_z vs. d_{hs}) curve exhibits a marked hysteresis seen both experimentally (Fig. 2a) and theoretically (Fig. 3a) as the surfaces are separated. We remark that, in the simulation and the measurements, separating the surfaces prior to contact results in no hysteresis. The hysteresis is a consequence of the adhesive bonding between the two materials and, as demonstrated by the simulation, separation is accompanied by inelastic processes in which the topmost layer of the Au sample adheres to the Ni tip. (See the configuration shown in Fig. 4b which corresponds to the distance $d_{ts} = 7.5 \text{ \AA}$ marked J in Fig. 3a). The mechanism of the process is demonstrated by the pressure contours during

liftoff of the tip shown in Fig. 5b, recorded for the configuration marked G ($d_{ts} = 5.5 \text{ \AA}$ in Fig. 3a). As seen the maximum tensile stress is located near the edges of the adhesive contact. We further observe that the diameter of the contact area decreases during lifting of the tip, resulting in the formation of a thin "adhesive neck" due to ductile extension, which stretches as the process continues, ultimately breaking at a distance d_{ts} of $\sim 9-10 \text{ \AA}$. The evolution of adhesion and tear mechanisms which we observe can be classified as mode-I fracture [31], reemphasizing the importance of forces operating across the crack in modeling crack propagation [31,32].

C. Indentation

We turn now to theoretical and experimental results recorded when the tip is allowed to advance past the jump-to-contact point, i.e., indentation (see Figs. 2b, 3(b,c), and 4c). As evident from Fig. (3b), decreasing the separation between the tip and the substrate causes first a decrease in the magnitude of the force on the tip (i.e., less attraction, see segment DL) and an increase in the binding energy (i.e., larger magnitude of the potential energy, shown in Fig. 3c). However, upon reaching the point marked L in Fig. (3b) a sharp increase in the attraction occurs, followed by a monotonic decrease in the magnitude of the force till $F_z = 0$ (point M in Fig. 3b) at $d_{ts} = 0.8 \text{ \AA}$. The variations of the force (in the segment DLM) are correlated with large deformations of the Au substrate (see the atomic configuration in Fig. 4c, corresponding to point M in Fig. 3b). In particular, the nonmonotonic feature (near point L) results from tip-induced flow of gold atoms which relieve the increasing stress via wetting of the sides of the tip. Indeed the atomic configurations (Figs. 4c and 5c) display a "piling-up" around the edges of the indenter due to atomic flow driven by the deformation of the Au substrate and the adhesive interactions between the Au and Ni atoms. Further

indentation is accompanied by slip of Au layers (along (111) planes) and the generation of interstitial defects (see atomic trajectories and atomic configuration, corresponding to point M, in Figs. 4c and 5c, respectively). In addition, the calculations predict that during the indentation process a small number of Ni atoms diffuse into the surrounding Au, occupying substitutional sites. Furthermore the calculated pressure contours at this stage of indentation, shown in Fig. 5d, demonstrate that the substrate surface zone in the vicinity of the edges of the tip is under tensile stress, while the deformed region under the tip is compressed with the maximum pressure (8.2 GPa) occurring at about the fifth Au layer below the center of the Ni tip-indenter. The general characteristics of the pressure (and stress) distributions obtained in our indentation simulations correspond to those associated [11,19,23] with the onset and development of plastic deformation in the substrate.

Experimentally, advancing the sample past the contact point is noted by the change in slope of the force as the increasing repulsive forces push the tip and cantilever back towards their rest position, as shown in Fig. 2b. We remark that the calculated pressures from the simulations compare favorably with the average contact pressure of ~ 3 GPa determined experimentally [45] by dividing the measured attractive force by the estimated circular contact area of radius 20 nm.

D. Tip-Substrate Separation After Indentation

Reversal of the direction of the tip motion relative to the substrate from the point of zero force (point M in Fig. 3b) results in the force- and potential energy- versus distance curves shown in Figs. 3b and 3c. The force curve exhibits first a sharp monotonic increase in the magnitude of the

attractive force (segment MN in Fig. 3b) with a corresponding increase in the potential energy (Fig. 3c). During this stage the response of the system is mostly elastic accompanied by the generation of a small number of vacancies and substitutional defects in the substrate. Past this stage the force and energy curves versus tip-to-sample separation exhibit a nonmonotonic behavior which is associated mainly with the process of elongation of the connective neck which forms between the substrate and the retracting tip.

To illustrate the neck formation and elongation process we show in Fig. 6 a sequence of atomic configurations corresponding to the maxima in the force curve (Fig. 3b, points marked O, Q, S, U, W and X). As evident, upon increased separation between the tip-holder and the substrate a connective neck forms consisting mainly of gold atoms (see atomic configurations shown in Fig. 4d and 4e). The mechanism of elongation of the neck involves atomic structural transformations whereby in each elongation stage atoms in adjacent layers in the neck disorder and then rearrange to form an added layer, i.e., a more extended neck of a smaller cross-sectional area. Throughout the process the neck maintains a layered crystalline structure (see Figs. 6 and 4e) except for the rather short structural transformation periods, corresponding to the sharp variations in the force curve, (see segments PQ, RS, TU and VW in Fig. 3b) and the associated features in the calculated potential energy shown in Fig. 3c where the minima correspond to ordered layered structures after the structural rearrangements. We note that beyond the initial formation stage, the number of atoms in the connective neck region remains roughly constant throughout the elongation process.

Further insight into the microscopic mechanism of elongation of the connective neck can be gained via consideration of the variation of the second invariant of the stress deviator, J_2 , which is related to the von Mises shear strain-energy criterion for the onset of plastic yielding [18a,19]. Returning

to the force and potential energy curves shown in Figs. 3b and 3c, we have observed that between each of the elongation events (i.e., layer additions, points marked Q, S, U, W and X) the initial response of the system to the strain induced by the increased separation between the tip-holder and the substrate is mainly elastic (segments OP, QR, ST, UV in Fig. 3b, and correspondingly the variations in Fig. 3c), accompanied by a gradual increase of $\sqrt{J_2}$, and thus the stored strain energy. The onsets of the stages of structural rearrangements are found to be correlated with a critical maximum value of $\sqrt{J_2}$ of about 3 GPa (occurring for states at the end of the intervals marked OP, QR, ST and UV in Fig. 3b) localized in the neck in the region of the ensuing structural transformation. After each of the elongation events the maximum value of $\sqrt{J_2}$ (for the states marked Q, S, U, W and X in Fig. 3b) drops to approximately 2 GPa.

In this context, it is interesting to remark that the value of the normal component of the force per unit area in the narrowest region of the neck remains roughly constant (~ 10 GPa) throughout the elongation process, increasing by about 20% prior to each of the aforementioned structural rearrangements. This value has been estimated both by using the data given in Figs. 3c and the cross sectional areas from atomic configuration plots (such as given in Fig. 6), and via a calculation of the average axial component (zz element) of the atomic stress tensors [51] in the narrow region of the neck. We note that the above observations constitute atomic-scale realizations of basic concepts which underlie macroscopic theories of materials behavior under load [17-19].

A typical distribution of the stress, $\sqrt{J_2}$, prior to a structural transformation is shown in Fig. 7 (shown for the state corresponding to the point marked T in Fig. 3b). As seen, the maximum of $\sqrt{J_2}$ is localized about a narrow region around the periphery in the strained neck. Comparison between the

atomic configuration at this stage (see Fig. 7, or the very similar configuration shown in Fig. 6c) and the configuration after the structural transformation has occurred (see Fig. 6d, corresponding to the point marked U in Fig. 3b) illustrates the elongation of the neck by the addition of a layer and accompanying reduction in areal cross section. We note that as the height of the connective neck increases the magnitude of the variations in the force and potential energy during the elongation stages diminishes. The behavior of the system past the state shown in Fig. 6f (corresponding to the point marked X in the force curve shown in Fig. 3b) is similar to that observed at the final stages of separation after jump-to-contact (Fig. 3b), characterized by strain induced disordering and thinning in a narrow region of the neck near the gold covered bottom of the tip and eventual fracture of the neck (occurring for a tip-to-substrate distance $d_{ts} \approx 18 \text{ \AA}$), resulting in a Ni tip whose bottom is covered by an adherent Au layer.

The theoretically predicted increased hysteresis upon tip-substrate separation following indentation, relative to that found after contact (compare Figs. 3a and 3b), is also observed experimentally, as shown in Fig. 2b. In both theory and experiment the maximum attractive force after indentation is roughly 50% greater than when contact is first made. Note however that the nonmonotonic features found in the simulations (Fig. 3b) are not discernible in the experiment which is apparently not sufficiently sensitive to resolve such individual atomic-scale events when averaged over the entire contact area.

Finally we remark that scanning Auger microscopy (SAM) was used to detect gold transfer onto the nickel tip following indentation. The lack of sensitivity of SAM to concentrations of materials less than 0.1% prohibits us from detecting Au transfer onto the tip for the typical small loads used in the measurements discussed in this paper. However, we did observe the

presence of Au on the Ni tip following the application of a load of ~ 100 mN between a freshly cleaned Ni tip and a Au surface, just moments before placing the tip into the Auger vacuum chamber for analysis.

CONCLUDING REMARKS

The recent emergence and proliferation of proximal probes, in particular tip-based microscopies [33-36], sensitive to nano- and subnano- meter scale structures provides compelling opportunities for studies of these structures which are key to the science base of many venerable technological problems [36]. In addition these probes, coupled with advances in theoretical understanding of the energetics and interaction mechanisms in materials and the development of computer-based materials modeling and simulation techniques, open new avenues for exploration of new scientific concepts and novel materials properties and processes on the subnanometer scale [36,52].

In this paper we have presented results of joint theoretical, molecular dynamics simulations, and experimental, atomic force microscopy, studies of the mechanisms and properties of intermetallic adhesive interactions, contact formation, nanoindentation and mechanical response. Our studies show that contact formation between a hard tip (nickel) approaching a soft metallic substrate (gold) is associated with an atomic-scale instability which leads to a jump-to-contact phenomenon which involves an inelastic response of the atoms in the proximal interfacial region of the gold substrate. Indentation of the surface by advancing the tip beyond the point of contact results in the onset of plastic yielding, adhesion-induced atomic flow and generation of slip in the surface region of the gold substrate. Separating the two materials from contact results in adhesion-induced wetting of the tip by gold atoms, adherence of a gold monolayer to the nickel tip, formation of an atomically thin connective neck and eventual fracture. Furthermore, retracting the tip

from the sample after indentation results in ductile extension of the substrate and formation of a connective crystalline neck which elongates, while reducing in cross-sectional area, via structural transformations involving elastic and yielding stages.

The above microscopic processes are portrayed in the theoretically calculated and experimentally measured force versus distance curves (Figs. 2 and 3), which exhibit pronounced hysteresis upon tip-to-sample approach and subsequent separation. We note however, that due to experimental constraints (such as the need to employ a cantilever of finite flexibility, sample and tip cleanliness, and tip size) certain characteristic features predicted by the simulations (i.e., the nonmonotonic behavior of the force vs. distance relationship during separation after indentation, associated with atomic structural transformations during elongation of the connective neck) could not be resolved in the present measurements.

Our investigations provide the impetus for further combined theoretical and experimental investigations of the microscopic mechanisms of adhesion, contact formation and atomic-scale mechanical response processes in materials, motivating a critical assessment of the range of validity of continuum theories and reformulation of contact mechanics formalisms [10,19,53] to incorporate an atomistic description of the processes of adhesion, deformation, wetting and fracture. In addition, the results presented here are pertinent to the general issue of the consequences of tip-substrate interactions in tip based microscopies (STM and AFM) and for studies of the transition from tunneling to point contact in STM [12,13,54-56]. Finally, our studies suggest a method for preparation of atomic size contacts and atomically thin wires (via the process of contact formation between a metallic tip and a soft metal substrate, followed by gentle separation) which could be used to study quantum conductance in narrow constrictions [57].

Acknowledgement

The authors thank I. Singer, H. Pollock, N. Turner and the STM group (S. Brandow, R. Brizzolara, D. DiLella, K. Lee, and C. Marrian) for their suggestions and helpful discussions. We thank C. L. Cleveland for most valuable assistance with the generation of computer graphics, V. P. Mallette for excellent photography and A. Ralston for meticulous typing. We would like to thank the US DOE, NSF and AFOSR (U.L.) and ONR (R.J.C.) for support of this work. Simulations were performed on the Cray Research, Inc. computers at NMFECC, Livermore, CA through a grant from DOE. This work was done while N.A.B. held a National Research Council-Naval Research Laboratory Research Associateship.

Figures

Fig. 1. (a) Schematic diagram showing the relative positions of the tunneling tip, cantilever tip and sample. The tunneling tip is under feedback control, operating in the constant current mode. The piezos are used to move the tunneling tip and sample. The cantilever for this experiment was made from a piece of Ni wire bend into the shape of a 'L' with a spring constant of 5000 N/m. The short part of the 'L' was chemically etched into a tip with a radius of curvature of approximately 200 nm. (b) Schematic diagram illustrating the force measurement technique.

Fig. 2. Experimentally measured force versus tip-to-sample distance relationship between a Ni tip and Au sample for (a) contact followed by separation and (b) indentation followed by separation. The force curves were obtained using AFM in dry nitrogen.

Fig. 3. Calculated force, F_z , versus tip-to-sample distance, d_{hs} , relationship between a Ni tip and an Au sample for: (a) approach and jump-to-contact followed by separation; (b) approach, jump-to-contact, indentation and subsequent separation. d_{hs} denotes the distance between the rigid tip-holder assembly and the static substrate of the Au surface ($d_{hs} = 0$ at the jump-to-contact point, marked D). The capital letters on the curves denote the actual distances, d_{ts} , between the bottom part of the Ni tip and the Au surface; in (a): A = 5.7 Å, B = 5.2 Å, C = 4.7 Å, D = 3.8 Å, E = 4.4 Å, F = 4.85 Å, G = 5.5 Å, H = 5.9 Å, I = 6.2 Å and J = 7.5 Å; in (b): D = 3.8 Å, L = 2.4 Å, M = 0.8 Å, N = 2.6 Å O = 3.0 Å, P = 3.8 Å, Q = 5.4 Å, R = 6.4 Å, S = 7.0 Å, T = 7.7 Å, U = 9.1 Å, V = 9.6 Å, W = 10.5 Å and X = 12.8 Å. (c) Potential energy of the system for a complete cycle of the tip approach, jump-to-contact, indentation and subsequent separation. Forces in units of nN, energy in eV and distances in Å.

Fig. 4. Atomic configurations generated by the MD simulations. (a) after jump-to-contact (see point D in Fig. 3a). Note bulging of the Au substrate under the Ni tip and partial wetting of the tip edges. (b) Separation after contact (point J in Fig. 3a) illustrating adherence of the top Au layer to the Ni tip and the formation of an atomically thin connective neck. (c) A cut through the system at the point of maximum indentation (M in Fig. 3b), illustrating deformation of the Au substrate and slip along (111) planes of the substrate, (d) separation after indentation (point X in Fig. 3b), illustrating wetting of the Ni tip by Au atoms, faceting of the Ni tip exposing (111) facet planes, incorporation of Ni atoms in substitutional sites, and formation of an extensive connective neck between the tip and the substrate. Note the crystalline character of the neck and the incorporation of atoms from the first, second and third topmost layers of the Au surface as well as several Ni atoms. (e) A cut through the system shown in (d) illustrating the crystalline structure of the neck and the extent of structural deformations of the substrate. In these figures the Ni tip atoms are colored red; atoms of the top layer of the Au surface in yellow, second layer in blue, third layer in green, fourth in yellow, etc.

Fig. 5. Calculated pressure contours and atomic configurations viewed along the [010] direction, in slices through the system. The Ni tip occupies the topmost eight atomic layers. Short-time atomic trajectories appear as dots. Distance along the X and Z directions in units of $X = 1$ and $Z = 1$ corresponding to 61.2 \AA each. Solid contours correspond to tensile stress (i.e., negative pressure) and dotted ones to compressive stress. (a) after jump-to-contact (point D in Fig. 3a, see also Fig. 4a). The maximum magnitude of the tensile (i.e., negative pressure, 10GPa, is at the periphery of the

contact, $(X,Z) = (\pm 0.19, 0.27)$. The contours are spaced with an increment, Δ , of 1 GPa. Thus the contours marked e, f and g correspond to -6, -5 and -4 GPa, respectively. (b) During separation following contact, (point G in Fig. 3a). The maximum tensile pressure (marked a), ~ -9 GPa, is at the periphery of the contact at (X,Z) equal to $(0.1, 0.25)$ and $(-0.04, 0.25)$. $\Delta = 0.9$ GPa. The marked contours h, i, j and k correspond to -2.5, -1.6, -0.66 and 0.27 GPa, respectively. (c) Short-time particle trajectories at the final stage of relaxation of the system, corresponding to point M in Fig. 3b, (i.e., $F_z = 0$). Note slip along the $[111]$ planes in the substrate. (d) Pressure contours corresponding to the final configuration shown in (c). Note the development of compressive pressure in the substrate which maximizes in the region of the contour marked l (8.2 GPa). The increment between contours $\Delta = 1.4$ GPa. The contours marked a and e correspond to -6.4 GPa and -1.1 GPa, respectively, and those marked f and g to 0.2 and 1.6 GPa.

Fig. 6. Atomic configurations in slices through the system illustrating the formation of a connective neck between the Ni tip and the Au substrate during separation following indentation. The Ni tip occupies the topmost eight layers. The configurations (a-f) correspond to the stages marked O, Q, S, U, W, and X in Fig. 3b. Note the crystalline structure of the neck. Successive elongations of the neck, upon increased separation between the tip-holder assembly and the substrate, occur via structural transformation resulting in successive addition of layers in the neck accompanied by narrowing (i.e., reduction in cross-sectional area of the neck). Distance in units of X and Z , with $X = 1$ and $Z = 1$ corresponding to 61.2 Å.

Fig. 7. von Mises' shear stress ($\sqrt{J_2}$) corresponding to the configuration marked T in Fig. 3b (i.e., just before the structural transformation resulting in the configuration (d) in Fig. 6). The proximal interfacial layers of Ni and Au are marked by arrows. The maximum contours (2.9GPa, marked a) occur on the periphery of the neck (X, Z) = ($\pm 0.1, 0.3$). The increment between contours is 0.2GPa. The contours marked h, i, j and k correspond to 1.1, 0.9, 0.7 and 0.5GPa, respectively. Distance along X and Z in units of $X = 1$ and $Z = 1$ corresponding to 61.2 Å.

References

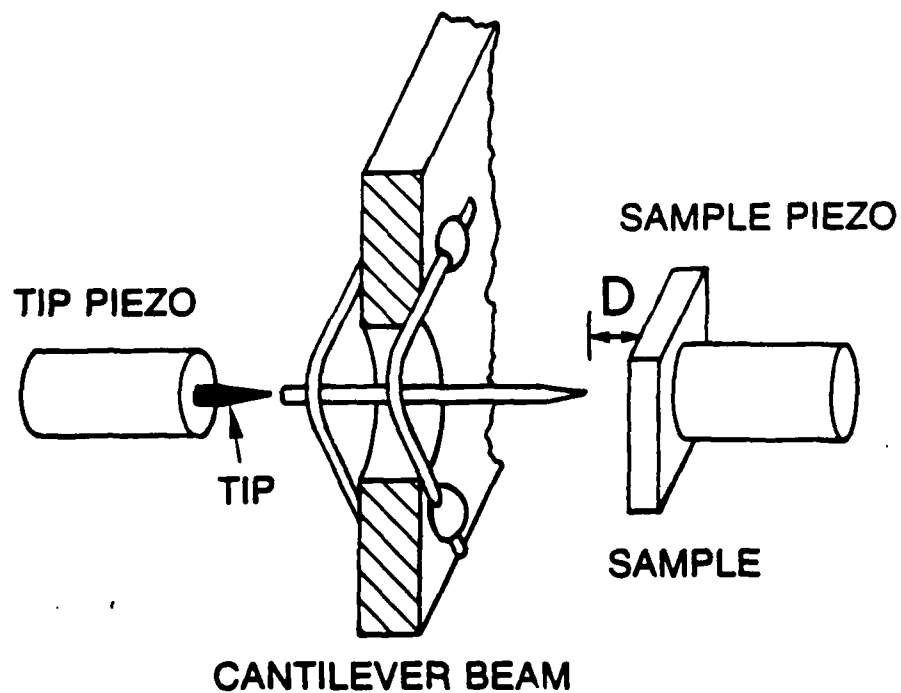
1. (a) D. Tabor, J. Coll. Interface Sci. 58, 2 (1977); (b) M. D. Pashley and D. Tabor, Vacuum 31, 619 (1981).
2. N. Gane, P. F. Pfaelzer and D. Tabor, Proc. Roy. Soc. London A 340, 395 (1974).
3. H. M. Pollock, Vacuum 31, 609 (1981).
4. D. Maugis, Le Vide 186, 1 (1977).
5. R. G. Horn, J. N. Israelachvili and F. Pribac, J. Coll. Interface Sci. 115, 480 (1987) and references therein.
6. N. A. Burnham and R. J. Colton, J. Vac. Sci. Technol. A7, 2906 (1989).
7. U. Landman, W. D. Luedtke and R. N. Barnett in Many-Atom Interactions in Solids, edited by R. M. Nieminen (Plenum, N. Y., 1989), where a preliminary report of the theoretical studies can be found.
8. D. Tabor and R. H. S. Winterton, Proc. Roy. Soc. London A312, 435 (1969).
9. H. M. Pollock, P. Shufflebottom and J. Skinner, J. Phys. D 10, 127 (1977); H. M. Pollock, *ibid.* 11, 39 (1978).
10. N. Gane and F. P. Bowden, J. Appl. Phys. 39, 1432 (1968).
11. D. Maugis and H. M. Pollock, Acta Metall. 32, 1323 (1984), and references therein.
12. U. Durig, J. K. Gimzewski and D. W. Pohl, Phys. Rev. Lett. 57, 2403 (1986); U. Durig, O. Zuger and D. W. Pohl, J. Microsc. 152, 259 (1988).
13. J. M. Gimzewski and R. Moller, Phys. Rev. B36, 1284 (1987).
14. J. B. Pethica and A. P. Sutton, J. Vac. Sci. Technol. A6, 2494 (1988).
15. J. R. Smith, G. Bozzolo, A. Banerjea and J. Ferrante, Phys. Rev. Lett. 63, 1269 (1989).
16. U. Landman, W. D. Luedtke and M. W. Ribarsky, J. Vac. Sci. Technol. A7, 2829 (1989); Mat. Res. Soc. Symp. Proc. 140, 101 (1989); see also M. W. Ribarsky and U. Landman, Phys. Rev. B38, 9522 (1988).

17. (a) H. Hertz, J. Reine Angew. Math. 92, 156 (1882); also in Miscellaneous Papers (MacMillan, London, 1896), p. 146; (b) See review by K. L. Johnson, Proc. Instn. Mech. Engrs. 196, 363 (1982).
18. (a) G. Dieter, Mechanical Metallurgy, (McGraw-Hill, New York, 1967); (b) E. Rabinowicz, Friction and Wear of Materials, (Wiley, New York, 1965); (c) S. P. Timoshenko and J. N. Goodier, Theory of Elasticity, (McGraw-Hill, New York, 1970), 3rd Edition.
19. K. L. Johnson, Contact Mechanics (Cambridge Univ. Press, Cambridge, 1985).
20. K. L. Johnson, K. Kendall and A. D. Roberts, Proc. Roy. Soc. A324, 301 (1971).
21. B. V. Derjaguin, V. M. Muller and Yu. P. Toporov, J. Coll. Interface Sci. 53, 314 (1975); V. M. Muller, B. V. Derjaguin and Yu. P. Toporov, Colloids Surfaces 7, 251 (1983).
22. P. A. Pashley, Colloids Surfaces 12, 69 (1984).
23. D. Tabor, The Hardness of Metals (Clarendon Press, Oxford, 1951).
24. J. B. Pettica, R. Hutchings and W. C. Oliver, Phil. Mag. A48, 593 (1983).
25. N. Gane, Proc. Roy. Soc. London A317, 367 (1970), and references therein.
26. Microindentation Techniques in Materials Science and Engineering, edited by P. J. Blau and B. R. Lawn (American Society for Testing and Materials, Philadelphia, 1985).
27. M. F. Doerner and W. D. Nix, J. Mater. Res. 1, 601 (1988).
28. (a) See articles in Mat. Res. Soc. Symp. Proc. 140, 101 (1989), edited by L. E. Pope, L. L. Fehrenbacher and W. O. Winer, (Mat. Res. Soc., Pittsburgh, 1989); (b) F. P. Bowden and D. Tabor, Friction and Lubrication Solids (Clarendon Press, Oxford, 1950).
29. C. W. Mate, G. M. McClelland, R. Erlandsson and S. Chiang. Phys. Rev. Lett. 59, 1942 (1987).

30. U. Landman, W. D. Luedtke and A. Nitzan, Surf. Sci. 210, L177 (1989).
31. R. Thomson, Solid State Physics 9, 1 (1986).
32. B. R. Lawn, Appl. Phys. Lett. 47, 809 (1985).
33. G. Binning, C. F. Quate and Ch. Gerber, Phys. Rev. Lett. 56, 930 (1986).
34. J. N. Israelachvili, Acc. Chem. Res. 20, 415 (1987); Proc. Nat. Acad. Sci. USA 84, 4722 (1987); J. N. Israelachvili, P. M. McGuiggan and A. M. Homola, Science 240, 189 (1988).
35. G. Binning, H. Rohrer, Ch. Gerber and E. Weibel, Phys. Rev. Lett. 50, 120 (1983).
36. See reviews by: P. K. Hansma and J. Tersoff, J. Appl. Phys. 61, R1 (1986); R. J. Colton and J. S. Murday, Naval Res. Rev., Vol. XL, 2 (1988); J. S. Murday and R. J. Colton, J. Mater. Sci. and Engr. B (to be published); J. S. Murday and R. J. Colton in Chemistry and Physics of Solid Surfaces. VIII, edited by R. Vanselow and R. Howe, Springer Ser. Surf. Sci. (Springer, Berlin, 1990).
37. See articles in Atomistic Simulation of Materials: Beyond Pair Potentials, edited by V. Vitek and D. J. Srolovitz (Plenum, NY, 1989).
38. See reviews by: F. F. Abraham, Adv. Phys. 35, 1 (1986); J. Vac. Sci. Technol. B2, 534 (1984); U. Landman in Computer Simulation Studies in Condensed Matter Physics: Recent Developments, edited by D. P. Landau, K. K. Mon and H.-B. Schuttler (Springer, Berlin, 1988), p. 108.
39. M. D. Pashley, J. B. Pethica and D. Tabor, Wear 100, 7 (1984).
40. F. F. Abraham, I. P. Batra, and S. Ciraci, Phys. Rev. Lett. 60, 1314 (1988).
41. R. J. Colton, S. M. Baker, R. J. Driscoll, M. G. Youngquist, J. D. Baldeschwieler, and W. J. Kaiser, J. Vac. Sci. Technol. A6, 349 (1988).
42. D. Tomanek, C. Overney, H. Miyazaki, S. D. Mahanti and H. J. Guntherodt, Phys. Rev. Lett. 63, 876 (1989).

43. J. M. Soler, A. M. Baro, N. Garcia and H. Rohrer, Phys. Rev. Lett. 57, 444 (1986); see comment by J. B. Pethica, ibid 57, 3235 (1986).
44. J. B. Pethica and W. C. Oliver, Phys. Scripta T19, 61 (1987).
45. N. A. Burnham, D. D. Dominguez, R. L. Mowery, and R. J. Colton, submitted for publication.
46. Mater. Eng. 90 (6), C120 (1979).
47. (a) S. M. Foiles, M. I. Baskes and M. S. Daw, Phys. Rev. B33, 7983 (1986); (b) The parameterization used in our calculations is due to J. B. Adams, S. M. Foiles, and W. G. Wolfer, J. Mater. Res. Soc. 4, 102 (1989).
48. See review by M. Baskas, M. Daw, B. Dodson, and S. Foiles, Mater. Res. Soc. Bull. XIII, 28 (1988).
49. E. T. Chen, R. N. Barnett and U. Landman, Phys. Rev. B40, 924 (1989); ibid. 41 (1), (1990).
50. R. N. Barnett, U. Landman and C. L. Cleveland, Phys. Rev. B28, 1685 (1983).
51. T. Egami and D. Srolovitz, J. Phys. F: Met. Phys. 12, 2141 (1982).
52. R. P. Feynman, in Miniaturization, edited by H. D. Gilbert (Reinhold, NY, 1961), p. 282.
53. Q. Guo, J. D. J. Ross and H. M. Pollock, in ref. 28a, p. 51.
54. N. D. Lang, Phys. Rev. B 36, 8173 (1987); Comments Condens. Matter Phys. 14, 253 (1989).
55. B. J. van Wees, H. van Houten, C. W. J. Beenakker, J. G. Williamson, L. P. Kouwenhoven, D. van der Marel and C. T. Foxon, Phys. Rev. Lett. 60, 848 (1988); D. A. Wharam et al., J. Phys. C 21, L209 (1988).
56. J. K. Gimzewski, R. Moller, D. W. Pohl and R. R. Schlittler, Surf. Sci. 189/190, 15 (1987).
57. N. D. Lang, A. Yacoby and Y. Imry, Phys. Rev. Lett. 63, 1499 (1989), and references therein.

a)



b)

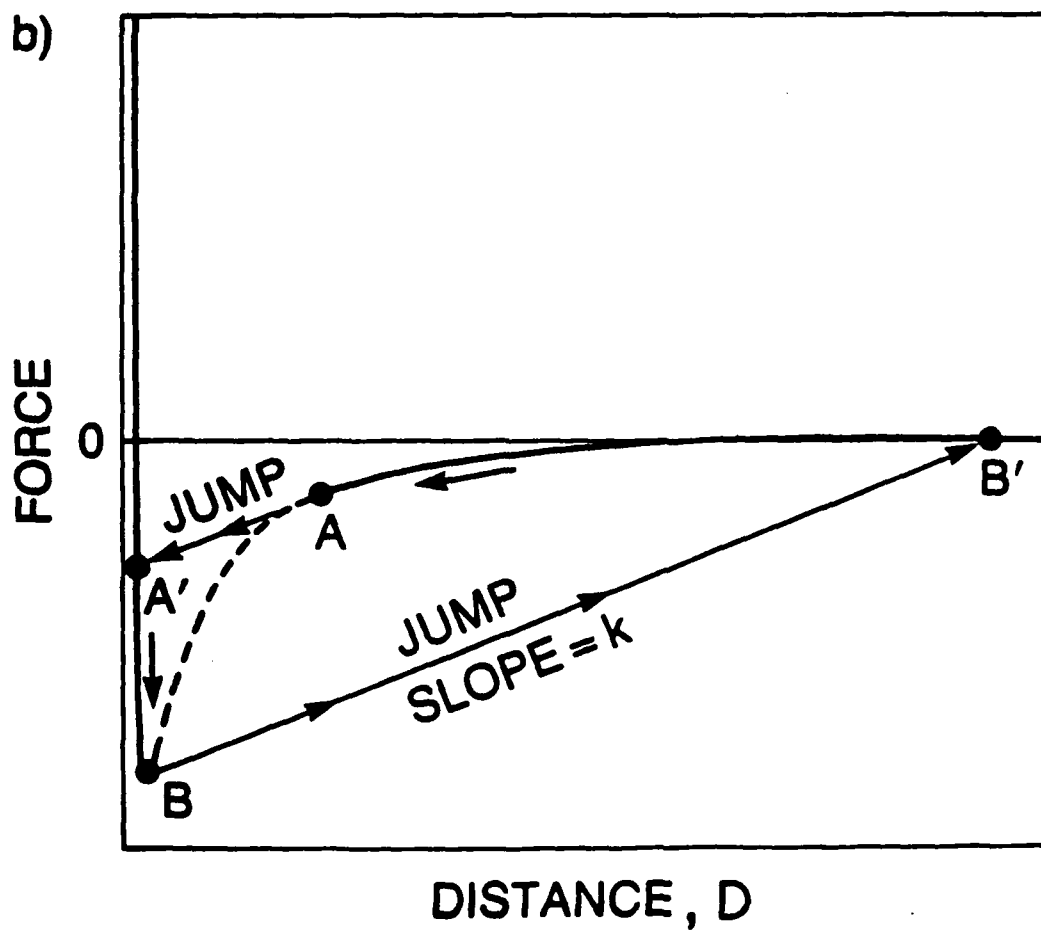


Figure 1

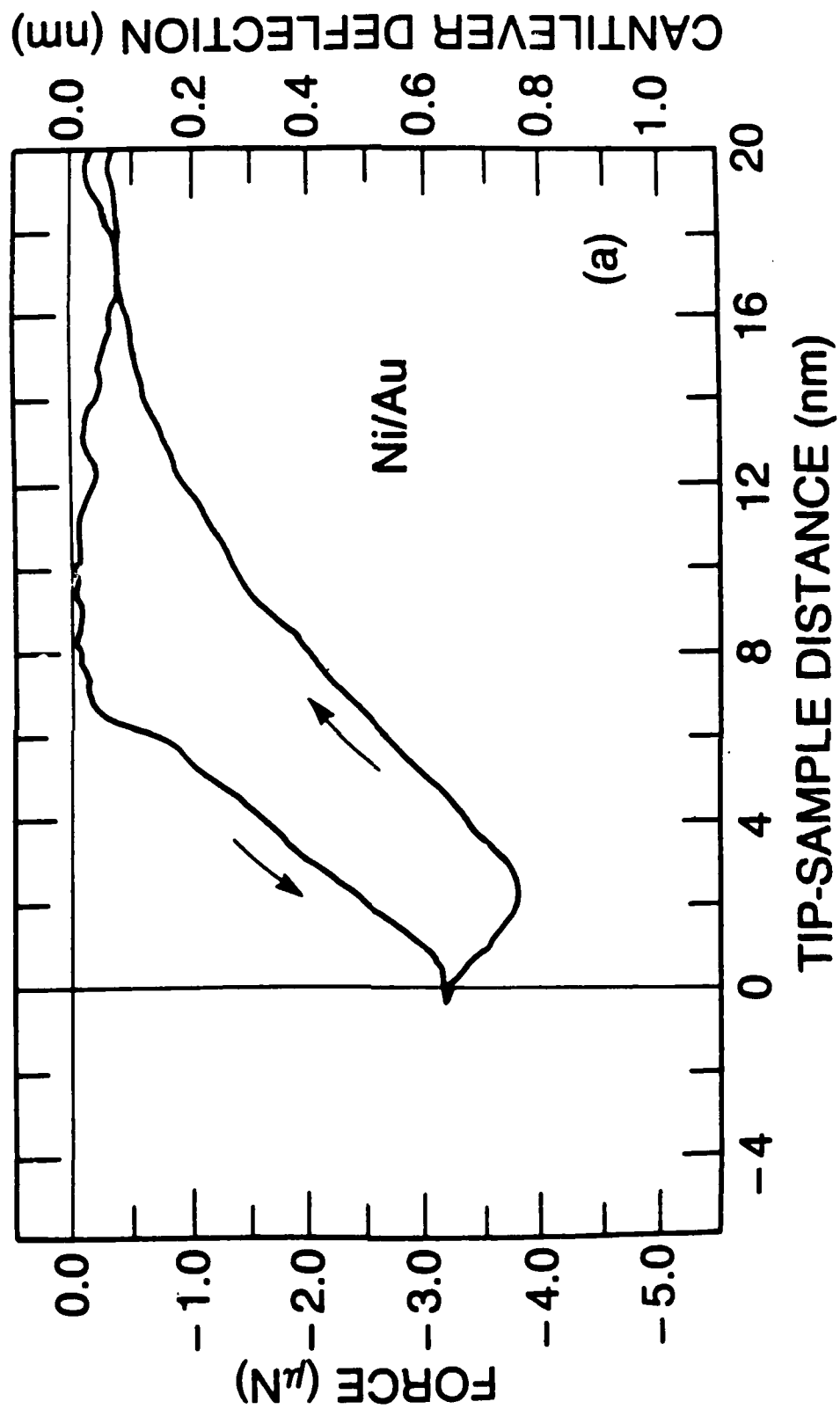


Figure 2a

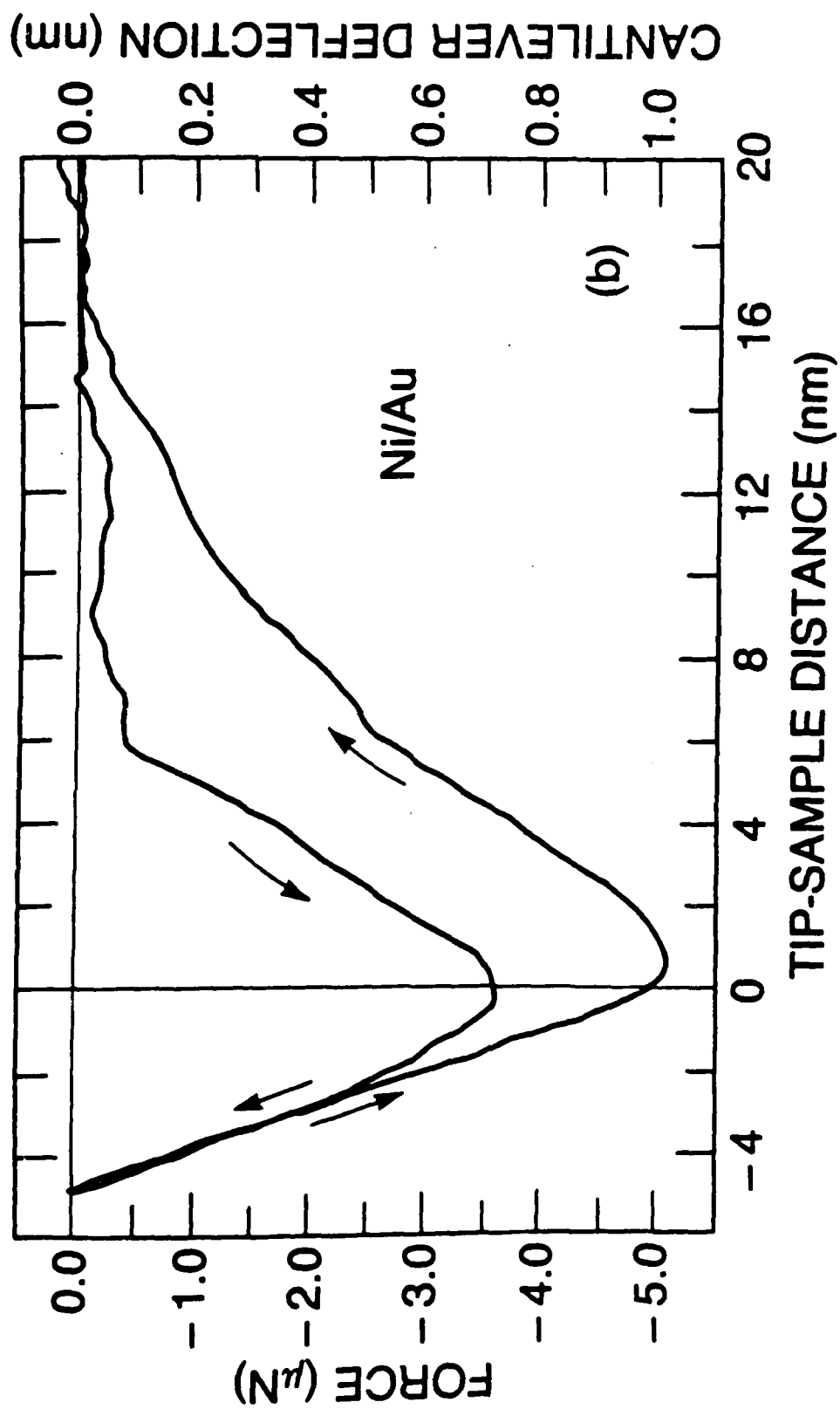


Figure 2b

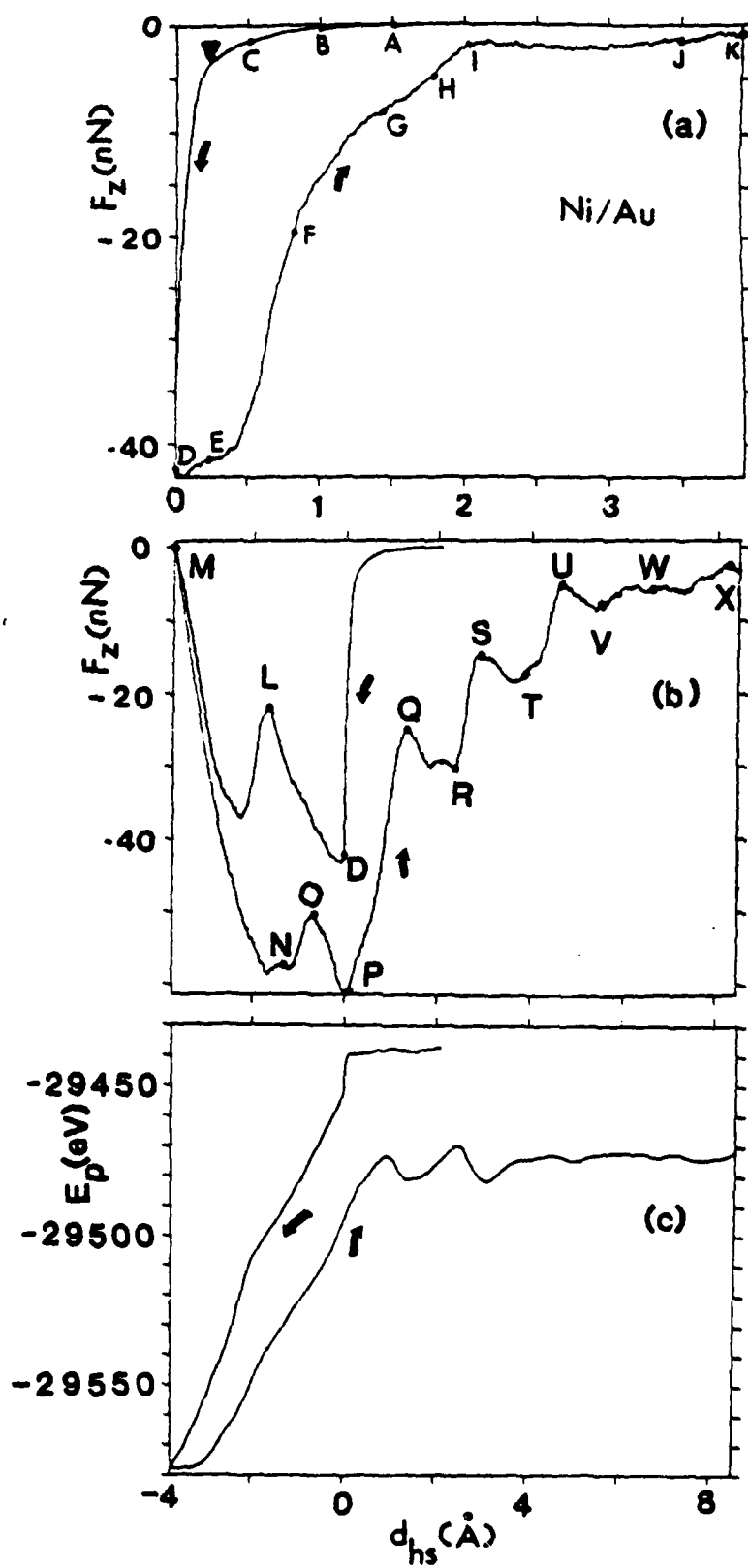
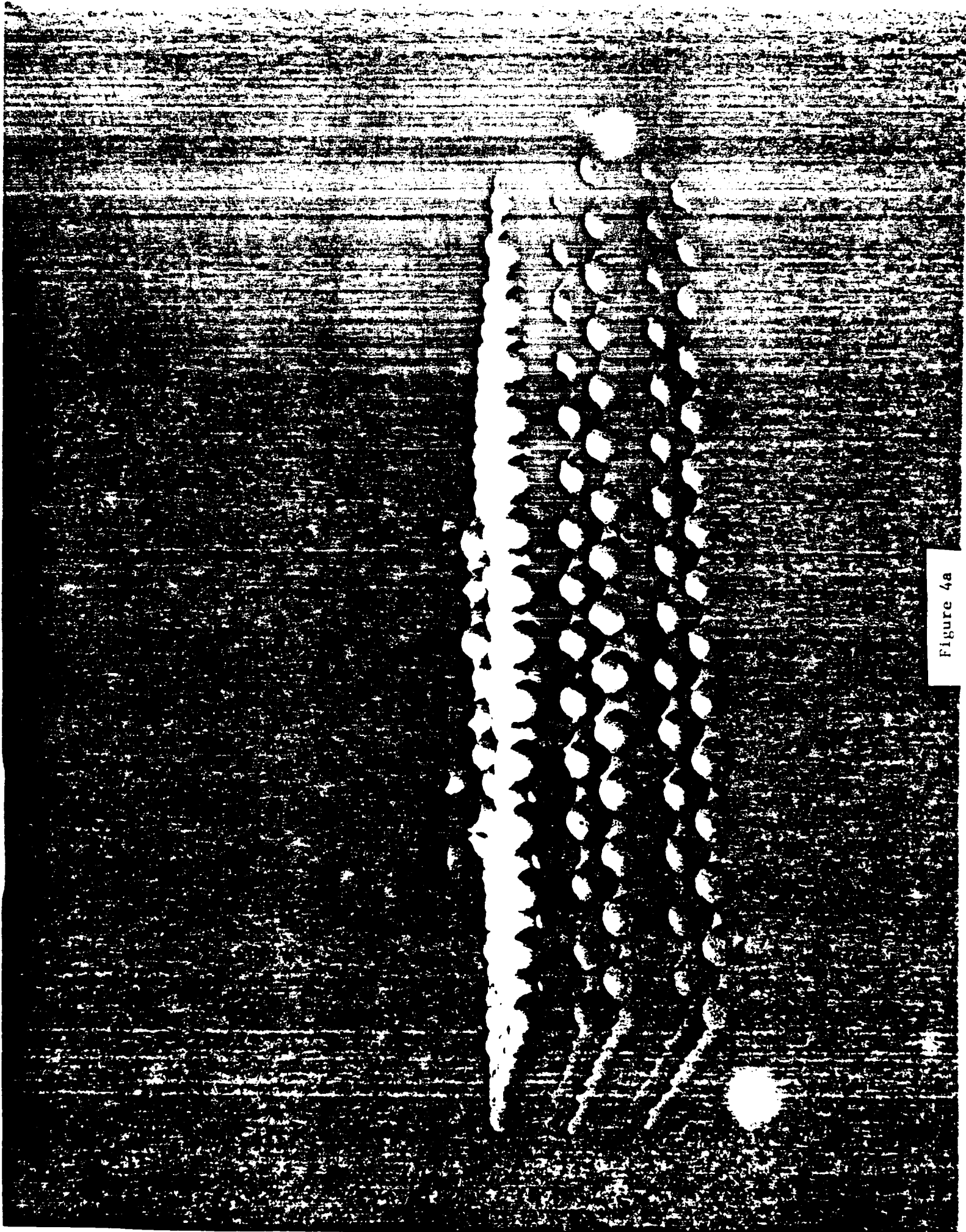


Figure 3

Figure 4a



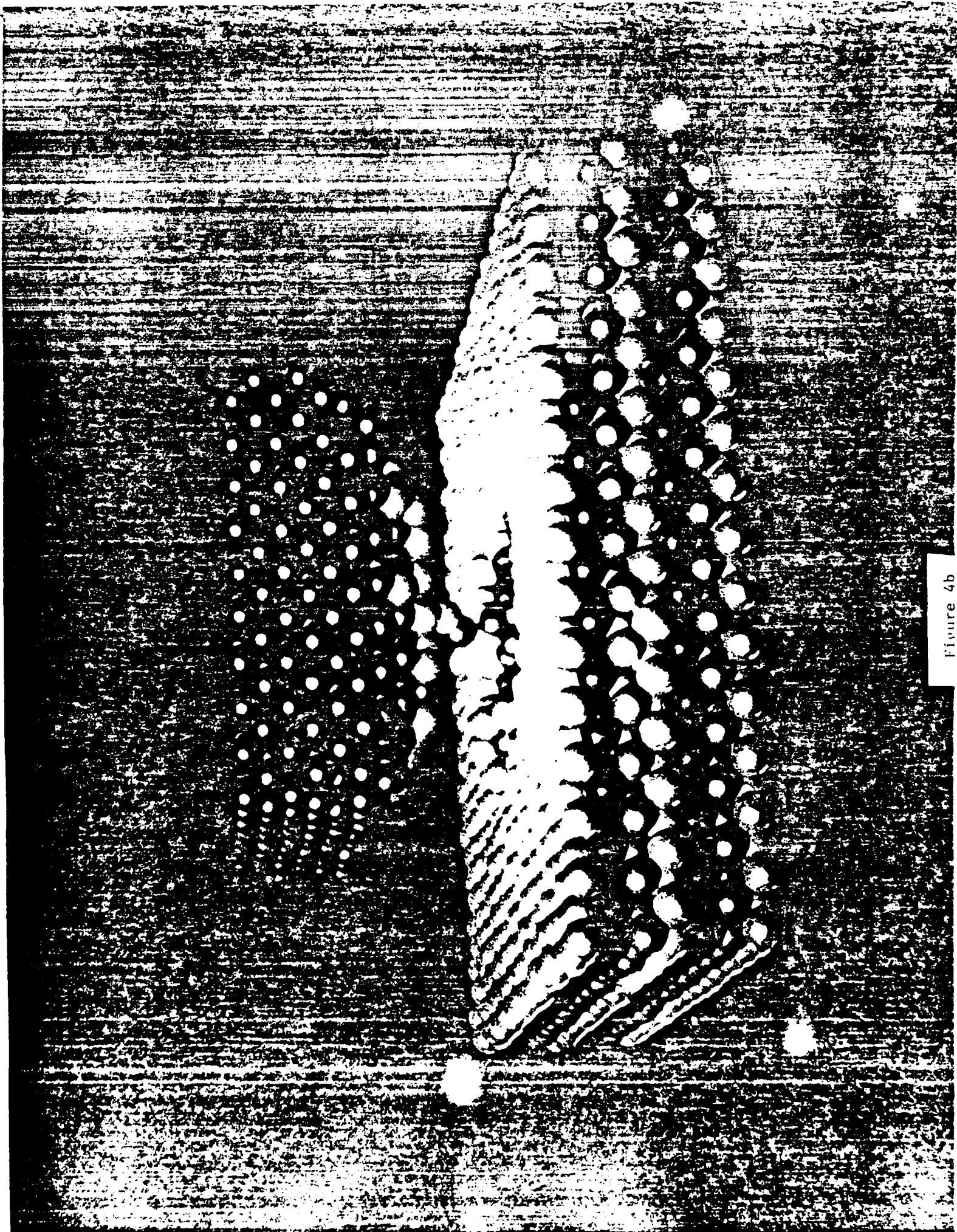


Figure 4b



Figure 4c

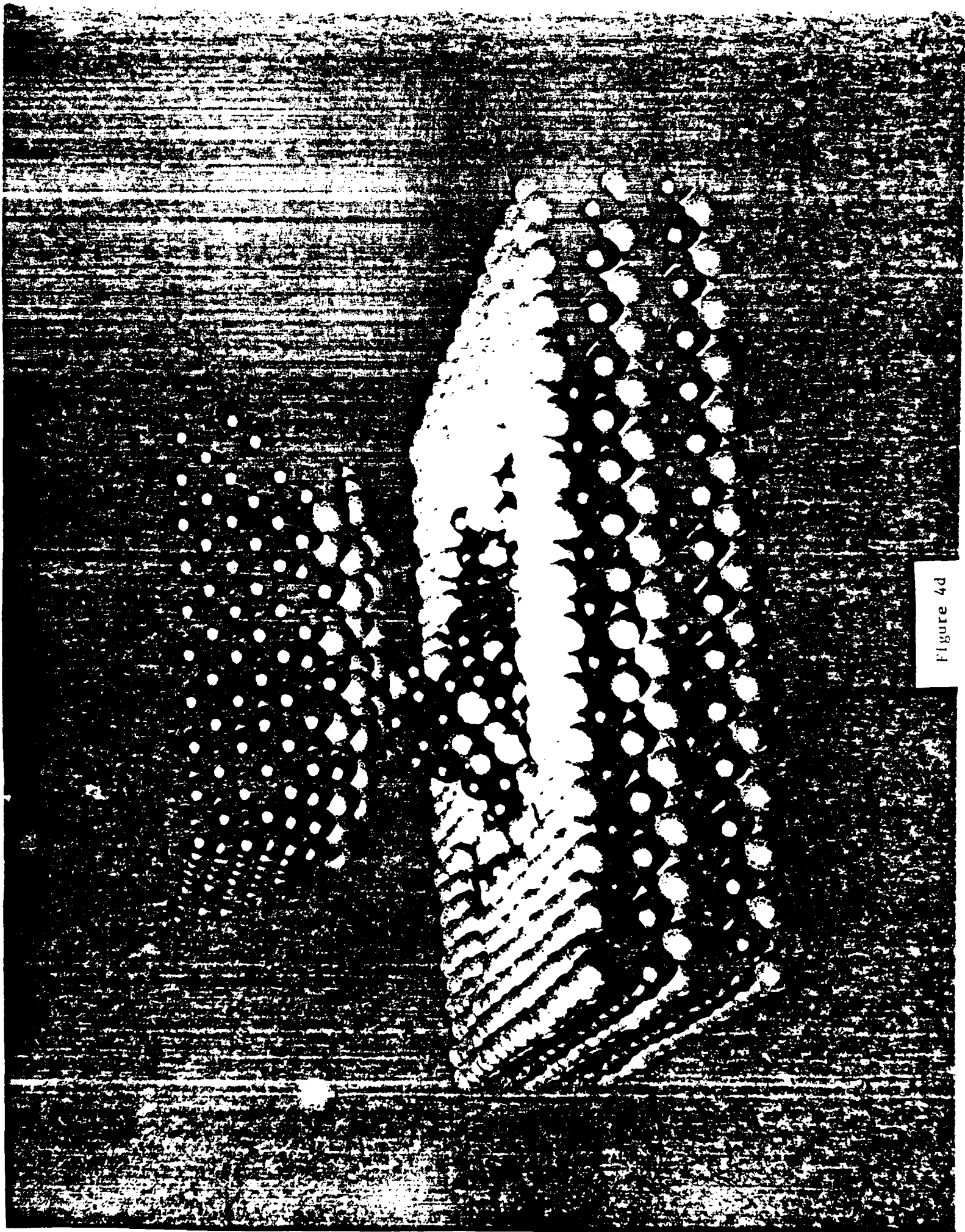


Figure 4d

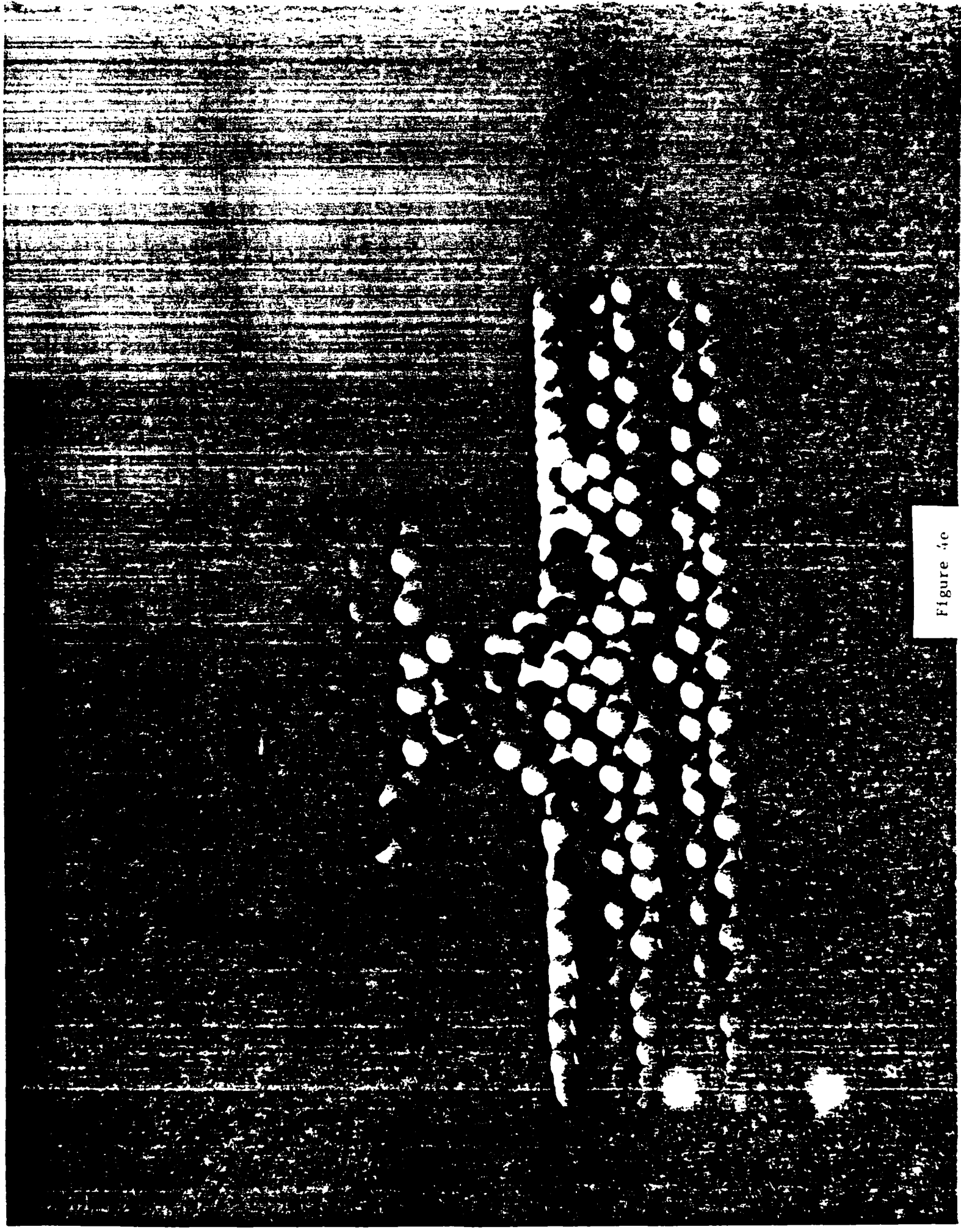


Figure 4c

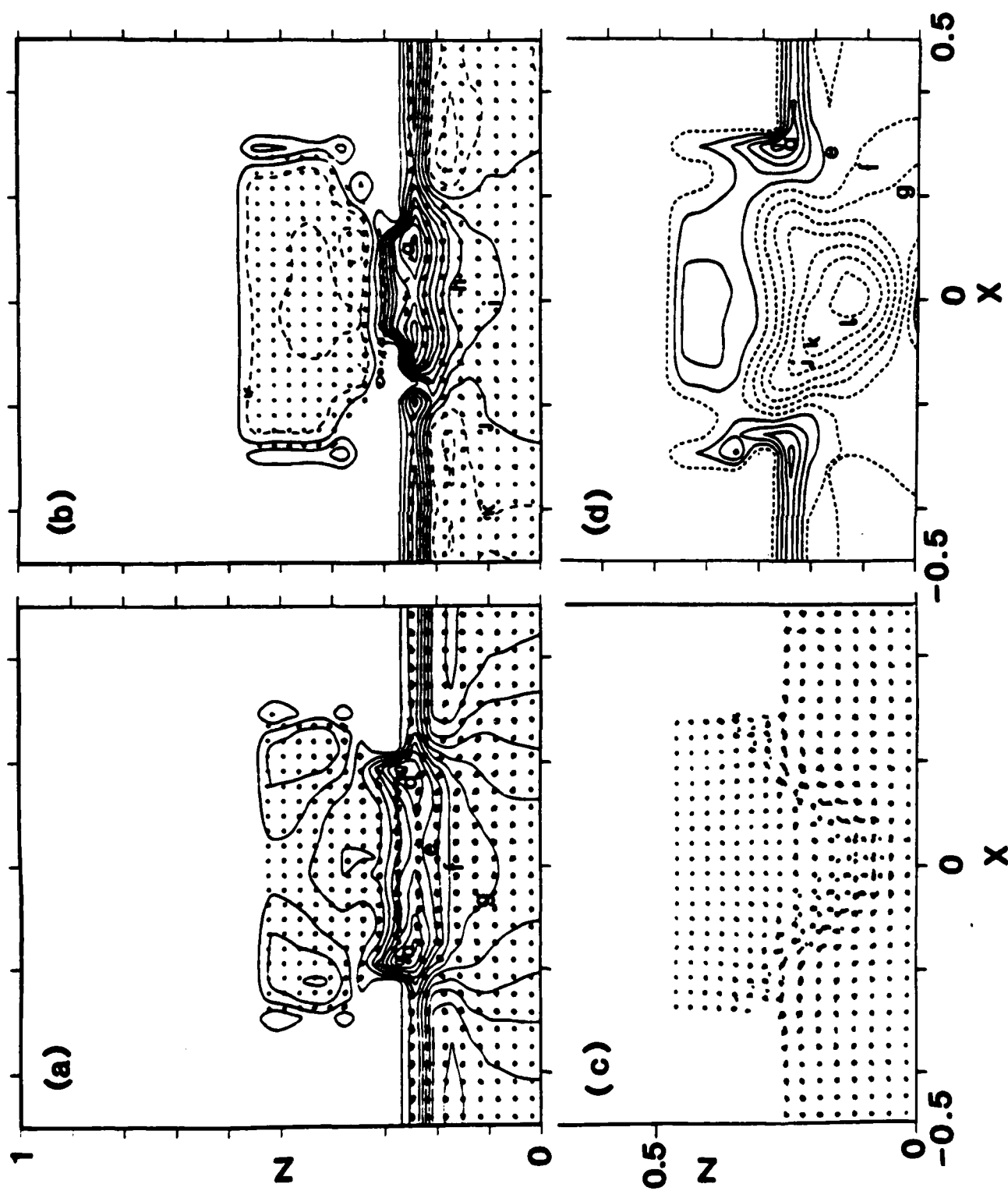


Figure 5

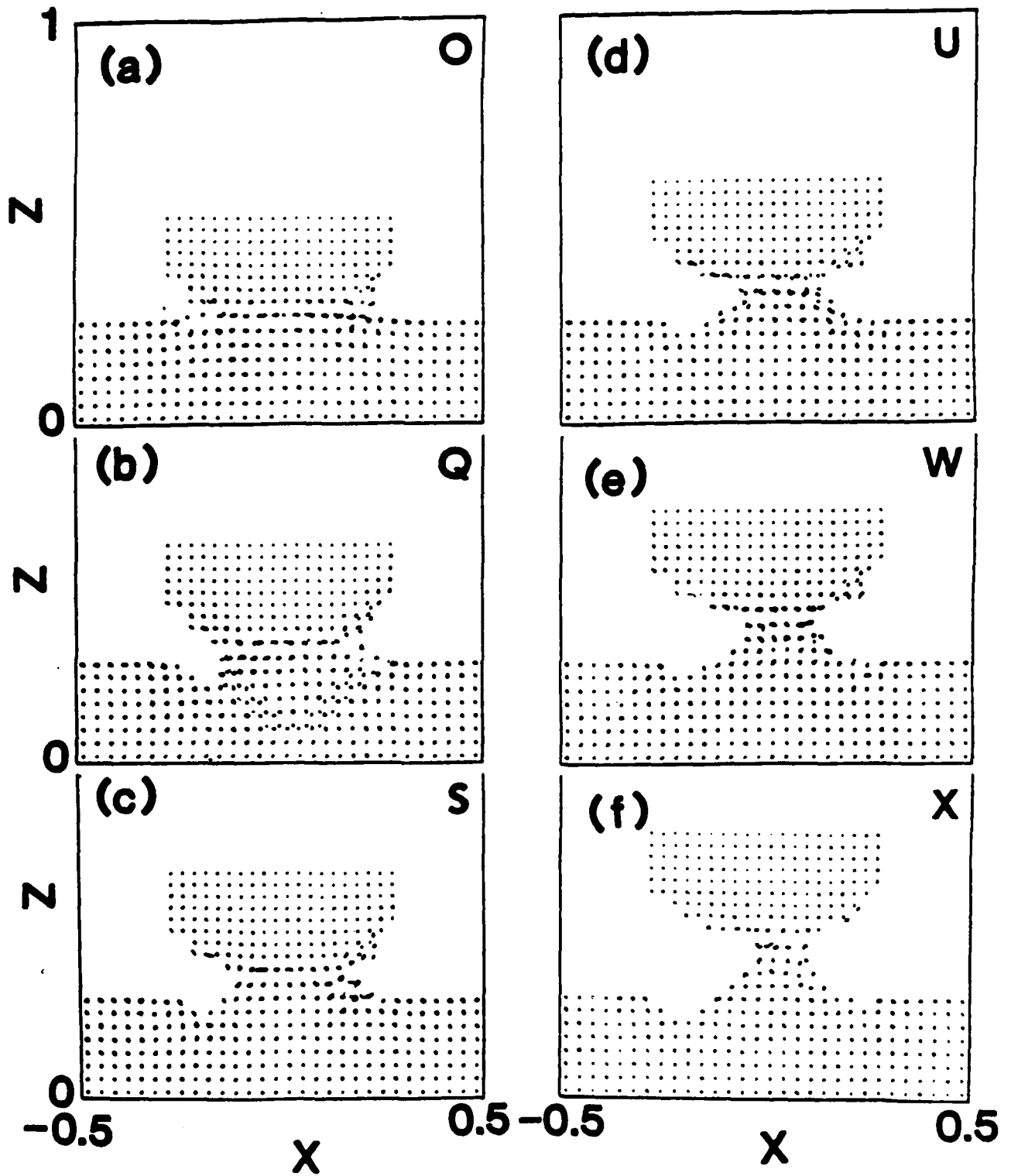


Figure 6

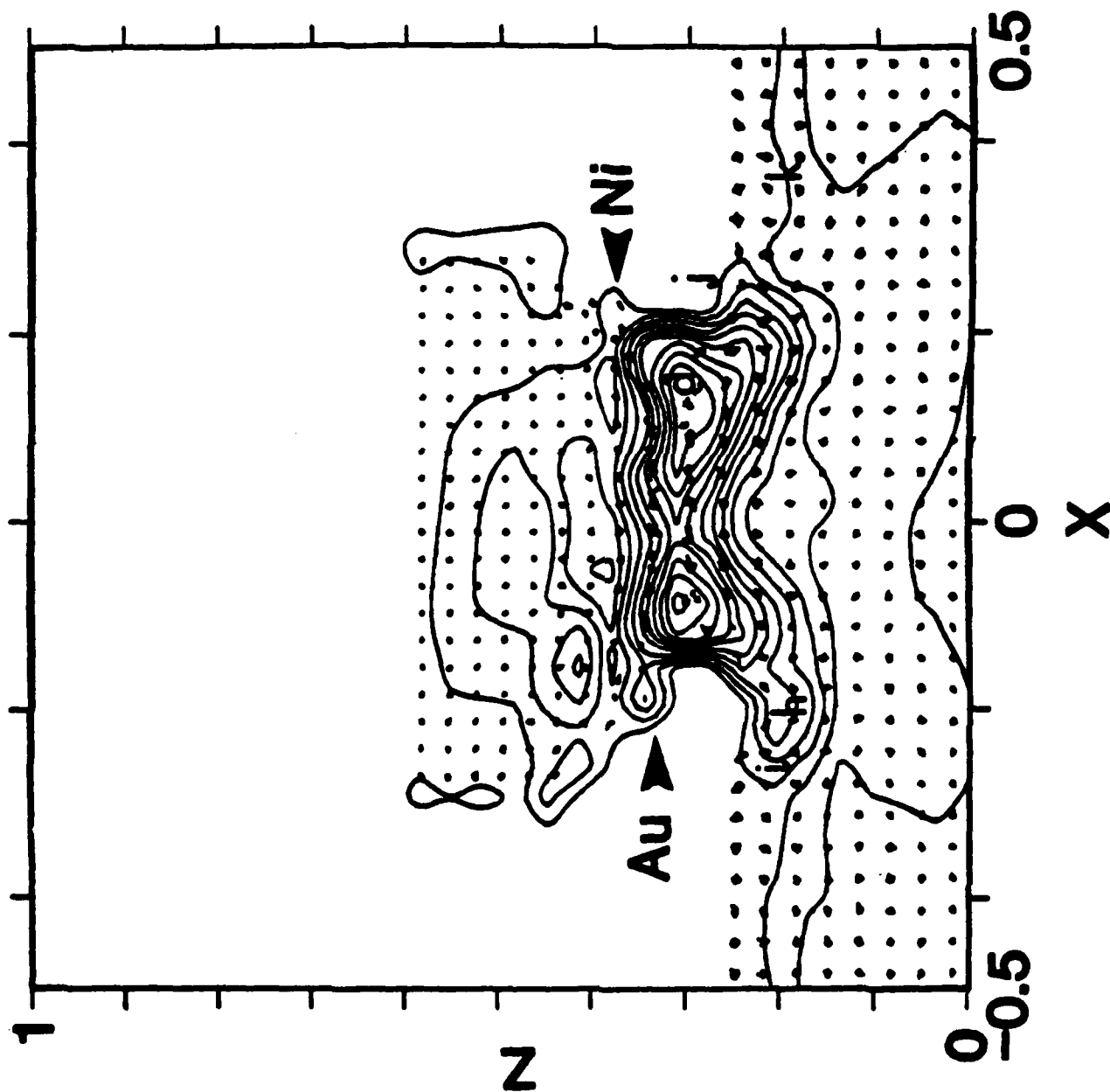


Figure 7